NORTHERN ILLINOIS UNIVERSITY

POINTING MUON TRACKS BACK TO CYGNUS X-3
USING THE D0 MUON COSMIC RAY TELESCOPE

A THESIS SUBMITTED TO THE GRADUATE SCHOOL
IN PARTIAL FULFILLMENT OF THE REQUIREMENTS
FOR THE DEGREE
MASTER OF SCIENCE

DEPARTMENT OF PHYSICS

BY

BRIAN E. DRENDEL

DEKALB, ILLINOIS
AUGUST 1992

Certification: In accordance with departmental and Graduate

School policies, this thesis is accepted in

partial fulfillment of degree requirements.

NORTHERN ILLINOIS UNIVERSITY
DeKalb, Illinois

CERTIFICATE OF COMPLETION

This is to certify that

Name:
Degree:
Major:
Degree Date:

BRIAN ERIC DRENDEL
M. S.
PHYSICS — APPLIED PHYSICS
AUGUST 8, 1992

All requirements for this degree have been satisfied.

Jerrold H. Zar

Dean of the Graduate School

Abstract

An attempt to point muon tracks back to Cygnus X-3 was made using the D0muon Cosmic Ray Telescope. A data set of 11.3 million muon events was examined, representing $\approx$ 313.5 hours of live time from September 13 - December 13, 1989. The data was filtered, which left $3,478,283$ events, with $8,226$ events in a $10° \times 1°$ elliptical window centered on Cygnus X-3. There were also $4,289$, $1,717$, and 452 events in similar windows with momentum cuts of 10 GeV/c, 25 GeV/c, and 100 GeV/c respectively. For each of the windows centered on Cygnus X-3, there were 35 equivalent background windows at the same declination as Cygnus X-3 spaced every $10°$ right ascension. An attempt to look for a DC excess of events from Cygnus X-3 was unsuccessful due to a severe time bias in the data. Phase histograms were used on the windows to look for a source periodicity. Both a cubic and parabolic fit equations were used from the van der Kliss and Bonnet-Bidaud ephemeris to calculate phase. A second time bias was found in the phase histograms, and was eliminated by subtracting an estimated background for each phase bin from each phase bin in the source window. A broad inconsistent peak of only marginal significance in these phase histograms was seen from $0.85 - 0.15$ in phase for the cubic fit, and from $0.00 - 0.25$ in phase in the parabolic fit. This peak could correspond to a peak in the phase histogram seen by Soudan-1 in 1983.

Acknowledgements

I would first like to thank my advisor, Dr. Suzanne Willis, for her guidance, patience, and suggestions as this project unfolded. She was very helpful whenever I had questions, and I am very happy that she suggested and then let me pursue this topic.

Next, I would like to thank Dr. Dave Hedin for being on my advisory board, offering very helpful suggestions, and initially getting me involved at Fermilab as an undergraduate.

I would also like to thank Dr. Mazhar Hasan for being on my advisory board, and teaching Astrophysics classes that were very helpful to this project.

I would like to express my appreciation to Dr. Ken Johns, who provided the astrophysics program that I modified to analyze my data, and helped me understand the data analysis process for looking for a signal coming from a source like Cygnus X-3.

I would also like to thank Dr. Mike Fortner for helping me understand how the cosmic ray telescope electronics function. His help with upgrading the electronics and getting the detector to function was invaluable.

Lastly, I would like to express appreciation to Rod Korte and Dan Russell for the many hours of work that they put in to setting up things for TeX, which I used to typeset this thesis, and for the many problems with TeX that they helped me resolve.

Table of Contents

List of Tables

List of Figures

Chapter 1
Introduction

Cygnus X-3 is an X-ray binary system with an orbital period of only 4.79 hours. Models of the Cygnus X-3 system have been constructed to explain the system's production of X-rays and high energy γ-rays with variable fluxes corresponding to its 4.79 hour orbital period. The time modulated high-energy particles produced by the Cygnus X-3 system, called the parent particles, must travel about 10 kiloparsecs through space until they strike the Earth's atmosphere along with an omnidirectional shower of background cosmic rays. The parent particles that strike the atmosphere can produce a whole cascade of various particles. One of the byproducts of these cascades is positively and negatively charged muons, which can penetrate large amounts of atmosphere and Earth to reach detectors both at sea level and underground. From the angle of the incoming muon track and the time the track passes through a detector, the right ascension and declination of the track can be reconstructed. At this point an attempt to point muon tracks back to Cygnus X-3 or some other source could be made by first looking for a DC excess of events coming from the direction of Cygnus X-3, and secondly by correlating the signal coming from Cygnus X-3 with its 4.79 hour orbital period. Most experiments that looked for a signal from Cyngus X-3 saw no signal or only a marginal signal; however, the Soudan-1 and NUSEX experiments saw a very significant muon signal coming from Cygnus X-3. The inconsistency of the reported results has made this topic

very controversial over the last few years, and more data needs to be collected in order to determine if there actually is a muon signal. In this experiment, I will try to point muon tracks back to Cygnus X-3 with the D0muon cosmic ray telescope, which consists of four muon chambers for reconstructing the tracks, two layers of scintillator and a complex system of electronics for triggering, and a 100-ton magnet for momentum measurements. A large collection of data taken from this detector was examined. After a long filtering and calibration process, I used a program called Dst_kj.for to both look for a DC excess of events coming from Cygnus X-3 and to try to correlate the signal coming from the direction of Cygnus X-3 with its 4.79 hour orbital period.

Chapter 2
Cygnus X-3

2.1. Introduction to Cygnus X-3

Cygnus X-3 was first discovered as an X-ray source in a 1966 rocket flight. It began to draw greater attention on September 2, 1972 when it was discovered to be the source of a very large radio outburst. In fact, Cygnus X-3 was the brightest radio source in the sky for several days.[1] It is not detectable in the optical range due to interstellar matter obscuring the view; however, it has an observed radio, infrared, X-ray, and γ-ray flux. All of these except the radio flux display a steady 4.8 hour periodicity,[2] where the infrared flux varies smoothly by about 15%, while the X-ray intensity varies by a factor of 3.[5] X-ray energies $\geq 1\mathrm{KeV}$ with a luminosity of $\approx 3 \times 10^{38}$ erg/s have been observed from the direction of Cygnus X-3. Ultra-high energy gamma rays have also been detected with energies up to $2 \times 10^{16}\mathrm{eV}$,[4] and have two sharp maxima in the 4.8 hour period.[3] The total output of Cygnus X-3 is believed to reach $\approx 10^5$ that of the sun.[1]

The periodicity dispayed by Cygnus X-3 has been very stable over the range of years, so Cygnus X-3 is believed to be an X-ray binary system, and the 4.8 hour period is believed to be the orbital period of the system. Cygnus X-3 is located in the galactic plane at a distance of 10 to 12 kpc from the sun, and

is located at the equatorial coordinates $\delta = 40.8°$ and $\alpha = 307.6°$ as shown in Figure 2.1.1 and defined in Section **3.1.2**.[3] The binary system is composed of a very dense degenerate neutron star pulsar, and a main sequence companion star that is similar to, but probably less massive than, the sun. The masses of the companion star and the pulsar are not known precisely, but given an estimate of their masses, and using Kepler's third law, we can calculate the distance between the two stars. Kepler's Third Law states that

$$R^3 = \frac{G \left(M_{Neutron\ star} + M_{Companion\ star}\right)}{4\pi^2} T^2 \qquad (2.1.1)$$

We know that the orbital period $T = 4.8\ hours$, and following the example given in Thomson, we can take $M_{Neutron\ star} = 1.5 M_\odot$, and $M_{Companion\ star} = 1.0 M_\odot$,[3] where $M_\odot$ is the mass of the sun. Substituting these values into Eq. (2.1.1), we get

$$R \approx 2 R_\odot \qquad (2.1.2)$$

where $R_\odot$ is the radius of the sun. This is very small on stellar scales, and complicates the theoretical models proposed for the Cygnus X-3 system. In fact, at this small a radius, the neutron star could actually be embedded in the companion star's atmosphere, depending on the radius of the companion star. Eq. (2.1.1) can be rearranged so that so that the distance between the two stars becomes

$$R \approx 10^{11} \left(\frac{M}{M_\odot}\right)^{\frac{1}{3}} cm \qquad (2.1.3)$$
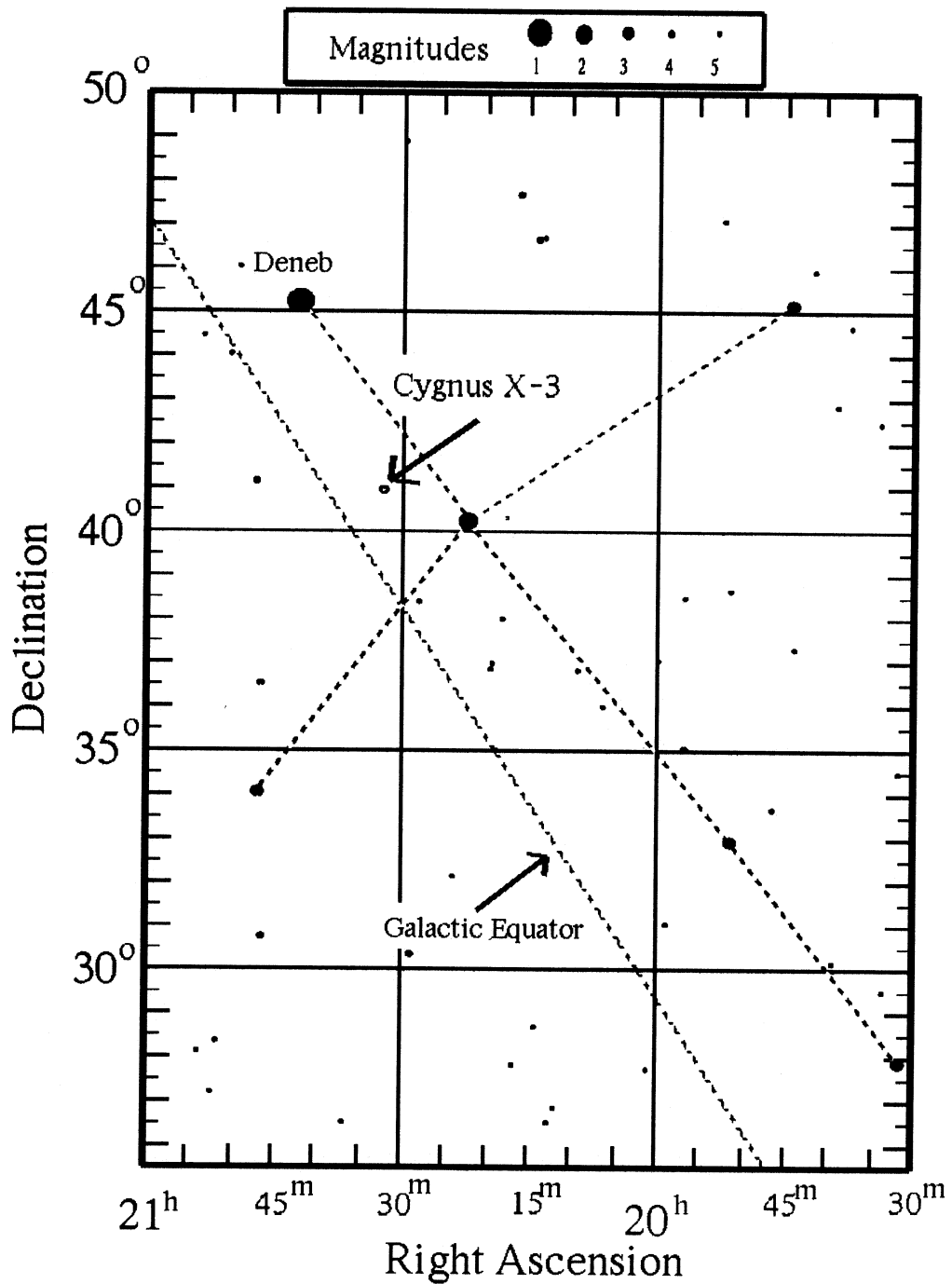
Figure 2.1.1: The location of Cygnus X-3 in the Summer Constellation Cygnus. Cygnus X-3 is located near the galactic equator

where M is the combined mass of the neutron star and the companion star in solar masses.[5]

2.2. X-ray Models of the Cygnus X-3 System

There have been many theoretical models constructed to try to explain the X-ray modulation and spectrum of Cygnus X-3. These models prove to be most successful at X-ray energies less than about 50 KeV.[1] Three of the most commonly cited X-ray models are the cocoon model,[7] stellar wind model,[5] and the accretion disk corona model.[6] Only a brief descriptive summary of each model will be given. More detailed and mathematical descriptions of these models can be found in the sources cited above.

2.2.1. Cocoon Model

The cocoon model has the binary Cygnus X-3 system surrounded by a shell of matter, called a cocoon, extending $\approx 10^{12}$cm from the center of the system. The cocoon is believed to have been formed by evaporating from the companion star by X-ray heating. The cocoon model assumes a binary pulsar system, with a fast $10 - 30$ms pulsar in close orbit around a nondegenerate noncompact companion.[7] The model predicts a modulation caused by a rotating shadow cast onto the shell by the motion of the orbiting companion.[1] It reproduces many major observational features of the Cygnus X-3 system, including the complete eclipse observed in the γ-ray spectrum, and the smoothed out eclipse observed in the infrared and X-ray spectrum. Irregularities in the light curves can be

explained with the addition of an eccentric orbit. In addition, the pulsar-shell system may be slightly unstable, which may cause an unpredictable variability in the output of the system. This may be an easy explanation for the large radio outbursts observed from the Cygnus X-3 system. One major problem with the model is that it incorrectly predicts that the $2-10$ KeV modulation is produced by energy independent Compton scattering, which would show a modulation depth that does not vary with energy.[1] Another problem with the model is, as Milgrom states, "developing a detailed self-consistent physical model for the shell."[7]

2.2.2. Stellar Wind Model

A second X-ray model developed for the Cygnus X-3 binary system is the stellar wind model. In this model, the X-ray emitting neutron star is embedded in a dense stellar wind originating from the companion star in a spherically symmetric fashion.[1] X-ray modulation is produced by the gradual and partial eclipsing of the compact X-ray object by the stellar wind originating from the companion star.[5] The eclipsing would cause changes in the scattering optical depth along the line of sight between the X-ray source and the observer, and thus would create a smoothly varying modulation in the observed flux.[7] This stellar wind would also supply the necessary mass transfer required to power the X-ray source.[5] This model is very successful in predicting the X-ray light curve; however, it fails to agree with other observations. It predicts that the infrared light curve would be unmodulated, where Bremsstrahlung emission

of the hot wind would account for most of the observed infrared flux.[1] It also predicts that the γ-ray modulation should be greatly reduced, since the scattering opacity is smaller there.[7] Both of these predictions are in direct contradiction to observation. Attempts to modify the model to correct these inconsistencies have been made, but often create even more contradictions.[7]

2.2.3. Accretion Disk Corona Model

A third X-ray model for the Cygnus X-3 system is the accretion disk corona model. In this model, the neutron star is surrounded by an optically thick cloud of gas, called a corona, that evaporated from the surface of an accretion disk. A sinusoidal modulation is produced from the partial occultation of the accretion disk corona by a bulge in the accretion disk which is caused by inflowing material. The bulge is believed to be the compact source of X-rays for this system. This model appears to best reproduce the X-ray light curve,[1] and bulges and irregularities in the accretion disk can be added to reproduce small asymmetries in the X-ray light curve. For example, the minimum of the X-ray light curve remains constant, but is known to have a steeper fall than climb. This can be corrected with azimuthal variation in the height of the outer edge of the accretion disk, so the occultation of the bulge creates a modulation that is not quite sinusoidal, and better fits the observed light curve.[6] One flaw of this model is that it predicts that the phase modulation is independent of energy; however, this may be corrected for by the addition of a vertical density gradient.[1]

2.3. Accelerating Mechanisms for the Cygnus X-3 System

The X-ray models described above explain the X-ray production by the Cygnus X-3 system. γ-rays have been observed from the Cygnus X-3 system with energies $\geq 10^{16}$eV, and need to be accounted for in these models. Therefore, models have been constructed explaining the production of these high energy γ-rays within the confines of the X-ray models. It is believed that protons interacting in the companion star's atmosphere produce either pions or neutrons, depending on which model is being used, which in turn produce the γ-rays. For this to happen protons must be accelerated to $\approx 10^{19}$eV.[3] Three models have been suggested to account for this accelerating mechanism. They are the pulsar acceleration model,[2] the diffuse shock acceleration model,[8] and the accretion disk acting as a dynamo model.[4] Again, only a brief descriptive summary will be given for each model, and more mathematical and detailed descriptions can be found in the sources listed above.

2.3.1. Pulsar Model

In the pulsar acceleration model, the protons are accelerated by the rotating neutron star's magnetosphere.[3] Here particles accelerated near the pulsar strike the atmosphere of the companion, where they form bremsstrahlung γ-rays,and π^o particles that can decay into γ-rays. The acceleration region in this model is pointlike, and the particle trajectories are straight lines outside of the acceleration region.[2] This model may work in magnetic fields up to $\approx 10^{12}$G.[1] The Ultra-high energy light curve can be reproduced, and pulses could be

as narrow as the observed 5% of the period.[2] The model requires that the the Cygnus X-3 system contain a fast pulsar with a period on the order of milliseconds. This fact seems to be supported by the fact that a 12.59 ms pulsation has been detected from the Cygnus X-3 system; however, observations of some other X-ray binaries, with slowly rotating neutron stars, also show high energy radiation equivalent to that observed in the Cygnus X-3 system. This fact has made many physicists skeptical of this model.

2.3.2. Diffuse Shock Acceleration Model

The diffuse shock acceleration model uses accretion as the energy source, and shock acceleration of ions as the mechanism responsible for the production of the high energy particles that produce the observed γ-ray emission. The ions are accelerated by a collisionless shock formed by the accretion of matter falling toward the surface of the neutron star. The accelerated ions produce neutrons by the high energy proton-proton collisions, and the photodissociation of the ultra-high energy ^4He nuclei. The neutrons then strike the companion star's atmosphere producing the narrow phase ultra-high energy γ rays. The neutrons are essential in this model, since they allow the transfer of energy without placing additional restrictions on the magnetic field configuration.[8] One problem with this model includes the fact that the maximum reachable energy, using this acceleration mechanism, is smaller than the $\approx 10^{19}$eV protons being produced unless the magnetic field is $\leq 10^8$G.[1]

2.3.3. Accretion Disk Acting as a Dynamo Model

The accretion disk acting as a dynamo model uses the accretion as the source of the energy for the acceleration. Here the magnetic field, which is assumed perpendicular to the particle flow, is magnified by the differentially rotating accretion disk. It is then assumed that the accreting material is highly conducting, and produces a radial electric field ($\vec{E} = \vec{v} \times \vec{B}$)which is responsible for the acceleration.[3] This acceleration aids proton-proton collisions in the companion star's atmosphere or other circumstellar gaseous material, which can create π^o particles which can decay into γ-rays.[4] Positive points of this model include the creation of a large electric potential over an extended region without an extremely large magnetic field, and an energy source that could last for a significant amount of time. One major problem with the model is that the predicted γ-ray flux would not have a significant modulation due to the symmetry of the emission. However, Brecher suggested that a highly inclined magnetic axis for the neutron star could produce the asymmetry in the particle beam that could produce the modulations.[4] Another problem with this model is that it could not account for all of the observed energy of the system if the magnetic field is $\geq 10^9$G.[1]

2.4. Cosmic Rays

The particles produced in the Cygnus X-3 system travel through a distance of $\geq$ 10 kpc before striking the Earth's atmosphere. There is also an omnidirectional background of highly energetic cosmic rays, whose origin is not

completely understood, striking the Earth's atmosphere at the same time. As a result of this, in the direction of Cygnus X-3 there is only a small excess of particles, over the background rate, that are actually coming from the Cygnus X-3 system. The cosmic rays that first strike the atmosphere are called cosmic ray primaries. These primaries produce a cascade of secondary particles produced in collisions with atmospheric nuclei. Some of these secondary particles can penetrate the Earth's atmosphere, and even far underground, where they can be detected with cosmic ray telescopes. Cosmic ray primaries can be any of a variety of particles, including protons, neutrons, γ-rays, nuclei, and photons. Much of the background is produced from hadronic showers and electromagnetic showers produced from hadron and photon primaries respectively. One topic of great controversy in recent years has been the identity of the primary cosmic rays that originate from Cygnus X-3.

2.4.1. Air Shower Production of Cosmic Ray Secondaries

The hadronic shower is produced when the primary cosmic ray interacting with the upper atmosphere is a hadron, which can be a proton or heavier nucleus.[9] Collisions of the hadron with nuclei in the upper atmosphere produce pions. The neutral π^o particles decay into photons, which produce an electromagnetic cascade of electrons and photons. The other two varieties of pions decay into charged muons and neutrinos ($\pi^{\pm} \rightarrow \mu^{\pm} + \nu$). This is the penetrating part of the shower. The positive and negative charged muons and associated neutrinos are of interest, since they can penetrate large

amounts of atmosphere, rock, and ground cover. These particles are able to penetrate so effectively since they are leptons, and thus are impervious to nuclear interactions.[9] The charged muons are of special interest, since they can be detected in sea level and underground cosmic ray telescopes due to their charge. Muons are very much like electrons and positrons, except they are about 200 times as heavy.

A second type of interaction producing cosmic ray secondaries is the electromagnetic shower, where the primary cosmic ray is a photon. The secondary particles in the cascade are mostly electrons, positrons, and photons produced in electromagnetic pair production and bremsstrahlung interactions with the coulomb fields in the atmospheric nuclei. This interaction is not as significant as the previous one for muon production, since the number of muons produced in this type of interaction is belived to be more than one order of magnitude smaller than the number of muons produced by hadronic showers.[9]

Both types of showers proceed rapidly, where the number of particles grows almost exponentially and the average energy of each particle in the cascade likewise decreases. Most showers do not have enough energy to reach the ground. To reach sea level, the primary cosmic ray that started the cascade must have an energy $\geq 10^{14}$eV. Most of the charged particles in the cascades that make it to the ground are muons.

2.4.2. Parent Particle of Muon Showers from Cygnus X-3

One topic of great debate centers on the identity of the parent particle, or cosmic ray primary, coming from Cygnus X-3 that produces the cascades in the atmosphere that generate the observed muon flux. To account for the overabundance of muons seen from the direction of Cygnus X-3, the parent particle must be neutral, since the 10^{-6}G galactic magnetic field would deflect any charged particles. It also needs to have a long enough lifetime to make the 10^4 year journey from Cygnus X-3, be energetic enough to produce cascades that yield muons that can be measured by underground detectors, be numerous enough to reproduce the observed muon fluxes, and somehow be able to maintain its phase coherence. No known particle can seem to account for what is observed.

Hadrons cannot be the parent particle, since no known neutral hadron has a lifetime long enough to survive the 10^4 year travel from Cygnus X-3 to the Earth.[9] Protons are further excluded because of their charge.

Neutrinos can be excluded, since they are believed to rarely make showers in the atmosphere.[9] They also are excluded by their zenith angle distribution. The muons from Cygnus X-3 display a cos^2 (*Zenith angle*) distribution, and if the primary were a neutrino, then the distribution would be independent of zenith angle. Also, the muon flux generated by the neutrino primaries is believed to fall short of the observed muon flux by two orders of magnitude.[1]

Photons are a possible candidate for the parent particle. Photons could produce showers that could point back to Cygnus X-3, but the number of muons

produced in a photon induced shower would not account for the large flux of muons observed.[9] It has been calculated that primary photons would have to be ≈ 1 TeV to reproduce the observed surface flux. This is unlikely, since a muon needs on the order of 600 GeV to reach some of the underground muon telescopes. If the energy of the primary is increased to account for this, then the calculated surface flux is off by two orders of magnitude.[10] It has been suggested that 10^{14}eV γ-rays could produce the observed flux if its nuclear cross section were much larger than the standard model of elementary particles dictates.[9]

Neutrons are another possible canadate for the parent particle. They are neutral, and would produce muon-rich air showers.[8] One problem with neutrons is that they only have an $\approx 10^3$ second lifetime. This means that the neutrons would have to have energies $\geq 10^{18}$eV for Lorentz time dilation to prolong their lifetimes long enough to reach Earth. The flux of all known cosmic rays above this energy would only produce approximately one muon event per year in Soudan-1; however, Soudan-1 records approximately 180 events per year from the direction of Cygnus X-3.[10]

The failure of any of the known cosmic ray primaries to reproduce the observed muon fluxes from Cygnus X-3 has led many physicists to believe that there is either some unknown mechanism at work, or the primary particle coming from Cygnus X-3 is a new undiscovered particle. This particle, if it exists, is called a cygnet. The cygnet would be a neutral particle with a long enough lifetime to travel from Cygnus X-3 to the Earth. It would have a large cross section for direct and indirect muon production. The addition of this

new particle, or new unknown interaction, would require energy calibration adjustments in air shower experiments, and could drastically change cosmic ray physics.[10]

Chapter 3
Muon Astronomy

When searching for a signal from an astronomical source, it is important to be able to tell what direction in relation to the stars the signal is coming from. We must be able to calculate the apparent directional origin of muons striking our detector, so that we can see which muons striking the detector are coming from the direction of Cygnus X-3. To do this one must be able to convert from a set of local time and coordinate systems that are relative to the observer, to a set of astronomical time and coordinate systems that are relative to astronomical sources. Also, since there is always a background flux of muons from background cosmic rays, one must be able to show statistically that the number of events seen coming from the expected source is significantly larger than the number of background events seen in other directions.

3.1. Astronomical Coordinate Systems

The first step involved in pointing muon tracks back to an astrophysical source like Cygnus X-3 is converting between the coordinate systems used in astronomy. There are four celestial coordinate systems that astronomers use to locate the positions of objects. They are the horizon, equatorial, ecliptic, and galactic systems. All four are spherical coordinate systems, and are defined by the following points. Each system must have a reference plane, sometimes

called a great circle, that defines the orientation of the coordinate system. Also, a certain point in the reference plane, that acts as the origin, must be defined, along with one of the poles of the circle, which is the origin of colatitude. Astrophysical coordinate systems may be topocentric, geocentric, or heliocentric, depending on whether the system is observer-, Earth-, or Sun-centered. In addition, since both right handed and left handed systems are used in astronomy, a sense of helicity must also be defined.[11] Figure 3.1.1, based on Figure 3.1 in Thomson, shows the orientations of the reference planes used in the coordinate systems mentioned above.[3]

The positions of the objects in all four coordinate systems are mapped on the celestial sphere, which is an imaginary Earth-centered sphere onto which all astrophysical objects are projected. The celestial equator, and celestial north and south poles, are extensions of the Earth's equator, and north and south poles. The apparent path of the sun on the celestial sphere is known as the ecliptic, and is inclined with respect to the celestial equator by $\approx 23.5°$. The points where the ecliptic and celestial equator intersect are called the autumnal and vernal equinox, and mark the beginning of fall and spring respectively in the northern hemisphere.[11]

3.1.1. Horizon System

The horizon coordinate system is a topocentric system that is defined relative to the observer. The reference plane is defined to be the plane of the observer's horizon, which is defined as the plane normal to the local
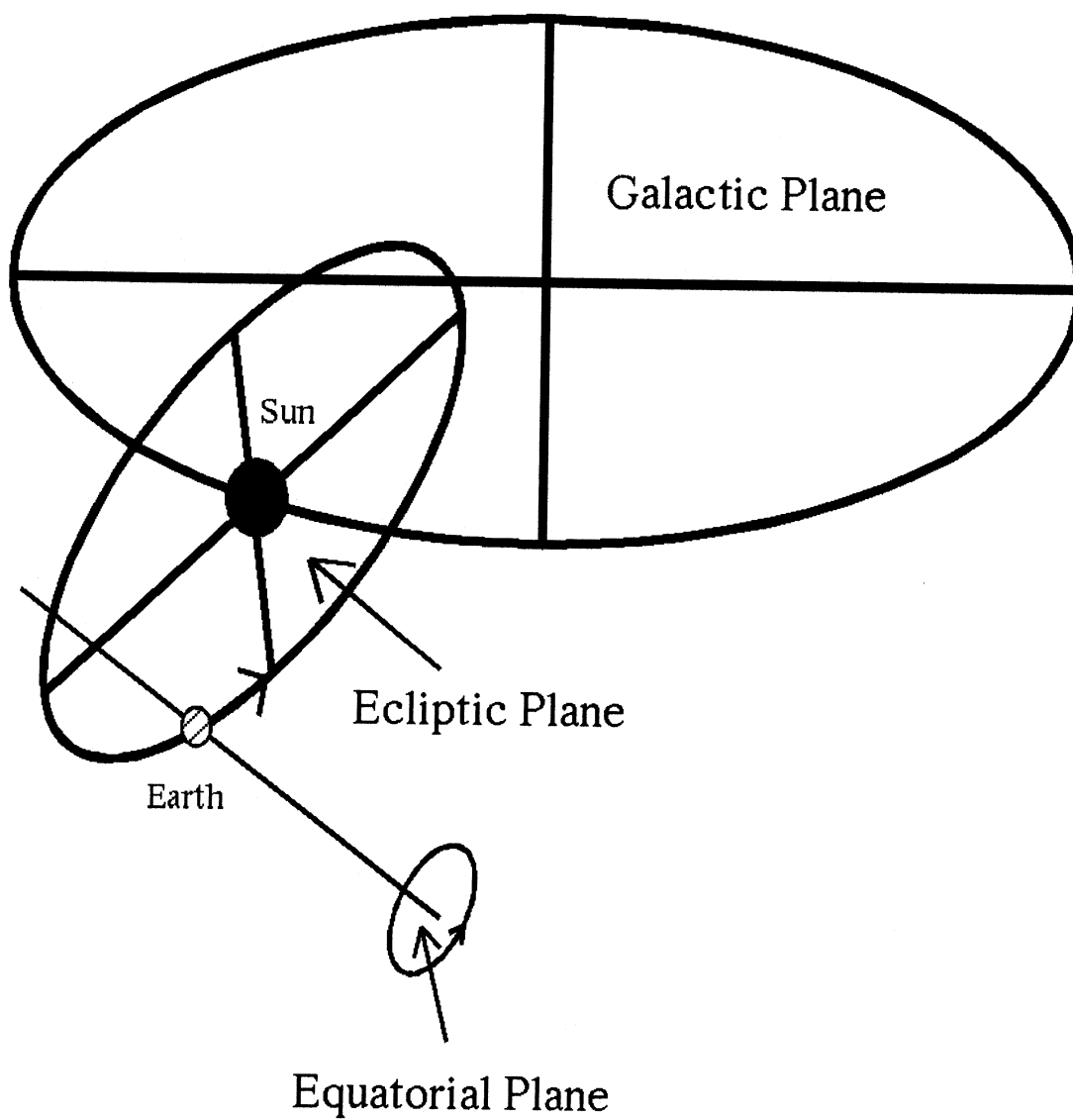
Figure 3.1.1: A pictorial representation of the relationship between the various astrophysical coordinate systems. This figure is based on Figure 3.1 in Thomson.

gravitational field. Directions in this system are defined by an altitude angle, $\vec{a}$, and a azimuthal angle, $\vec{A}$. $\vec{a}$ varies from $0 - 90°$, has the reference plane as its origin, and is defined as the angular distance above the horizon. $\vec{A}$ varies from $0 - 360°$, has the meridian as its origin, and is a measure of angular distance east of the meridian. The meridian is the great circle that connects the zenith point with geographic north. Since $\vec{A}$ is measured positive eastward, the helicity of the system is left. The stars appear to move in the sky due to the rotation of the Earth; therefore, the $\vec{a}$ and $\vec{A}$ coordinates of astrophysical sources change with time. This limits the usefulness of this system when dealing with astrophysical sources.[11]

3.1.2.   Equatorial System

The equatorial coordinate system is a geocentric system that is defined relative to the Earth, where the reference plane is defined by the plane of the celestial equator. Directions in this system are defined by declination, δ, and right ascension, α. δ varies from $0 - \pm90°$, has the reference plane as its origin, and is defined as the angular distance above $(+\delta)$ or below $(-\delta)$ the celestial equator. α is measured in sexagesimal hours, varies from $0 - 24$ hours, and has the rising of Ares, Υ, as its origin. Υ is the position of the vernal equinox on the celestial sphere, and α is measured positive eastward, making this a right-handed system. The equatorial system follows the path of the stars, so that a fixed star will maintain the same δ and α. This system is ideal for locating the position of objects in relation to the stars.[3,11]

3.1.3. Ecliptic System

The ecliptic coordinate system is a heliocentric system that is defined relative to the sun. The reference plane is defined by the plane of Earth's motion around the sun, or the ecliptic. Directions in this system are defined by ecliptic latitude, β, and ecliptic longitude, λ. β varies from $0 - \pm 90$, has the reference plane as its origin, and is defined as the angular distance above or below the ecliptic. λ varies from $0 - 360°$, has the direction Υ as its origin, and is defined as the angular distance measured from Υ. λ is measured positive eastward, and is thus a right-handed system. Since most objects in the our solar system follow paths close to the ecliptic, this is a useful coordinate system for dealing with objects inside the solar system.[3,11]

3.1.4. Galactic System

The galactic coordinate system is defined relative to the Milky Way galaxy. The reference plane is the plane of our galaxy that when projected on the celestial sphere forms the galactic equator. The angle between the galactic equator and the celestial equator is $\approx 63°$, and the galactic north pole is located at equatorial coordinates $\alpha = 12^h 49^m$ and $\delta = +27°24'$. Directions in this system are defined by galactic latitude, $\vec{B}$, and galactic longitude, $\vec{L}$. $\vec{B}$ varies from $0 - 90°$, has the reference plane as its origin, and is defined as the angular distance above or below the galactic plane. $\vec{L}$ varies from $0 - 360°$, has the line joining the sun and galactic center as its origin, and is defined as the

angular distance east of its origin. Galactic coordinates are used to measure the position of objects in our galaxy.[3,11]

3.2. Astronomical Time Systems

To point muon tracks back to astrophysical sources, one must not only be able to convert between astrophysical coordinate systems, but also between astrophysical time scales. The rotation of the Earth around the sun results in different stars being visible at different times of the year. This translates to a difference between the solar day and the sidereal day, which leads to two different time scales. Time based on the solar day is called universal time, whereas time based on the sidereal day is called sidereal time. Another time scale called the Julian date defines all observations with respect to some time defined as zero.

3.2.1. Solar and Sidereal Days

The solar day is used to keep track of the sun, and is the time scale that we base our lives on. The mean solar day is the average time between two successive transits of the sun, and is equal to exactly 24 hours. The Earth moves faster when at perihelion than when at aphelion, and the rotation rate is constant; therefore, the time between successive transits is not constant. The time between transits is averaged over an entire year, and this quantity is defined as the mean solar day. The sidereal day is used to keep track of the stars, and is defined as two successive transits of a star. The sidereal day is

equal to $23^h56^m4^s.09$, which is about four minutes shorter than the solar day. This means that a certain star will rise four minutes earlier each day, or be offset by about $1°$ at the same time on consecutive days. These two time scales are the bases for universal time and sidereal time.

3.2.2. Universal and Sidereal Time

Universal time (UT) is the timescale on which all civil timekeeping is based, and has units of seconds. $UT1$ is universal time corrected for polar motion, and UTC is coordinated universal time , and is the time that is broadcast and received on a $WWVB$ receiver. The difference between $UT1$ and UTC is called $DUT1$ and is kept less than $0^s.90$ seconds by the addition of leap seconds at the end of June or December. $DUT1$ is broadcast along with UTC.

The Greenwhich mean sidereal time (GMST) is the sidereal time on the Greenwhich meridian, that is at zero longitude. The Greenwhich mean sidereal time can be calculated from $UT1$ using the following equation,

$$GMST \ of \ 0^hUT1 = 6^h41^m50^s.54841 + 8640184^s.812866T$$
$$+ 0^s.093104T^2 - 6^s.2 \times 10^{-6}T^3$$

(3.2.1)

where T is measured in Julian centuries of $36,525$ days of $UT1$ from January 1, 2000 at 12 hours $UT1$. This corresponds to a Julian Day of 2451545.0 $UT1$.[11] The Julian Day (JD) is a timescale used by astronomers that is related to universal time, and has an arbitrary offset so that a predetermined time is set equal to zero. $JD = 0$ at 12^h UT on January 1, 4713B.C.. This time was chosen so that no observation or calculation would involve a negative time.[3]

Local mean sidereal time ($LMST$) is the sidereal time at a longitude λ, and can be calculated from $GMST$ as follows,

$$LMST = GMST - \lambda \qquad (3.2.2)$$

So, in astrophysical calculations, the conversion between UTC and $LMST$ is made to help locate a particular object. A worked out example of time and coordinate transformations for a typical astronomy application can be found in Kochocki.[11]

Sidereal noon for a particular astrophysical object occurs the instant when it crosses the meridian. At some time later, the star has moved, and the hour angle is defined as the degrees or hours of arc the star is from the meridian. At sidereal noon the hour angle is equal to zero. The hour angle is measured positive westward from 0 to 12^h, and negative eastward from 0 to -12^h. The hour angle information and sidereal noon of an astrophysical object shows when the object of interest is visible in the sky.[11,12]

3.3. Pointing Muon Tracks Back to Cygnus X-3

Once the astrophysical locations of muon tracks striking the detector have been determined, then the problem becomes assessing the significance of any excess of events that we may see from a source region over the background rate. Marshak writes, "The identification of Cygnus X-3 as a source relies on both the shower arrival direction and the observation of a flux enhancement in a phase plot with use of Cygnus X-3's characteristic 4.8 hour period."[10] The first

part of Marshak's statement suggests that the first component in looking for a source like Cygnus X-3 is verifying that the event rate coming from the direction of Cygnus X-3 is greater than that in a non-source direction. This is done by windowing. A window of a certain predetermined size centered on Cygnus X-3 is opened and the number of events in this window is compared to other windows pointing in other directions to determine if a DC excess exists in the direction of Cygnus X-3. The second part of Marshak's statement suggests that if a 4.8 hour periodicity can also be associated with the events in the window centered on Cygnus X-3, then it further strengthens the arguement that the excess signal is coming from there, since the known orbital period of the system is 4.8 hours. This analysis is done with phase histograms that show the number of events arriving from the direction of Cygnus X-3 in each part of the system's orbit. For the above two parts of the analysis we draw heavily on the work done by Nagle,[13] and Li and Ma.[14] To calculate what part of the orbit of Cygnus X-3 each event is coming from requires a knowledge of the system's orbital behavior. This is accounted for in the ephemeris provided by M. van der Klis and J. M. Bonnet-Bidaud,[15] and is common to all of the experiments mentioned hereafter. An additional complexity in calculating the phase of each event is that there needs to be a barycenter correction that accounts for the change in distance between Cygnus X-3 and the Earth, due to the Earth's orbit around the sun. A Fortran program written by Ken Johns, from the University of Arizona, and modified by myself, makes the necessary astrophysical, background, and phase calculations.[12]

3.3.1. Search for a DC excess

The following follows closely work done by Nagle[13], and Li and Ma.[14] When looking for a signal from a point source at equatorial coordinates α_o and δ_o, one must open up a $\theta°$ window, called a circle or ellipse of resolution, that is centered on that source. Circular windows can be utilized when the detector resolution is the same in all directions, and elliptical windows can be used when the detector has unequal resolutions in two different coordinates. Any events that fall within the window are counted in the on-source count N_{on}. In order to measure the background rate, an analysis identical to the on-source analysis is preformed. $(K-1)$ other $\theta°$ windows are opened, and events that fall within these regions contribute to the off-source count N_{off}. The off-source windows should be located at,

$$\alpha_i = \alpha_o + \frac{i}{K} \times 24 \ hours$$
$$\delta_i = \delta_o$$

$$(3.3.1)$$

with $i = 1, 2, 3, ..., (K-1)$. Here K is chosen so that the windows do not overlap for the largest zenith angle at which the data is taken. Also, it is important to note that in Eq. (3.3.1) the off-source windows are all located on the same declination band as the on-source window. This is done because the detector sensitivity is only uniform in right ascension, and all of the windows will then pass over the same overburden.[13]

The ratio of on-source to off-source exposures can be given by,

$$\xi = \frac{< A_{eff} \Omega t >_{on}}{< A_{eff} \Omega t >_{off}}$$

$$(3.3.2)$$

where N_{on} events are collected at times t_{on}, and N_{off} events are collected at times t_{off}. Ω_{on} and Ω_{off} are the solid angle subtending the on-source window, and the total solid angle subtending the off-source windows, respectively. Also, A_{eff} is the effective area of the detector for cosmic rays.[13]. When the response of the detector is taken into consideration, then Eq. (3.3.2) can be approximated by,

$$\xi \simeq \frac{\int \int \varepsilon(t) \, A_{eff}\{E, \theta(\alpha_o, \delta_o, t)\}\Omega\{(\alpha_o, \delta_o, t) \, I_{CR}(E) \, dE dt}{\sum_{i=0}^{K-1} \int \int \varepsilon(t) \, A_{eff}\{E, \theta(\alpha_i, \delta_i, t)\}\Omega\{(\alpha_i, \delta_i, t) \, I_{CR}(E) \, dE dt} \qquad (3.3.3)$$

where the "o" subscripts represent the on source region, and the "i" subscripts represent the $K - 1$ off-source regions. $\varepsilon(t)$ equals 0 or 1 depending on whether the detector was operational at that time. The effective area, A_{eff}, is a function of energy E, and zenith angle θ. The zenith angle is a function of the equatorial coordinates α and δ, and of the time t. The solid angle, Ω, is also a function of zenith angle. I_{CR} is the cosmic ray differential intensity. If the detector downtime is uniformly distributed in time, then we can approximate Eq. (3.3.3) by,

$$\xi \approx \frac{1}{K - 1} \qquad (3.3.4)$$

The maximum-likelihood estimate of the background count in any window then becomes,

$$\hat{B} = \xi N_{off} \qquad (3.3.5)$$

and the maximum-likelihood estimate of the source count in the on-source window is,

$$\hat{N}_s = N_{on} - \hat{B} \qquad (3.3.6)$$

The statistical significance of any excess of events in the source window can be tested using the maximum-likelihood statistic λ which can be written as,

$$\lambda = \left\{ \left[\frac{\xi}{1+\xi} \right] \frac{N_{on} + N_{off}}{N_{on}} \right\}^{N_{on}} \left\{ \left[\frac{1}{1+\xi} \right] \frac{N_{on} + N_{off}}{N_{off}} \right\}^{N_{off}} \qquad (3.3.7)$$

Nagle states that $-2ln\lambda$ is distributed as $\chi^2(1)$ asymptotically, and the significance of the observation in standard deviations is,

$$S = \sqrt{-2ln\lambda} \qquad (3.3.8)$$

Many experiments calculate the statistical significance of events differently, but these methods are less flexible. They compare N_{on} with $\hat{B}$, and calculate the probability for the observed excess using the Poisson formula, or from the observed excess in standard deviations,[14]

$$S = \frac{\left(N_{on} - \hat{B} \right)}{\sqrt{\hat{B}}} \qquad (3.3.9)$$

Nagle points out that these approaches are only valid if $\xi \ll 1$, and assumes that there is almost no uncertainty in the background estimate. Also, in the method using Eq. (3.3.9) $\hat{B}$ must be very large.[13] These methods are not preferred, since the number of events recorded in typical muon experiments is very small. This means that there is usually significant uncertainty in the background rate, and $\hat{B}$ is small.

3.3.2. Phase Histograms

Due to the small number of events over background observed by muon experiments, the significance using the windowing method in the above section is usually very small. Therefore, we must find a way to ensure that the events over background are coming from the source, and not from a statistical fluctuation of the background events. Marshak stresses, "The ability of a detector to separate the signal of an x-ray binary system from a random background is considerably enhanced by the source periodicity."[17] This suggests that if we can associate the source periodicity with the events in the window centered on Cygnus X-3, then this will enhance significance of our results. As mentioned earlier, the Cygnus X-3 system has a known 4.8 hour period that is well documented in X-ray data. We can create a phase, that ranges from $0 - 1$, that is folded with the 4.8 hour period of the Cygnus X-3 system. Here a minimum in the x-ray light curve occurs at a phase of 0, and broad maximum occurs at a phase of ≈ 0.65. The phase tells us where in the orbital cycle the Cygnus X-3 system is at any time, so if we know the time that a muon struck the detector from the direction of Cygnus X-3, then we can associate a phase with that event. If a small excess of events in a window centered on Cygnus X-3 accumulates events uniformly over all phases, then it would be expected that the events were just random background events. However, if the excess of events accumulate with a peak in phase of around 0.65, then it would be expected that the events were actually coming from Cygnus X-3, since they then would have exhibited the same periodicity seen in the x-ray data.

So the arrival times t_i of events are converted to phases ϕ_i by,

$$\phi_i = \frac{(t_i - T_o)}{P_o} - \frac{\dot{P_o}(t_i - T_o)^2}{2P_o^2} - \frac{\ddot{P_o}(t_i - T_o)^3}{6P_o^2} \qquad (3.3.10)$$

where T_o is the time of x-ray minimum, P_o is the period of the Cygnus X-3 system, $\dot{P_o}$ is the time rate of change of the period, and $\ddot{P_o}$ is the time rate of change of $\dot{P_o}$.[13] Eq. (3.3.10) is called the cubic fit phase equation. Some experiments use the parabolic fit phase equation to calculate the phase, which is just Eq. (3.3.10) with $\ddot{P_o} = 0$.

It is customary in muon experiments to bin the data in histograms, sometimes called "phaseograms". The bins are usually of size 0.05 or 0.1 in phase, and maximum in these phase histograms is expected to be in the area of $0.65 - 0.90$ in phase. Nagle suggests that if there is a large number of events, then the number of events over background can be tested using the χ^2 test. The number of events in a window centered on Cygnus X-3 is usually small, however, so the significance is usually tested using N_{max} as the test statistic. When $\xi \ll 1$, then the Poisson distribution can be used to calculate the significance.[13]

The off-source windows can be used to help calculate the background for each phase bin. For, example the background estimate of the ith phase bin, $\hat{B_i}$ can be calculated by multiplying the number of off-source background events in the ith phase bin by ξ. The phases of the off-source background events are calculated using Eq. (3.3.10) in the same manner as those in the on-source window, but with one exception. For the $K-1$ off-source windows, at positions

defined in Eq. (3.3.1), the time epoch, T_o must be shifted to,

$$T_o\left(i\right) = T_o + \left(\frac{24i}{K}\right) \times 0.0415529 \; days \qquad (3.3.11)$$

This shifts T_o by $\frac{1}{24}$ of a sidereal day for every one hour of right ascension. This insures that any zenith angle effects affecting the source region will affect the background regions in the same phase.[13] This correction is particularly important with Cygnus X-3, since the orbital period of the system is very close to $\frac{1}{5}$th of a solar day. The consequences of this are that measurements taken without the Eq. (3.3.11) correction will tend to accumulate particular energies at particular phases over a month's time. Another complication is that there is an observed 34-day x-ray variation, and this is similar to the period of the lunar month, which further complicates the phase-linked energy dependence.[18]

Nagle further suggests that the probability of observing fewer than N events in the ith phase bin of the on-source window is,[13]

$$P_r\left(n < N_{max}; ith \; bin\right) \simeq exp\left(-\hat{B}_i\right) \sum_{n=0}^{N-1}\left(\frac{\hat{B}_i^n}{n!}\right) \qquad (3.3.12)$$

and if there are M phase bins, the probability of observing fewer than N_{max} events in all bins is,[13]

$$P_r\left(n < N_{max}; all \; M \; bins\right) \approx \prod_{i=1}^{M} P_r\left(n < N_{max}; ith \; bin\right) \qquad (3.3.13)$$

A critical value for N_{max} can be calculated at the desired confidence level. If the null hypothesis is that the phase distribution is consistent with background, then it may be rejected if N_{max} exceeds the critical value. Nagle also suggests that, if ξ is not much less than 1, then the maximum-likelihood ratios, used in

the previous section when searching for a DC excess of events, can be applied to the calculation of the phase bin significance.[13]

3.3.3. Ephemeris of Cygnus X-3

In order to calculate the phase, ϕ_i, for an event striking the detector at a time, t_i, using Eq. (3.3.10), there are four orbital parameters that must be known. These four parameters describe the periodicity of the system, and are the orbital period P_o, the time rate of change of the orbital period $\dot{P}_o$, the time rate of change of the time rate of change of the orbital period $\ddot{P}_o$, and the time of x-ray minimum T_o. These parameters make up what is called the ephemeris of the system. Most muon experiments cite an ephemeris calculated from x-ray data by van der Klis and Bonnet-Bidaud in 1981.[15] The ephemeris was improved in 1988 by van der Klis and Bonnet-Bidaud by analysing 15 years of x-ray data taken by the EXOSTAT observatory starting in 1970.[16] The differences in these two ephemeri are small for the years $1981 - 1984$, and slowly start to diverge at around the year 1985. Both the 1981 parabolic and 1988 cubic ephemeris values are shown below in Table 3.3.1.[16] There are also other ephemeri, whose values are slightly different than the ones calculated by van der Klis and Bonnet-Bidaud; however, they are not used often.[3] When comparing the results from different muon experiments, it is important to use the same ephemeris for consistency.

Table 3.3.1: Cubic and Parabolic ephemeris values for Cygnus X-3 calculated by van der Klis and Bonnet-Bidaud in 1988 using x-ray data from the EXOSTAT observatory. The units of T_o are heliocentric Julian Days

Parameter	Cubic Fit	Parabolic Fit
P_o $(Days)$	$0.19968354 \pm 0.00000015$	$0.19968354 \pm 0.00000015$
$\dot{P}_o$	$(2.18 \pm 0.320) \times 10^{-9}$	$(0.94 \pm 0.048) \times 10^{-9}$
$\ddot{P}_o$ (yr^{-1})	$(-0.16 \pm 0.04) \times 10^{-9}$	0.00 ± 0.00
T_o $(J.D.)$	2440949.8962 ± 0.0009	2440949.8962 ± 0.0009

3.3.4. Barycenter Correction for Cygnus X-3

There is one other correction that must be made when calculating the phase of a muon event from Cygnus X-3. Since the Earth revolves around the sun, and light takes $\approx$ 8 minutes to get from the sun to the Earth, the time that it takes light from an astrophysical source to reach the Earth may vary by as much as 16 minutes over the course of the year. The exact variation in arrival time depends on the angle between the direction of the source and the plane of the solar system. This variation can be eliminated by calculating the phase at a point in space that is at a constant distance to Cygnus X-3. The solar system barycenter can be used as this point. If the effects of all of the planets on the solar system barycenter are considered negligible, then the center of the sun, or heliocenter, can be used instead. Thomson calculates the change to the barycenter by adding Jupiter to the solar system, and shows that this difference

would create a negligible difference in arrival times when compared to the 4.8 hour period. However, Thompson stresses, that if an experimenter were trying to observe the millisecond pulser that is believed to be at the core of the Cygnus X-3 system, then the barycenter variations caused by all of the planets would have to be calculated, along with the variations in the orbital motions of the Cygnus X-3 system.[3]

3.3.5. Ken Johns Analysis Program

A Fortran program written by Ken Johns, and modified by myself, makes the calculations laid out earlier in this chapter. For every muon track the altitude and azimuth angles are calculated, along with the right ascension and declination angles, from the angle that the track strikes the detector. The time quantities such as Julian Day, Greenwhich Mean Sidereal Time, and Local Mean Sidereal Time are calculated from the Universal Time received on a WWVB receiver. This includes the barycenter correction that makes the arrival times of the cosmic rays independent of Earth's motion.[12]

A $10° \times 1°$ elliptical window is opened centered on Cygnus X-3, with the ellipse size corresponding to the detector resolution as will be discussed later. The program then calculates the phase using Eq. (3.3.10) and the ephemeris in Table 3.3.1 for events falling in that window. Three other similar phase histograms are created for equal sized windows with momentum cuts of 10 GeV/c, 25 GeV/c, and 100 GeV/c.

Some of my additions to the program include addition of the search for a DC excess, and the addition of the background calculations. In addition to the $10° \times 1°$ elliptical window centered on Cygnus X-3, I added 35 off-source windows spaced every $10°$ as shown in Eq. (3.3.1). For the background calculation I used the methods outlined in Eqs. (3.3.4) through (3.3.9). Here Eq. (3.3.8) and Eq. (3.3.9) are used to calculate the statistical significance of the DC excess in standard deviations. For the phase calculation I made the time epoch correction for the background windows as defined in Eq. (3.3.11), and will use the maximum-likelihood ratios to calculate my statistical significance for any phase bin excess in standard deviations. I plot the four phase histograms for the on-source window, as well as for the 35 off source windows. The on-source window should display a peak near 0.65, and the off-source windows should display a flat distribution if events from Cygnus X-3 are detected in the on-source window. In addition I added histograms that plot the right ascension verses the number of events in various phase bins. The phase bins between 0.65 and 0.90 should show a larger excess in the on-source region, than right ascension histograms including all phases, if events in the source region are from the direction of Cygnus X-3.

Chapter 4
Muon Observations

The reported muon signals coming from the direction of Cygnus X-3 have been the subject of great debate and controversy over the last few years. Four underground detectors and one above-ground detector show some evidence of muon tracks from the direction of Cygnus X-3, while three other underground experiments could find no signal (see Table 4.1). Of these only two of the underground experiments show substantial results. The Soudan-1 and NUSEX tracking detectors both showed very positive results. The Soudan-1 detector showed a $\approx 3\sigma$ enhancement on the phase plot between 0.65 and 0.90, and the NUSEX detector showed a substantial peak in the phase plot between 0.70 and 0.80. There were three other experiments that showed only marginal evidence of a muon signal from Cygnus X-3. The underground IMB water Cerenkov detector and the Mayflower scintillation detector recorded only 1.8σ and 2.3σ enhancements in the 0.65 and 0.90 range on the phase plots respectively. Also, the ground level MUTRON magnetic spectrometer showed only a 2σ enhancement near 0.60 on the phase plot. There are also three experiments that claim to see no muon signal from the direction of Cygnus X-3. No excess muon signal or phase enhancement were found with the Fréjus tracking detector, the Kamioka water Cerenkov detector, or the Baksan liquid scintillation detector. The variability of the reported results from these detectors has created a lot of controversy concerning the reported positive

results, and has led many physicists to believe that we may not completely understand all of the mechanisms involved.

Table 4.1: Detectors that attempted to point muon tracks back to Cygnus X-3.

Detector	*Size* (m^3)	*Latitude*	*Depth* (m)	*Signal*
$Soudan - 1$	$(2.9 \times 2.9) \times 1.9$	$48°$	$600m$	3.5σ
$NUSEX$	$(3.5 \times 3.5) \times 3.5$	$45.9°$	$1,850m$	$> 4.0\sigma$
IMB	$(18 \times 19) \times 24$	$41.7°$	$1,570m$	1.8σ
$Mayflower$	$(37m^2) \times ?$	$40.5°$	$200m$	2.3σ
$MUTRON$	$(16 \times 7) \times 4$	$34.0°$	$Sea\ Level$	2.0σ
$Fréjus$	$(6 \times 6) \times 12.3$	$45.1°$	$1,800m$	0σ
$Kamioka$	$(60.8 \times \pi) \times 16$	$36.4°$	$1,000m$	0σ
$Baksan$	$(16 \times 16) \times 11$	$44.3°$	$300m$	0σ

4.1. Positive Sightings

4.1.1. Soudan-1

One positive sighting of Cygnus X-3 came from the Soudan-1 detector in Minnesota, USA. The Soudan-1 detector is a test calorimeter for the second generation Soudan-2 detector, and is composed of 3456 proportional tubes. It is located at a latitude of $48°$ north, has dimensions of $(2.9 \times 2.9) \times 1.9m^3$, and is at a depth of 600m (1800m of water equivalent). The detector has a $1.4°$ angular resolution, and a 45% running efficiency. Muon events are required to

have at least eight proportional tube hits in each of two orthogonal views. A 0.96 year live time sample collected from September 1981 to November 1983 resulted in 784,000 recorded muon events. 1,183 of these events came from within 3° of Cygnus X-3.[1]

In May 1985, an article was published that claimed that Cygnus X-3 had been identified in terms of both direction and phase; however, this claim was not completely straightforward.[10] A 6° diameter window centered on Cygnus X-3 did not show a significant excess of events from Cygnus X-3. In addition, a phase analysis preformed by folding the data with the van der Klis and Bonnet-Bidaud ephemeris, which is used by all of the underground experiments, showed no significant modulation. However, when the 6° diameter window was offset by 2.7° north (larger than the 1.4° angular resolution), the results were strikingly different.[1] A major 3σ phase enhancement of 84 ± 20 events above the background in the range of 0.65 to 0.90 occured, as seen in the phase plot in Figure 4.1.1.[10]

A second article published in November 1985[17] reanalyses the data sample covered in the first article. The background was determined from off-source directions in the same declination band and Rayleigh analysis was performed. This time the 6° window was centered on Cygnus X-3, and showed 60 ± 17 events in the peak phases 0.65 and 0.90 as shown in Fig. 4.1.2. This is a 3.5σ effect with a $\sim 2 \times 10^{-4}$ probability of being from background fluctuation.[17]

The second paper also found two different enhancements of the phase plot results. The first of these involved analysing pairs of events that occur within
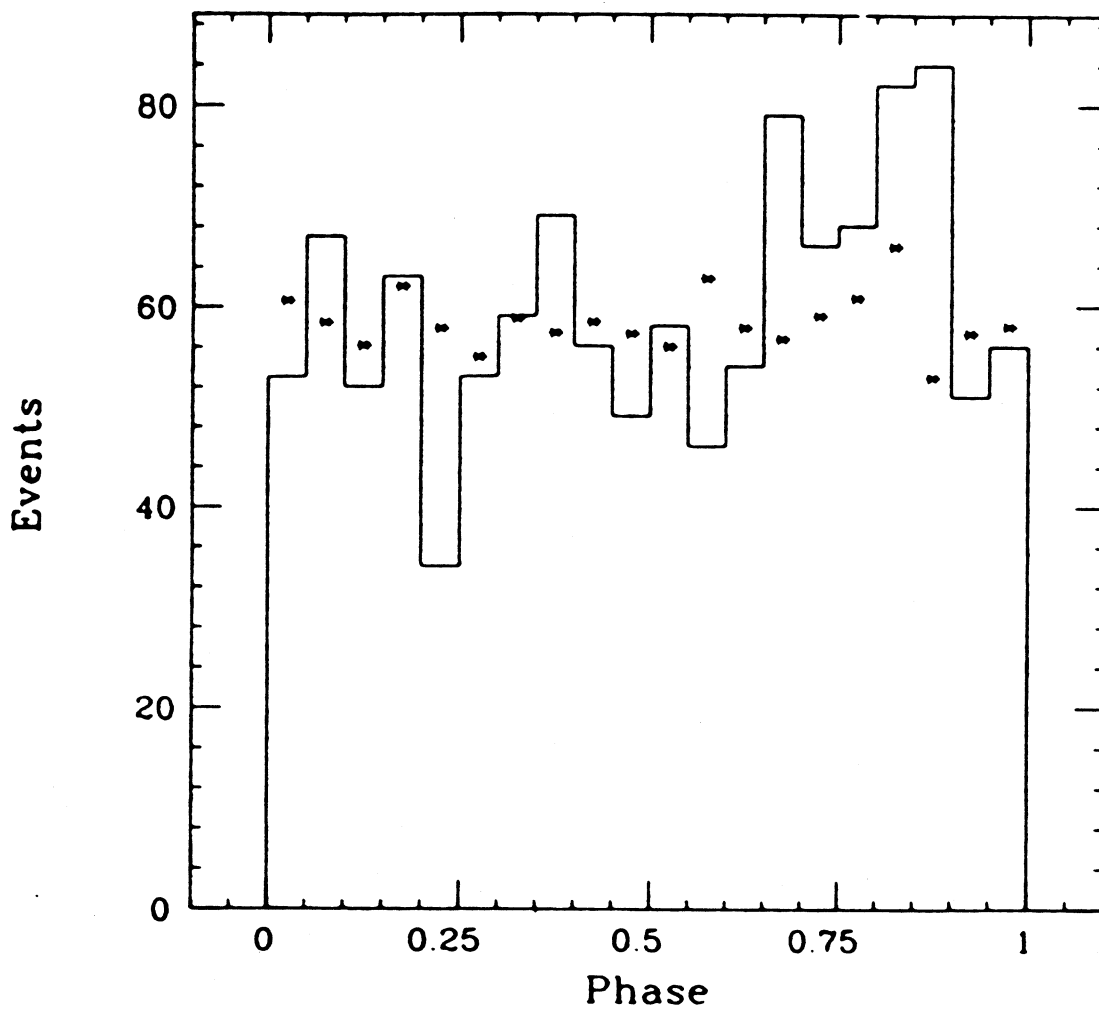
Figure 4.1.1: Phase plot from the Soudan-1 detector for events within 3° of the position 2.7° north of Cygnus X-3 show a 3σ enhancement from 0.65 to 0.90. The points represent the expected number of background events.[10]
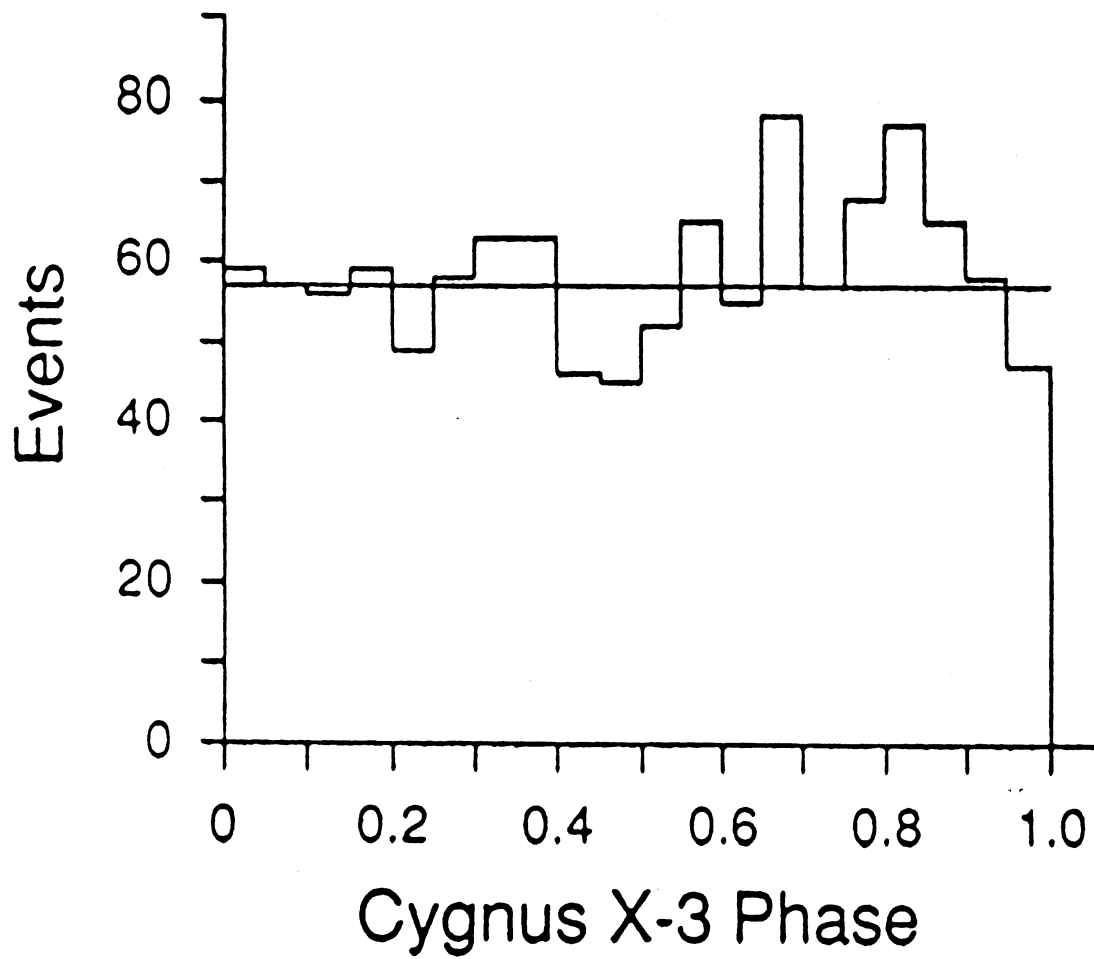
Figure 4.1.2: Phase plot from Soudan-1 for muons within 3° of Cygnus X-3. The horizontal line represents the expected number of background events.[17]

0.5 hour of each other. For the phases between 0.65 and 0.90, 29 ± 6 pairs were found above background of ≈ 8, which corresponds to a $\sim 3 \times 10^{-4}$ probability of the events being from random fluctuation. The second enhancement found involved analysis of data collected during the September – October 1985 large radio outburst. Here the phase bins were reduced from 0.05 to 0.025. No directional excess was noted; however, on the phase plot there were 10 events over the background of ≈ 3 in the 0.725 to 0.750 phase interval.

4.1.2. NUSEX

The strongest evidence for a muon signal coming from Cygnus X-3 comes from the NUSEX detector installed in the Mont Blanc tunnel in Italy. The NUSEX detector is a digital tracking calorimeter with 134 horizontal iron plates (3.5×3.5) m^2 and $1cm$ thick with $50,000$ $1cm \times 1cm$ streamer tubes interleaved with the iron planes.[19] It is located at a latitude of $45.9°$ north, is $(3.5 \times 3.5 \times 3.5)$ m^3, and is at a depth of $1850m$. The detector has a $\approx 1.2°$ angular resolution, and an 86% running efficiency. Four contiguous planes or one pair and three other contiguous planes must be fired simultaneously to meet the trigger requirements for the muon track.[20]. An effective running time of 2.4 years from January 1, 1982 to February 1, 1985 resulted in the collection of $21,700$ muons with zenith angles up to $85°$. Cygnus X-3 was observed for about 76% of the time, and a total of 142 events were recorded in a $9°$ diameter window centered on Cygnus X-3.[1]

Piazzoli reported that underground muons from the direction of Cygnus X-3 were observed at the NUSEX experiment.[19] The background was determined

from comparison of the 9° diameter window centered on Cygnus X-3 with 27 other 9° diameter windows centered off-source on the same declination band every 4.5°. A marginal excess of 28 events over a background of 114 was recorded. A phase analysis showed more substantial results. An excess of 19 events against an average off-source background of 11.39 ± 0.23 events is found in the phase between 0.7 and 0.8, as is shown in Figure 4.1.3. The probability of this occuring from random background fluctuations was calculated to be less than $\sim 10^{-4}$. Results published by Battistoni covering the same data set yielded almost identical results.[20] In this article, a $10° \times 10°$ window centered around Cygnus X-3 was used. A graph almost identical to Figure 4.1.3 was produced. 32 events occured in the phase range 0.7 to 0.8, and the average off source background was 13.0 ± 0.2. Again the probability of this excess being due to background was calculated to be less than $\sim 10^{-4}$.

In the Piazzoli article, the phase interval of 0.6 to 0.7 was then plotted against the right ascension angle on one graph for the windows used to determine the background, and the window pointing to Cygnus X-3. This yielded ≈ 28 events over the background of 113.2 ± 2.1, with a probability of this being due to random fluctuations less than $\approx 10^{-3}$.
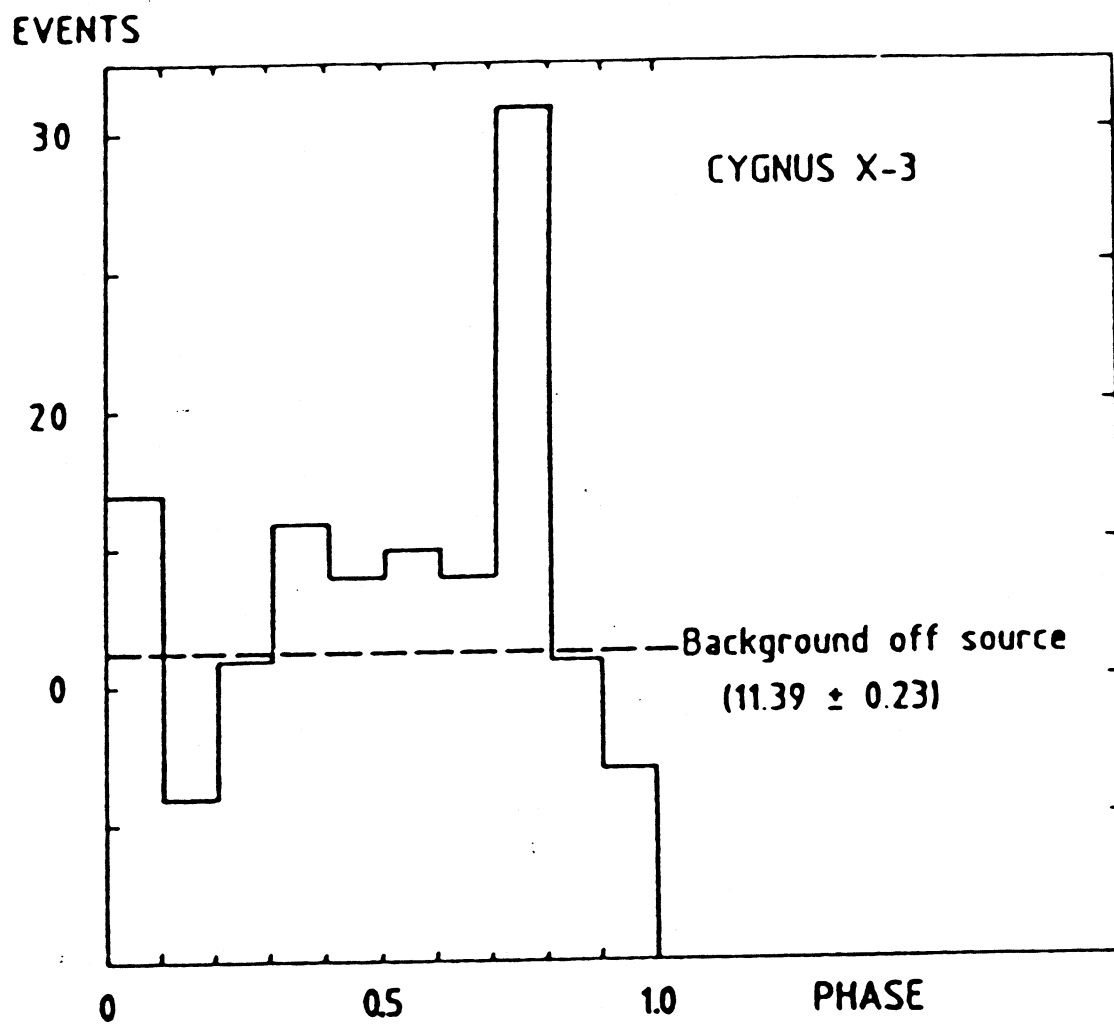
Figure 4.1.3: Phase plot from the NUSEX experiment of muon tracks within 4.5° of Cygnus X-3.[19]

4.2. Possible Sightings

4.2.1. IMB

The Irvine-Michigan-Brookhaven (IMB) proton decay detector located in Fairport Harbor, Ohio showed evidence of a possible sighting of Cygnus X-3. The IMB detector is a a water Cerenkov detector with 2048 five inch photomultipliers that provide timing and pulse height information. It is located at a latitude of $41.7°$, has dimensions $(18 \times 19) \times 24m^3$, and is at a depth of $600m$ ($1570m$ of water equivalent).[1] The detector has a $7°$ angular resolution, and an $\approx 10\%$ running efficiency. Trigger cuts were made based on the number of photomultiplier tubes hit. The events that were left were mostly single muons of energy greater than 2 GeV. A 655-hour live time sample collected from September 1982 to April 1984 resulted in $36,046$ uncut muon events within $7°$ of Cygnus X-3.[21]

A July 1987 article summarized the results of the IMB search for Cygnus X-3.[21] A $7°$ half angle window centered on Cygnus X-3 shows only a 1.8σ excess in the range of 0.65 to 0.90 on the phase plot. There were 8749 observed events compared to 8704 expected events in this phase range.[21] This is a much less significant signal than was seen by the Soudan-1 and NUSEX experiments. Bonnet suggests that this could be due to the poor angular resolution of the detector and the fact that the time coverage was sparse. [1]

The IMB group then analysed events gathered from the times of large radio outbursts,[21] since the Soudan-1 papers suggested a link between the

phase plots and the time of the outbursts.[17] There were three periods of times corresponding to large Cygnus X-3 radio outbursts studied. Data gathered from both the September/October 1982 (55 hours of uncut data), and the February/March 1983 (36 hours of uncut data) radio outbursts reveiled no significant excesses. However, when the data from the September/October 1983 (71 hours of uncut data) outburst were analysed, strikingly different results were obtained. Figure 4.2.1 is a phase plot of these data. It shows a 4.2σ excess in the phase interval between 0.5 and 0.65.

4.2.2. Mayflower

Another possible sighting of Cygnus X-3 occured at the Mayflower detector located in the Mayflower mine near Herber, Utah.[22] The Mayflower detector is composed of 300 plastic scintillation counters arranged in three layers, and was designed to measure sidereal anisotropy in the cosmic ray muon flux. It is located at a latitude of $40.5°$ north, has an area of $37m^2$, and is at a depth of $200m$ (500 hg cm^{-2}).[1] The detector has a resolution of only $15°$ in α, and a running efficiency of 65%. A 5.4 year live time sample from January 5, 1978 to August 1983 resulted in 0.49×10^9 recorded events. The events were tallied in $60,419$ non-empty half hour summaries, with an average of $7,810$ events per summary.[22]

Background was determined with windows pointing at different right ascensions, and it was found that the signal was slightly greater when pointed toward Cygnus X-3. A right ascension window $15°$ wide centered on Cygnus
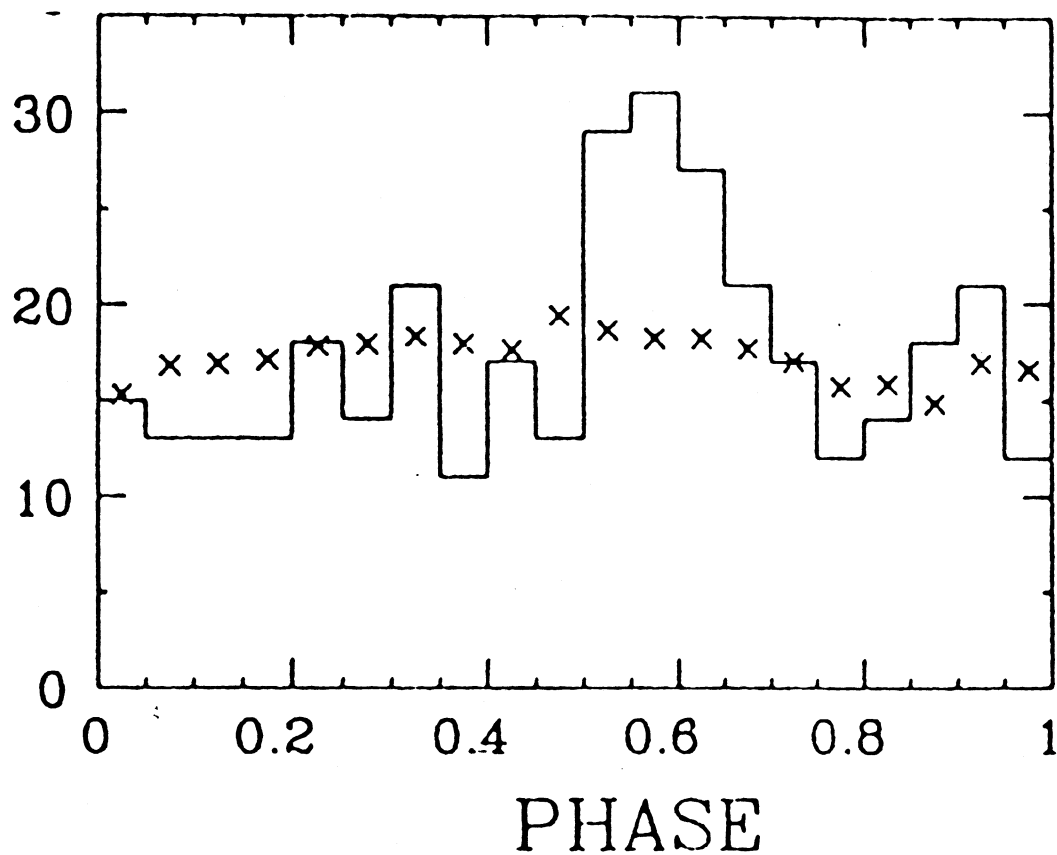
Figure 4.2.1: Phase plot from the IMB detector for data taken
during a large radio outburst from Cygnus X-3. The data was
a $\frac{690}{64}$ hour live time sample from September 17 to October
31, 1983. The crosses represent the expected background
distribution in absence of a source.[21]

X-3 was used to create the phase plot, and a least squares fit to a sine wave was applied to the data. The amplitude of the sine wave was found to be $\left(1.7 \pm {}^{0.8}_{0.5}\right) \times 10^{-4}$, and occured at a phase of 0.67 ± 0.10. This is a marginal 2.3σ effect, and is shown in Fig. 4.2.2. Attempts were made to enhance this effect using windowing, but yielded no significant results.[22]

4.2.3. MUTRON

A third experiment that yielded borderline results is the MUTRON detector in Japan. The MUTRON detector is a magnetic spectrometer with wire and spark chambers. It is located at a latitude of $\approx 34°$ north, and has dimensions of $(16 \times 7) \times 4m^3$. Unlike most of the detectors covered in this section that are located underground, the MUTRON detector is located at ground level. The detector has an angular resolution of $\approx 5°$ right ascension and $\approx 1°$ declination. Data was gathered from March 1977 to July 1982, and a $4°$ right ascension window centered on Cygnus X-3 was used to create a phase plot. The results showed a broad modulation around ≈ 0.6 with a marginal 2σ enhancement.[1]
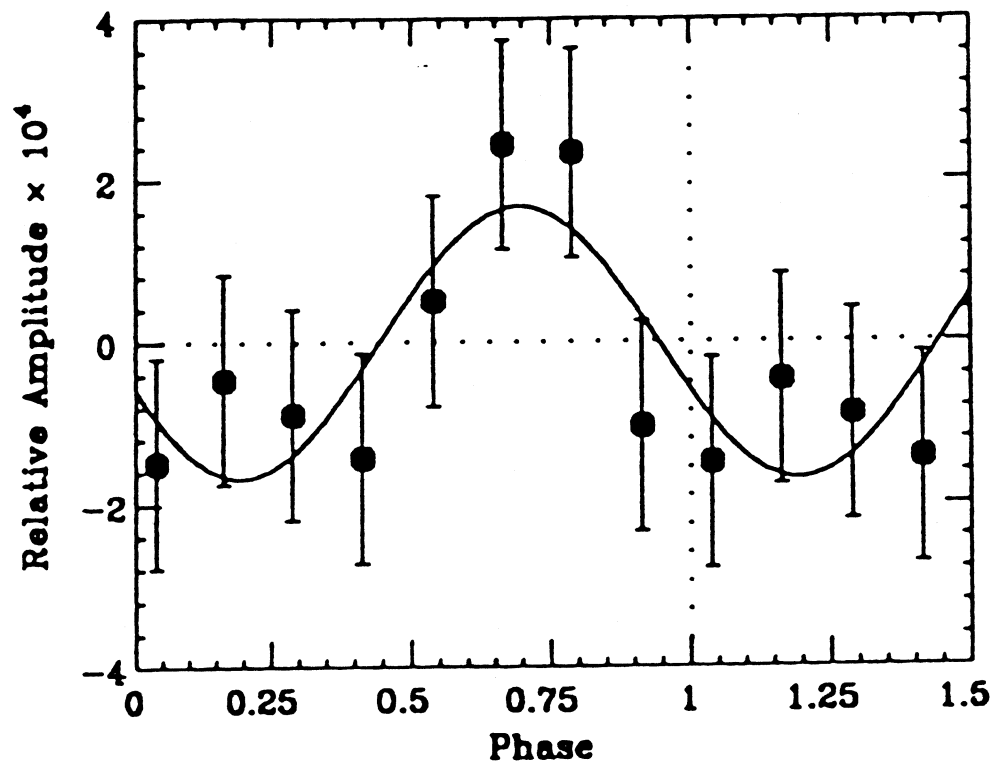
Figure 4.2.2: A phase plot from the Mayflower experiment of data coming from a 15° right ascension window. 1.5 periods of the phase plot are shown for clarity.[22]

4.3. Negative Sightings

4.3.1. Fréjus

One detector that did not show any evidence of Cygnus X-3 was the Fréjus nucleon decay detector located near Modane, France. Fréjus is a fine grain tracking calorimeter that measures $(6 \times 6) \times 12.3 m^3$ and weighs 900 tons. It is located at a latitude of $45.1°$ north, and is at a depth of $1800m$. Fréjus has $1,000$ vertical planes of flash chambers and Geiger tubes with alternating horizontal and vertical cells. The $40,000$ Geiger tubes trigger the $\approx 930,000$ flash chamber cells, and allow muon tracks to be recorded at ≈ 20 per hour. The detector has an angular resolution of $\approx 1.2°$, and a running efficiency of 78%.[23] Trigger cuts include muon tracks almost parallel to the vertical detector planes, and tracks that do not cross eight flash chamber planes in each view. Data were collected from February 1984 to January 1986, and resulted in $170,146$ single muon events.[23]

Berger reported that no excess in events were recorded with a $10°$ window centered on Cygnus X-3.[23] A $2°$ half angle window window centered on Cygnus X-3 showed 70 muon events, compared to the expected number of 65.3, and $5°$ half angle window window centered on Cygnus X-3 showed 419 muon events, compared to the expected number of 414.5. Neither of these plots show significant excess. The background rate was calculated with 35 off-source windows spaced every $10°$ right ascension on the same declination band. Phase plots were created using the $2°$ and $5°$ half angle windows centered on Cygnus

X-3. A weighting system was used to account for the time that the detector was inactive. The phase plot was incremented with a weight proportional to the corresponding daily background muon flux. These plots are shown in Figure 4.3.1 and reveal no phase peaks on either plot in the range of 0.65 to 0.90.[23]

Berger then looked to see if there was a correlation between the large radio outbursts and muon tracks coming from Cygnus X-3 as was suggested in the Soudan-1 experiment.[17] The muon tracks collected from the September/October 1985 radio outburst were analysed. No accumulation was noticed around Cygnus X-3. In a 5° half angle window centered on Cygnus X-3, only 24 muon events were recorded, compared to the 21.8 events expected. In addition, no peak was found in the phase range 0.65 to 0.90.

The results from this experiment are significant because the Fréjus detector is the same type of detector as the NUSEX detector, which showed the most substantial phase peak. The two detectors are at similar depths and geographic locations. In addition, the Fréjus detector is six times larger than the NUSEX detector, and collected five times as many muon events. Bonnet offers the explanation that the time overlap of the two experiments was not complete, and the signal coming from Cygnus X-3 could show variability.[1]

4.3.2. Kamioka

Another detector that did not show any evidence of Cygnus X-3 was the Kamioka nucleon-decay experiment located in the Kamioka mine in Japan. The
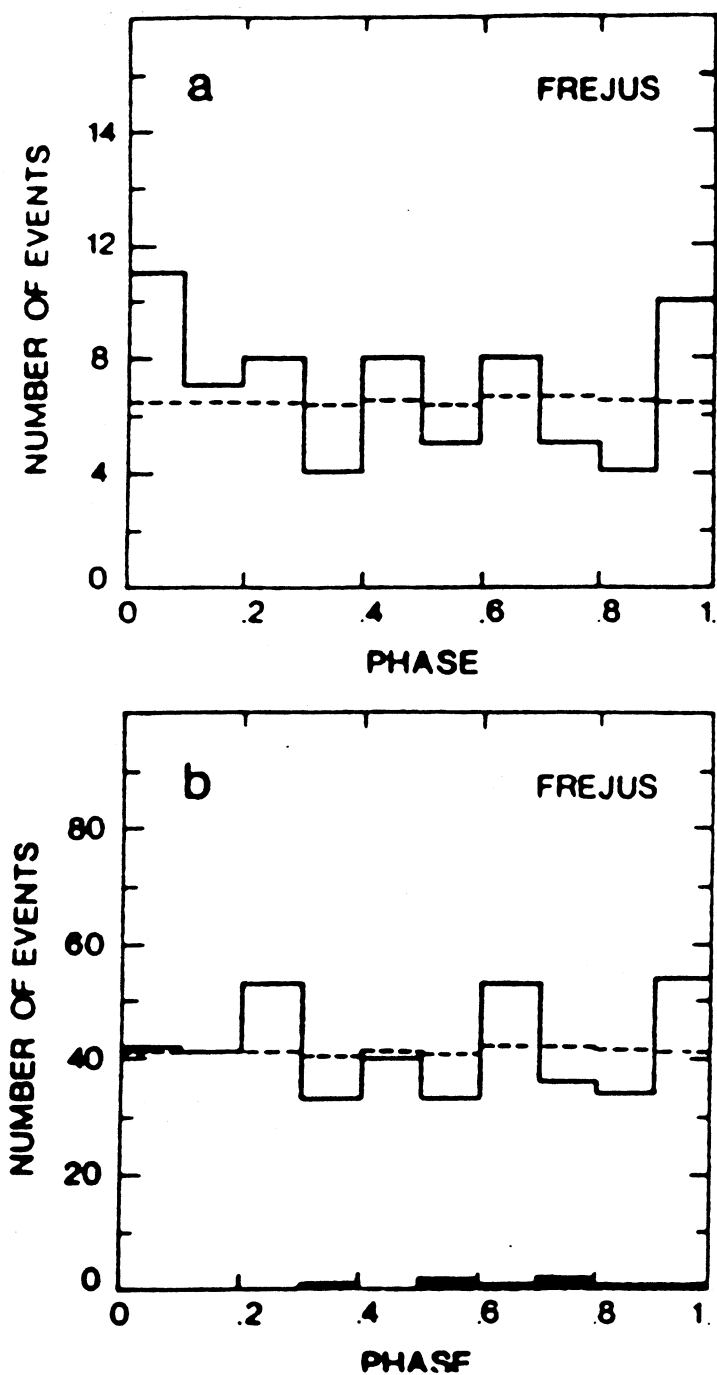
Figure 4.3.1: Phase plots from the Fréjus experiment with 2° and 5° half angle windows. No peaks are seen in the 0.65 to 0.90 phase range. The dashed line represents the expected number of background events.[23]

Kamioka detector is a water cerenkov detector that is composed of a cylindrical steel tank with diameter of $15.6m$ and and a height of $16m$ that stores $3,000$ tons of pure water. This is 30 times larger than the Soudan-1 detector.[1] 100 photomultipliers, each with a 20-inch diameter photosensitive area, cover 20% of the inner surface of the tank. It is located at a latitude of $36.4°$ north, and is at a depth of $1,000m$. The detector has a $2.7°$ angular resolution, and a 40% running efficiency. All events with a total phase height of 110 photoelectrons are recorded in normal trigger mode. Data were taken continuously for a 204-day period from July 1983 to September 1984, and resulted in 1.9×10^6 events. 5560 muon tracks were recorded from a $10° \times 10°$ window centered on Cygnus X-3.[24]

Oyama reported that no excess flux was found in the direction of Cygnus X-3, or in the phase plot from 0.7 to 0.8. The background was determined with 16 non-overlapping off source regions in the same declination band spaced every $10°$. Corrections were made for the dead times that the detector was not running, and the results showed nothing of significance. There were 4874 ± 69 muon tracks in the on-source window, and an average of 4924 ± 18 muon tracks in the off-source windows. Figure 4.3.2 shows the phase plot distributions with ratios of on-source to off-source tracks for each phase bin. No peak is found in the 0.65 to 0.90 phase range.[24]
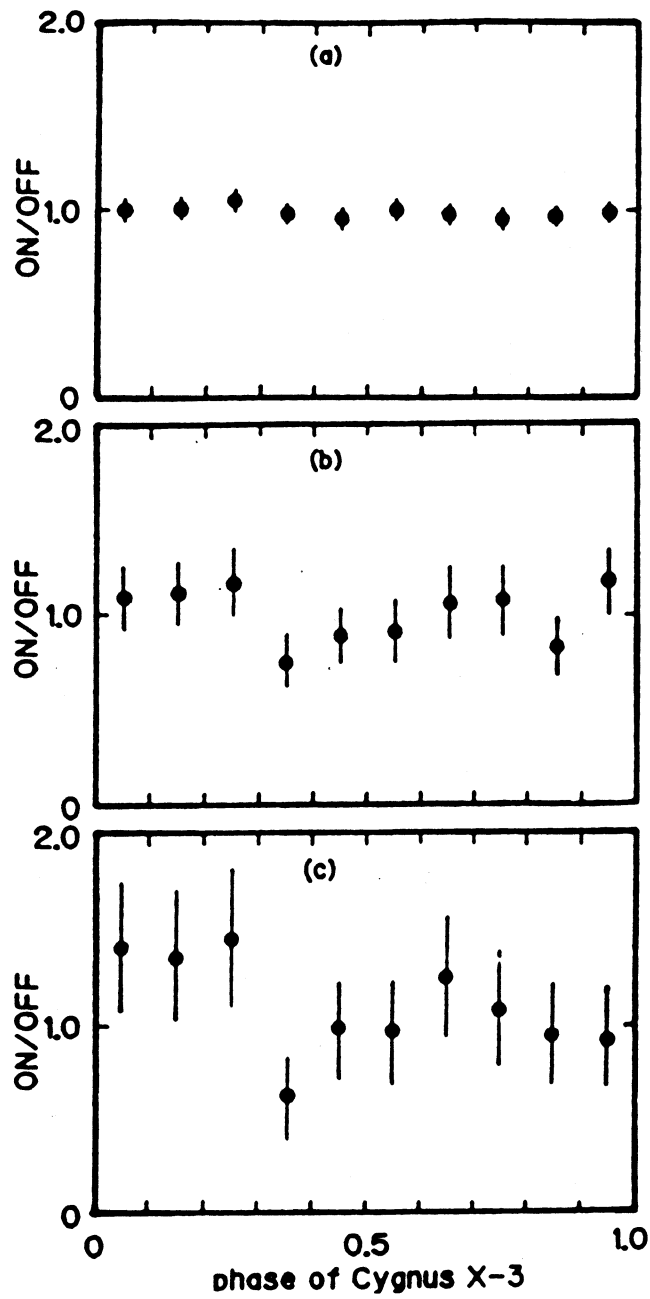
Figure 4.3.2: Phase plots from the Kamioka experiment for muons tracks coming from Cygnus X-3. The ratio of on-source to off-source events for each phase bin is shown at three different depths: (a) 2400 mwe, (b) 3400 mwe, and (c) 4400 mwe.[24]

4.3.3. Baksan

Another detector that failed to point muon tracks back to Cygnus X-3 was the Baksan detector in USSR. The Baksan detector is composed of liquid scintillator and wire cambers, and was built for studying atmospheric neutrinos and supernova neutrino bursts. It is located at a latitude of 44.3° north, and is at a depth of $300m$. It has dimensions of $(16 \times 16) \times 11m^3$, which makes it ≈ 30 times larger than Soudan-1. The detector has a 2° angular resolution, and an 80% running efficiency. Muon events were collected from March 1982 until February 1986 at a rate of $\approx 10^8$ muons per year. A $10° \times 10°$ window centered on Cygnus X-3 was constructed. There was no excess of events coming from the direction of Cygnus X-3. In addition phase plots were constructed and showed no peak in the 0.65 to 0.90 phase range. This is significant since this detector is the same type as Soudan-1, which recorded a positive sighting of Cygnus X-3. Both detectors cover similar time frames, and the Baksan detector is much larger than the Soudan-1 detector, allowing it to collect many more muon events.[1]

4.4. Observation Conclusions

The results of all of the experiments looking for muons from the direction of Cygnus X-3 are very variable. The Soudan-1 and NUSEX experiments announced substantial positive sightings. These sightings were controversial, since they would imply a production of muons by non-standard methods from known particles, or production by a new neutral particle. Other sightings

of Cygnus X-3 were not as positive. The IMB, Mayflower, and MUTRON detectors showed only marginal evidence of a signal; however, this marginal evidence occured in the same 0.60 to 0.90 range of the phase plots for all of these experiments. This is the same phase plot range that the Soudan-1 and NUSEX experiments showed enhancements. The Fréjus, Kamioka, and Baksan detectors showed no evidence of a signal. The negative sightings are very important, since they are larger detectors that have collected more data than the Soudan-1 and NUSEX experiments. For example, the Fréjus detector is very similar to the NUSEX detector in type, location, and depth. It has recorded five times as many events as NUSEX, but does not have a complete time overlap. Similarly, the Baksan detector is similar to the Soudan-1 detector, and is $\approx$ 30 times larger in size. These two detectors have data taken over similar time frames. It is not understood why these results vary so greatly. I feel the results of these experiments are summarized best in Piazzoli's claim that "More and better observations [of Cygnus X-3] are urgently needed. An important lesson we have learnt is that experiments performed in different locations and depths or at different times are difficult to compare."[19] With this in mind, the D0muon Basement detector was used in this experiment to look for muon signals coming from the direction of Cygnus X-3. This includes the same phase plot analysis that was used in all of the above experiments.

Chapter 5
The D0 Muon Cosmic Ray Telescope

The D0muon Cosmic Ray telescope is a collaboration of Northern Illinois
University, Fermi National Accelerator Laboratory, and the University of
Minnesota. The telescope consists of drift chambers, a trigger system,
electronics, a data acquisition system, and data analysis software that are
nearly identical to the system of the D0 experiment (E-740) at Fermi National
Accelerator Laboratory. In fact, it has been used as a test bed for the
D0 experiment, where prototype electronics and chambers were tested and
debugged. The electronics have been completely updated to the final version
that will be run in the D0 experiment, and the cosmic ray telescope should
provide valuable information on the muon fluxes from Cygnus X-3.[25]

The muon fluxes from Cygnus X-3 and some other X-ray sources have
proven difficult to explain. Previous observations have come from experiments
deep underground as described earlier. Most of these experiments had very low
event rates and allowed no momentum analysis for the muons. As an example
of the low event rates, the underground Soudan-1 experiment produced only 90
events from the direction of Cygnus in a period of six months.[25] The cosmic ray
telescope, on the other hand, has an 1.4 kilogauss iron electromagnet that allows
the momentum of the tracks to be analysed. In addition, it is estimated that for
6 months of running for only 50% of the time would result in 100 *million* events

on tape, with 3000 muons with momentum above $100GeV/c$. Based on analysis of data from a previous run, and assuming 100 *million* events are collected on tape, we would have $\approx 73,000$ events from the direction of Cygnus X-3. This could provide valuable analysis of the muon fluxes coming from Cygnus X-3.[25]

5.1. The Detector

The cosmic ray detector consists of four chambers, a Fe electromagnet, and two layers of scintillators. The chambers each measure $2.4m$ x $6m$, and provide an accurate 3-D position of the particle. The four chambers do this with an array of sense wires and vernier pads that pinpoint the track to $\pm 0.31mm$ in the horizontal position perpendicular to the wire direction, and to $\pm 2.7mm$ with a vernier pad fit or to only $\pm 20cm$ without the pad fit in the wire direction.[27] This corresponds to an angular resolution of $\approx 1°$ in the direction perpendicular to the wires, and $\approx 1.4°$ with the pad fit or $\approx 10°$ without the pad fit in the wire direction. The magnet is sandwiched between the top two and bottom two chambers, and allows momentum analysis to be done on the muon tracks. The trigger is provided by the two layers of scintillator. A coincidence between the two layers of scintillator set up the timing signals that synchronize the electronics. Figure 5.1.1 shows a side view of the detector.

3.7m

3.0m

2.3m

2.05m

1.05m

0.8m

0.5m

0.0m

Module 200

Top Scintillators

Module 100

Magnets

Module 11

Bottom Scintillators

Module 10

~6m

~2½m

y

z

x

N

E

W

S

Coordinate system with the
origin just below the bottom
of Module 10, near the center
of the chamber.
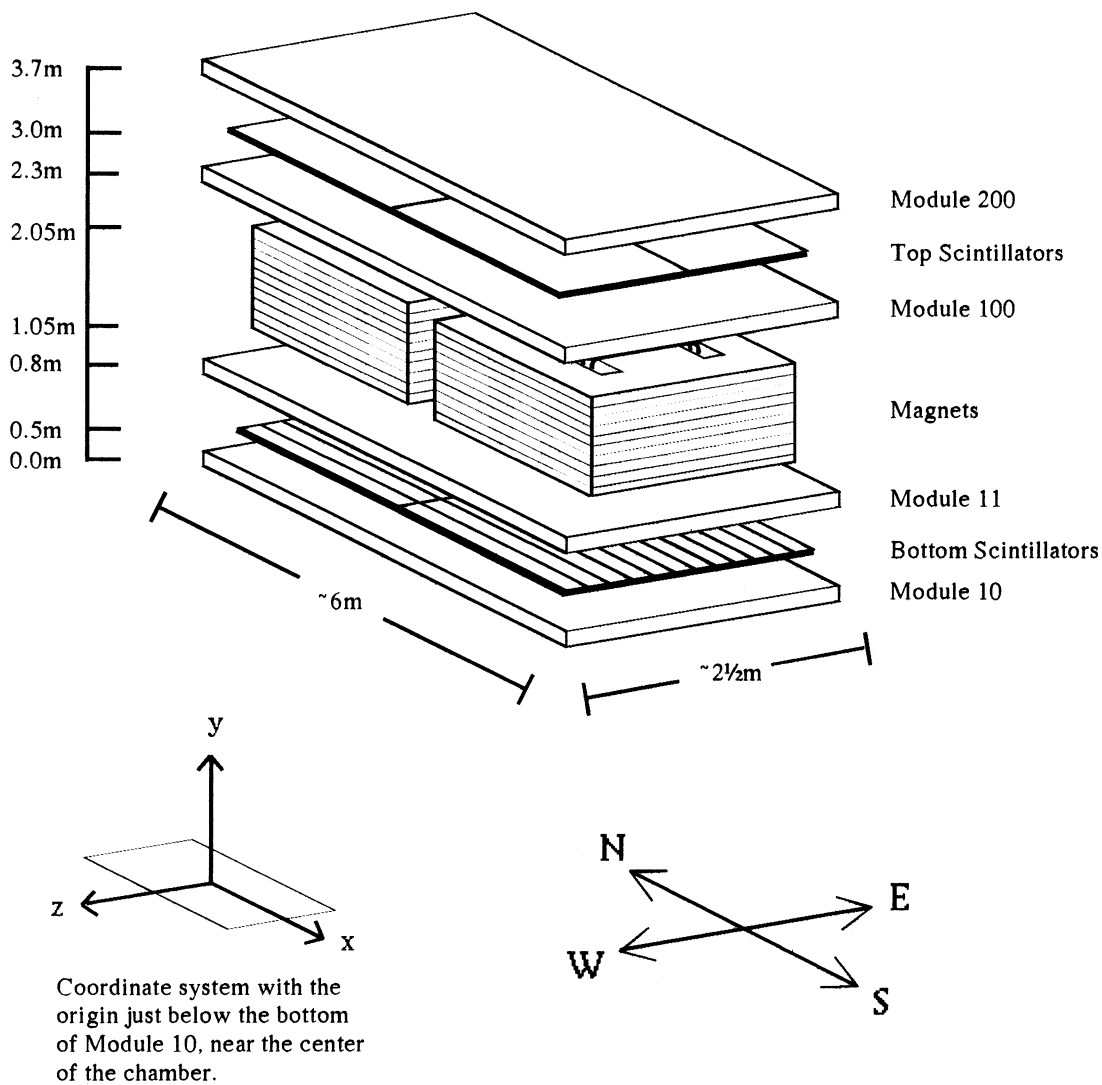
Figure 5.1.1: Side view of the cosmic ray telescope that consists of four wire chambers, two magnets, and two layers of scintillator. This diagram is borrowed from Figure 3.1 of Mueller.[26]

5.1.1. Chambers

There are four chambers in the D0 Muon Basement Detector. Each chamber is composed of 72 unit cells that are $10.1cm$ x $5.5cm$ x $6m$. The unit cells are arranged in three layers, so that each layer contains contains 24 unit cells. Each unit cell contains an anode sense wire running through the center of the cell for the full length of the chamber. The sense wires are used to locate the position of the particles going through the chamber both in the direction of the wire and in the horizontal direction perpendicular to the wire. The layers of the cells are slightly offset to compensate for left/right ambiguity in the position of the track. Each unit cell also contains two cathode vernier pads. The pads are located on the top and bottom of the unit cell, and help get a fine tuned position of the track in the wire direction.[29] The unit cells are connected with special sealed Aluminum extrusions and Ar/CO_2 gas is used which optimizes the detection of the muons.

Each anode sense wire is a gold-plated $50\mu m$ tungsten wire that is run at $+4.54$ KV.[28] When a charged muon goes through the chamber, it causes the gas in the cell to ionize. The electron is attracted to the anode sense wire, which ionizes more particles, and this repeats so that an avalanche of electrons occurs. When the avalanche of electrons hits the wire a signal is produced. Scintillator is located near to the chamber, so that the exact time that the track went through the chamber is known. Comparing this time to the time that the sense wire receives a signal, and knowing how fast the electrons drift through the gas, gives a horizontal position perpendicular to the wire. The wires run parallel to

the field created by the magnet so that the bend of the track occurs in the drift direction. Resolutions of $\pm 0.31 mm$ are obtained in this coordinate.[27]

The angular resolution can then be calculated from the positional resolution using Eq. (5.1.1) below,

$$\sigma_\theta = \sqrt{\left(\frac{\partial\theta}{\partial x_1}\right)^2 \sigma_{x_1}^2 + \left(\frac{\partial\theta}{\partial x_2}\right)^2 \sigma_{x_2}^2} \qquad (5.1.1)$$

which yields an angular resolution of $\approx 1°$.

Each wire is connected at one end to an adjacent wire in the same row so that the wires form wire pairs. This is done so that electronics servicing both ends of the wire are on the same side of the chamber. Connecting electronics to both ends of the wire allow a coarse measurement of position in the wire direction. This is done by comparing the time that the signal reaches one end of the wire to the time that it reaches the other end of the wire.

For example, in Fig. 5.1.2, if l is the length of the chamber, and x is the position of the track, $t_a = \frac{x}{c}$ is the time the signal arrives at one end, and $t_b = \frac{(2l-x)}{c}$ is the time that the signal arrives at the other end. Then the difference between these two becomes,

$$\Delta t = t_b - t_a = \frac{2(l-x)}{c} \qquad (5.1.2)$$

And the resolution is,

$$d(\Delta t) = \sqrt{2}dt_a = \frac{2dx}{c} \qquad (5.1.3)$$

Here the resolution in the wire direction is only $\pm 20 cm$.[27] Using Eq. (5.1.1), the anglar resolution in the wire direction is then $\approx 10°$.
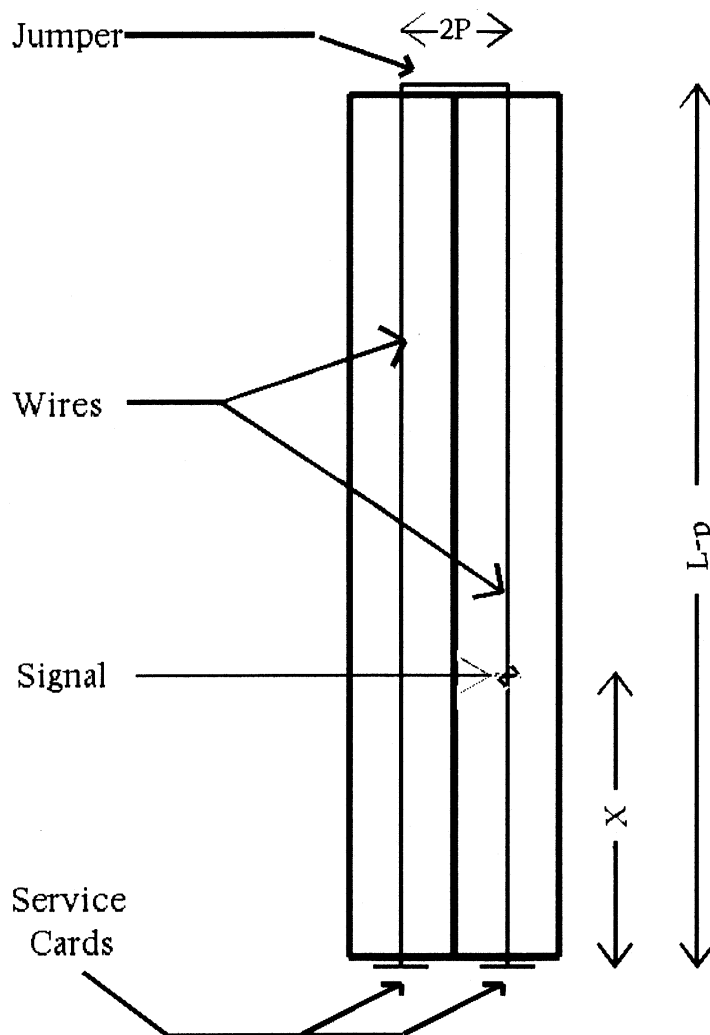
Figure 5.1.2: A top view of a wire pair on a muon chamber. The hit occurs at a distance X from one end of the chamber, the total length of the wire is $2L$, and P is a correction for the length of the jumper that connects the two wires. The difference in the arrival times of the signal at the two service cards can be used to determine the position of the track along the wire (non-bend) view.

Vernier pads were introduced to increase the resolution in the wire direction. These cathode pads run at +2.60 KV, and are made of copper clad Glassteel. The Glassteel is polyester and epoxy based plastic sheets with a glass fiber mat.[28] Sawtooth patterns were cut into the copper coating to make an isolated right and left side of conductor on the pad (see Fig. 5.1.3).
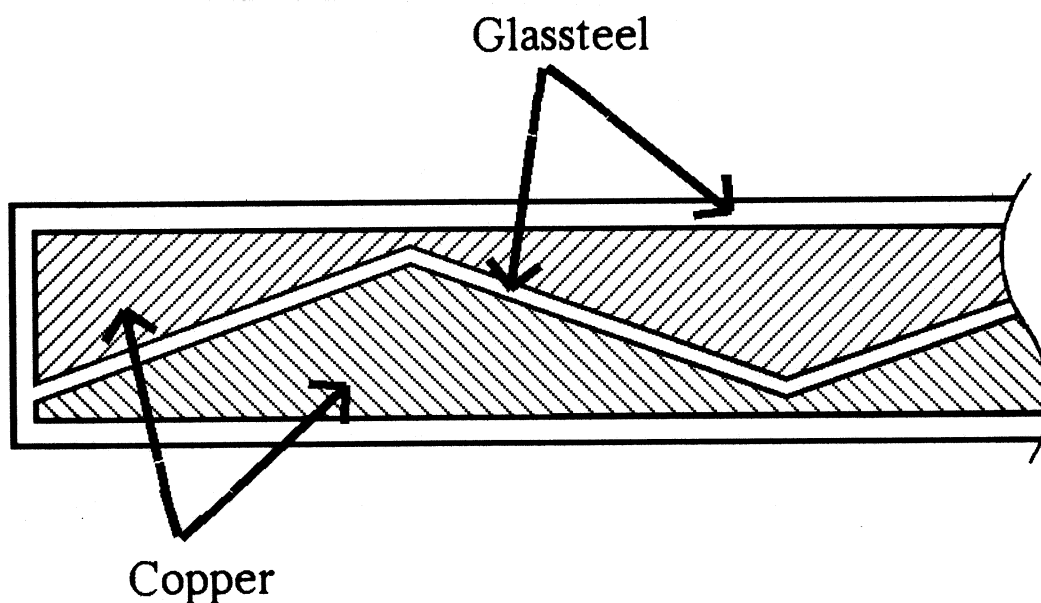
Figure 5.1.3: The Pad Configuration used in the D0muon basement detector chambers. A sawtooth pattern is cut in the copper foil that is bonded to the insulating Glassteel, and is used to increase the resolution in the wire direction.

Each cell contains a top and bottom pad, and the left sides of both pads are wired together, as well as the right sides. Comparing the ratio of charges on each side of the pad will give a more precise position in the non-bend direction. The length of one period of the sawtooth pattern is larger than the resolution in the non-bend view without the pad. So a coarse position in the wire direction is found by comparing the times of arrival of the signals on both ends of the wire, and a fine position is then determined by comparing the charges on both sides of the pads. The pad patterns are shifted by $10cm$ between layers to reduce the ambiguity coming from node points.[28] Using this method, the resolution in the wire direction becomes $\pm 2.7mm$,[27] and using Eq. (5.1.1) the angular resolution becomes $\approx 1.4°$.

The pads are held in position by Aluminum extrusions that fit together to form the structure of the whole chamber. The chamber is sealed and 90% $Ar/10\%CO_2$ gas is run through the chamber. The gas content is very important to the proper functioning of the chamber. For example, Oshima and Igarashi found that a 1% change in the CO_2 content makes a $17 \pm 5\%$ gain change, and at an oxygen content of $3200ppm$ there is a 35% drop in the gas gain.[27] It is important, therefore, to monitor the contamination of the gas in the system. Presently the gas system on the basement detector is run off of four gas bottles, has a recirculating pump to use the gas more efficiently, and has an oxygen meter to monitor the oxygen contamination in the system.

5.1.2. Magnet

The magnet for the basement comes in two sections, which are the north half and the south half. Each half covers an $2\frac{1}{2}m$ x $2\frac{1}{2}m$ area on the chambers, and stands approximately $1m$ high. The magnet has a field strength of 1.4 $Kgauss$, which allows measurements of momentum from 5 GeV/c to 500 GeV/c. Muons going through the magnet get a 450 MeV/c momentum kick in the drift direction. Momentum resolution depends on this as well as the resolution in the drift direction and multiple scattering due to the $1m$ Fe magnet.[25]

5.1.3. Scintillator

The scintillator provides a trigger for the muon detector, and is situated in two layers. Each layer covers a slightly smaller area than the chambers, and is positioned for maximum acceptance where the magnetic field is perpendicular to the drift direction. The active trigger area for each layer is approximately $7.4m^2$.[25] The top scintillator is positioned between the top two chambers, and contains only four large area scintillators with two phototubes each in opposite corners of the scintillator. The bottom scintillator is positioned between the bottom two chambers, and is composed of 24 narrow scintillators with phototubes at each end. There are twelve bottom scintillators on the north half of the detector and twelve scintillators on the south half, where all of the scintillator runs in the same direction as the chamber wires. Both the top and bottom scintillator are run by independent high voltage supplies. Each high

voltage is adjusted to a plateau value where small changes in voltage do not significantly change the signal rate.

The scintillator provides time of flight information for muons going through the detector. A trigger is created with a coincidence between the two scintillator planes. $5ns$ resolution on line and $1ns$ resolution using fitting from the track is obtainable.[25] The scintillator signal provides a drift time stop for each chamber and will provide a trigger decision to the level 1 electronics in $500ns$.[30]

5.2. Chamber Electronics

The chamber electronics consist of a monitor board, three motherboards, and a cornerboard. The monitor board monitors chamber parameters through a monitor VME. This includes voltages and gas flows and pressures. The motherboards do the initial processing of the data from the detector and have circuits that handle both the pad and wire signals. All three motherboards connect to a corner board. The corner board is an interface between the chamber electronics and the higher level electronics. It passes commands from the higher level electronics to the motherboards, and transfers the motherboard analog and digital data to the higher level electronics.

5.2.1. Monitor Board

The Monitor Board provides an interface between the chambers and the Monitor VME. The monitor VME, located next to the level 1 electronics, allows the monitoring and adjusting of various analog and binary information. The location of the analog and binary information on the VME is set with an address switch on the monitor board. This is done so that each chamber will have its own analog page and binary description page.

There are 31 possible analog readouts for each chamber. These come in two varieties: analog input/output and analog input. The analog input/output values can both be monitored and adjusted. The most important of these are the wire and pad threshold voltages, which are set at -5.00 volts and -0.40 volts respectively. These values are important because they are used in the chamber electronics to distinguish hits from noise. The other analog input/output values are the pulsing level for the pad test input, and the pulsing level for the wire test input. Both of these values are set at +4.00 volts. Along with the analog input/output values are the analog input values. These values can be viewed, but they can not be adjusted. Voltages, temperatures, and the gas are monitored in this section. The low voltage (+12 volts, -12 volts, +5 volts, and -5 volts) that runs the chamber electronics can be viewed as well as the values of the wire and pad threshold after a diode voltage drop. These values help in troubleshooting chamber problems. The temperatures are monitored for the monitor board, chamber surface, and low voltage supply . It is important that these temperatures do not get too high where they could damage electronic

boards. The gas may be monitored also. The input and output gas flow are displayed along with the input and output gas pressure. Proper flow of the gas is essential for efficient chamber functioning.

In addition to the analog page, each chamber also has binary description pages on the monitor VME. The binary pages contain both binary input and output information. The binary input is a 16-bit chamber identification. An identification tag can be plugged into the monitor board so that the chamber number will be displayed on the monitor VME. The binary output contains 15 bits of information. The first eight of these can be adjusted directly from the monitor VME. One adjustable binary output tells how many layers the chamber has. Another set of five of these adjust the level of coincidence in binary. The coincidence level tells how many layers of the chamber must be hit before an event is accepted as a possible hit. There are also three other adjustable and seven unadjustable output bits.[31]

5.2.2. Motherboards

The motherboards are responsible for the initial processing of the data from the chambers. Each chamber has three motherboards, and each motherboard handles eight columns of cells from the chamber. Both wire and pad signals for one column of cells is sent to the motherboard by a Service Card, which filters off the high voltage from the wire and pad signal.

The motherboards have various subsets of circuitry that include the power supply, the cell address decoder, the control signals, the wire circuitry, and the

pad circuitry. The most important of these are the wire and pad circuitry. The wire circuitry is made up of one basic circuit repeated for each wire pair. The hybrids that run the wire circuitry are the Two Wire Amplifier-Discriminators(2WADs), the Time Voltage Converters (TVCs), and the Delta-Time voltage converters(delta-TVCs). Like the wire circuitry, the pad circuitry is made up of one unit circuit that is repeated for each wire pair. The hybrids that run the pad circuitry are the Charge Sensitive Preamps (CSPs), Baseline Subtractors (BLSs), and the Pad Latch Discriminators (PLDs).[32]

The wire circuitry starts with the 2WADs. Each 2WAD handles the signals from two wires. It amplifies the wire signal, creates an inverted and noninverted output, and then compares the amplified signal with the adjustable wire threshold voltage to decide if the signal is noise or a possible hit. If the hit passes the threshold, then a TTL pulse is produced and sent to the TVCs and delta-TVCs.[32]

The TVC services two wires, but is only connected to one end of the wire pair. It measures the distance between the hit and the wire by measuring the time that it takes the avalanche of electrons produced by the hit to reach the wire. The time that the track went through the chamber is provided by a layer of scintillator which generates the end of the TSTOP timing signal. That time is compared to the time that the wire receives the signal. The time difference is converted to a voltage by a charging capacitor. This voltage is then output on an analog bus. The difference between the two times, and a knowledge of

the avalanche speed in the gas, can be used later to calculate the distance of the hit from the wire.

Like the TVC, the delta-TVC is enabled by TSTOP and handles the signals from one wire pair, but unlike the TVC, the delta-TVC is connected to both sides of the wire pair. The delta-TVC gives a coarse measurement of the hit position along the direction of the wire. It does this by measuring the time difference between the arrival time of the signal at the two ends of the wire. A delay greater than $2l/c$, where l is the length of the chamber, is placed on one end of the wire so that one side always precedes the other. The time difference is converted to a voltage by charging capacitors. The outputs of both the TVC and delta-TVC share analog output busses T1 and T2. T1 carries the first hit of the delta-TVCs and the second hit of the TVCs. Likewise T2 carries the second hit of the delta-TVCs and the first hit of the TVCs.[32]

The pad circuitry starts with the CSPs. Each unit cell contains two pads, a top pad and a bottom pad. The right side of both top and bottom pads are wired together into one output and the left side of both top and bottom pads are wired together into another output. Each CSP handles the signals from one of these outputs, so there are two CSPs for each cell. The CSP integrates the charge on the side of the pad that it is connected to, and produces a voltage that is proportional to the charge on that side of the pad. A comparison of the charge on both sides of one pad can provide a fine adjustment to the position along the wire direction. The output of the CSP goes two places. It goes through a buffer both to a PLD and to a delay that connects to a BLS.[32]

The PLD handles the signals from two pairs of cells independently. It provides digital information to the higher level electronics that are used to create a fast low resolution map of the track. The PLD compares the output of the CSP to an adjustable pad threshold. If the CSP output is more negative than the threshold voltage, then the PAD latch output drops from +5 volts to ground. The pad latch outputs are sent to the Control Board which then sends them to the level 1 electronics for processing.[33]

The output of each CSP goes to one BLS. The BLS subtracts leftover voltage from previous hits, and then amplifies the signal that is left. The output of all the BLSs that are connected to the left side of a pad are placed on the analog bus QA. Likewise all of the outputs from BLSs that are connected to the right side of a pad are placed on the analog bus QB.[32]

5.2.3. Control Board

The Control Board provides the interface between the front end electronics that are mounted on the chambers, and the level 1 electronics that are located in a crate outside the boundaries of the detector. The functions of the control board can be broken down into four basic signal groups. These are the Pulser, Pad Latch, A-Line, and Analog signal lines. The Pulser is used for calibration and testing, and is not of interest here. The pad latch signal line is used for transferring pad latch information to the level 1 electronics. Pad latches from all three motherboards are sent to the control board. The control board in turn sends the latches in groups of 24, corresponding to each deck in the chamber,

to the Module Address Card in the Level 1 electronics where it is processed. When an event passes the level 1 trigger, the addresses of the hit cells are sent back serially from the module address card card to the motherboard through the A-line on the control board. At this point the motherboard's analog signals get transferred to an analog to digital converter through the analog signal lines on the control board. The analog signals from the cells with latched pads are retrieved from the motherboard one cell at a time. They are transferred to the control board on the QA, QB, T1, and T2 analog signal lines. Each signal is inverted, and all of the signals are sent on a analog cable to the analog to digital converter where the analog data is digitized.[34]

5.3. Level 1 Electronics

The VME electronics are located in a VME crate outside the perimeter of the detector itself. It consists of a module address card, coarse centroid trigger card, octant trigger card, fanout card, analog to digital converter, a buffer board, and a processor board. The Module address card receives the latches from the corner board, and creates centroids. The coarse centroid trigger card and octant centroid trigger card then use the centroids created by the module address card to filter out bad hits. The fanout provides the timing signals to synchronise the electronics with the events, the analog to digital converter digitizes the chamber analog data if the track passes the filter. The data is then stored in a buffer board where it is transfered to the level 2 electronics.

The level 2 electronics further filter the data and write the data that passes the filter to disk.

5.3.1. Module Address Card

The Module Address Card is one of the level 1.0 and 1.5 trigger boards. There is one module address card per chamber, making a total of four module address cards for the basement detector. The basic functions of the module address card include relaying timing signals from the Fanout Card to the motherboards, receiving latch bits from the control board, performing zero suppression for data acquisition, and generating trigger patterns.[35]

The module address card handles the pad latch signals, but does not handle any of the analog signals. It receives the pad latches from the control board in three 24 bit words forming a 72 channel hit map of the chamber. A data strobe is used to clock the data into the register.[36] The latch bits are demultiplexed and stored in a 2-stage buffer. The buffered data is then processed by eight EP900 PALs. The PALs generate a map of raw hits or a map of trigger hits based on raw hits. A hit editor and priority encoder process the hit map and loads the addresses of the hits into a FIFO.[35]

The trigger hits generated by the module address card are called centroids. The centroids come in two varieties: fine centroids and coarse centroids. The fine centroids are localized to $\frac{1}{2}$ of a cell or $5cm$. The coarse centroids are a logical OR of the fine centroids, and are three fine centroids wide. The coarse centroids are produced in $100ns$ and are sent to the Coarse Centroid Trigger

Card for a level 1 trigger. If the event passes the level 1 trigger, then the sequencer sends the fine centroids out the front panel to the Octant Trigger Card for a level 1.5 trigger. If the event passes the 1.5 level trigger, then the sequencer toggles the centroid PALs to raw hits and the FIFO is loaded with the hit cells for the readout by data acquisition.[35]

5.3.2. Coarse Centroid Trigger Card

The coarse centroids are read into the Coarse Centroid Trigger Board. The Coarse Centroid Trigger Board accepts input from all three layers of all four chambers.[37] The coarse centroids are OR'ed by four to create a six-cell-wide hit. The Coarse Centroid Trigger Board then uses simple combinational logic to determine if the track passed through the layers of the detector. The logic assumes that the hit will cross at least two out of three cells in a chamber within a three column band. This is consistent with 99% of all of the hits occurring within 45° of zenith.[35] It takes the Coarse Centroid Trigger Board less than 100ns to decide if the event is a hit once all of the inputs are present.[30]

5.3.3. Octant Trigger Card

The Octant Trigger Card is the final stage of the hardware muon trigger.[33] It uses the fine centroids generated in the Module Address Card to form a more detailed level 1.5 trigger decision. The Octant Trigger Card requires that the level 1 Coarse Centroid Trigger Board trigger is passed before it receives the fine centroids. The Octant Trigger Card has a single input, so the Carry Out is

daisy chained between Module Address Cards and provides the order of readout. A data strobe is used to latch the fine centroids into the Octant Trigger Card input buffer. To synchronize this effort a permit to send command is passed between cards.[35] Once all of the centroids are read into the Octant Trigger Card input buffer, parallel RAM memories and a lookup table are used to test each possible centroid combination. Tracks below a programmed monentum cut are discarded. For each successful combination, another lookup table is used to return the angle and monentum of the triggered muon. It takes 1000 to 3000ns for the Octant Trigger Card to make a decision once the input centroids are present.

5.3.4. Fanout Card

The Fanout Card is an interface between the Module Address Card, Analog to Digital Converter, 68000 microprocessor, and external timing clock and trigger system. In the basement, one Fanout Card is used in the VME crate. The functions of the Fanout include VME communication from the 68000 microprocessor, pad latch downloading to the Module Address Card, control signal generation for the Module Address Card, trigger and interrupt processing for the 68000, and control signal processing for the Analog to Digital Converter. The most important of these is the generation of the timing signals.[39]

The timing signals are BEFORE, AFTER, TSTOP, RESET, and UPDATE. They synchronize the actions of the chamber electronics with the higher level electronics. In the basement we create these signals using NIM modules external

to the Fanout Card. The signal from the scintillator ties the timing signals in with the hits going through the chamber to complete the trigger timing. BEFORE and AFTER are timing signals before crossing sample and after crossing sample respectively. BEFORE fires for $250ns$ every $5\mu s$. AFTER fires at the beginning of BEFORE and is up for $3\mu s$. RESET is a TVC reset and is equal to BEFORE. UPDATE allows the storing of one hit and is also set equal to BEFORE. TSTOP is a common TVC stop that fires for up to $2.5\mu s$ when BEFORE pulls down. The Scintillator enable signal begins $650ns$ (cable delay) after TSTOP begins. The end of the scintillator enable corresponds with the end of TSTOP.[38,39]

When the Fanout receives the trigger, it generates an interrupt. The 68000 microprocessor picks up this interrupt and reads the lists of addresses of the hits from the Module Address Card. The 68000 then tells the Motherboard to send the analog data to the Analog to Digital Converter for those channels that were hit. The fanout then sends a command to the Analog to Digital Converter to digitize this analog information. The digitized information is stored in the Analog to Digital Converter until all of the analog data is received from the Motherboard and digitized. The 68000 microprocessor then transfers the digitzed data to a buffer board, which is an interface between level 1 and level 2. The level 2 electronics can then retrieve the data from the buffer board.[39,40]

5.3.5. WWVB Synchronized Clock

The model 8170 WWVB synchronized clock provides the time stamp for each event that is necessary for pointing muon tracks back to a source. The clock has three basic components: the antenna, the receiver, and the VME-clock interface board.

The antenna, as shown in Fig. 5.3.1, is mounted on a 10-foot stand made of one inch O.D. PVC pipe. The bottom of the PVC pipe is mounted on a $2' \times 2' \times 1"$ steel plate, which is buried two feet underground for stability. The antenna is oriented so that it points in the direction of Fort Collins, Colorado, which is the origin of the 100 $\mu V/m$ 60 KHz signal. To orient the antenna properly, it was pointed in the approximate direction of Fort Collins, and then the direction was varied slightly until the strongest possible signal was obtained. The signal cable from the antenna was run through the center of the PVC pipe, and then run underground for a short distance to the building where the cosmic ray telescope is located.

It was found that the antenna had to be located outside of the building. According to the WWVB clock instruction manual[41], if the antenna is mounted within three feet of any steel, or in a building with large steel structural supports, then a 20 dB degradation of the signal-to-noise ratio could occur. The antenna also had to be located as far as possible from any motors, power lines, TV sets, oscilloscopes, and flourtescent or neon lights, since all of these can be sources of RF noise that would interfere with the signal. All of these things were impossible to avoid inside of the building; however, a strong signal
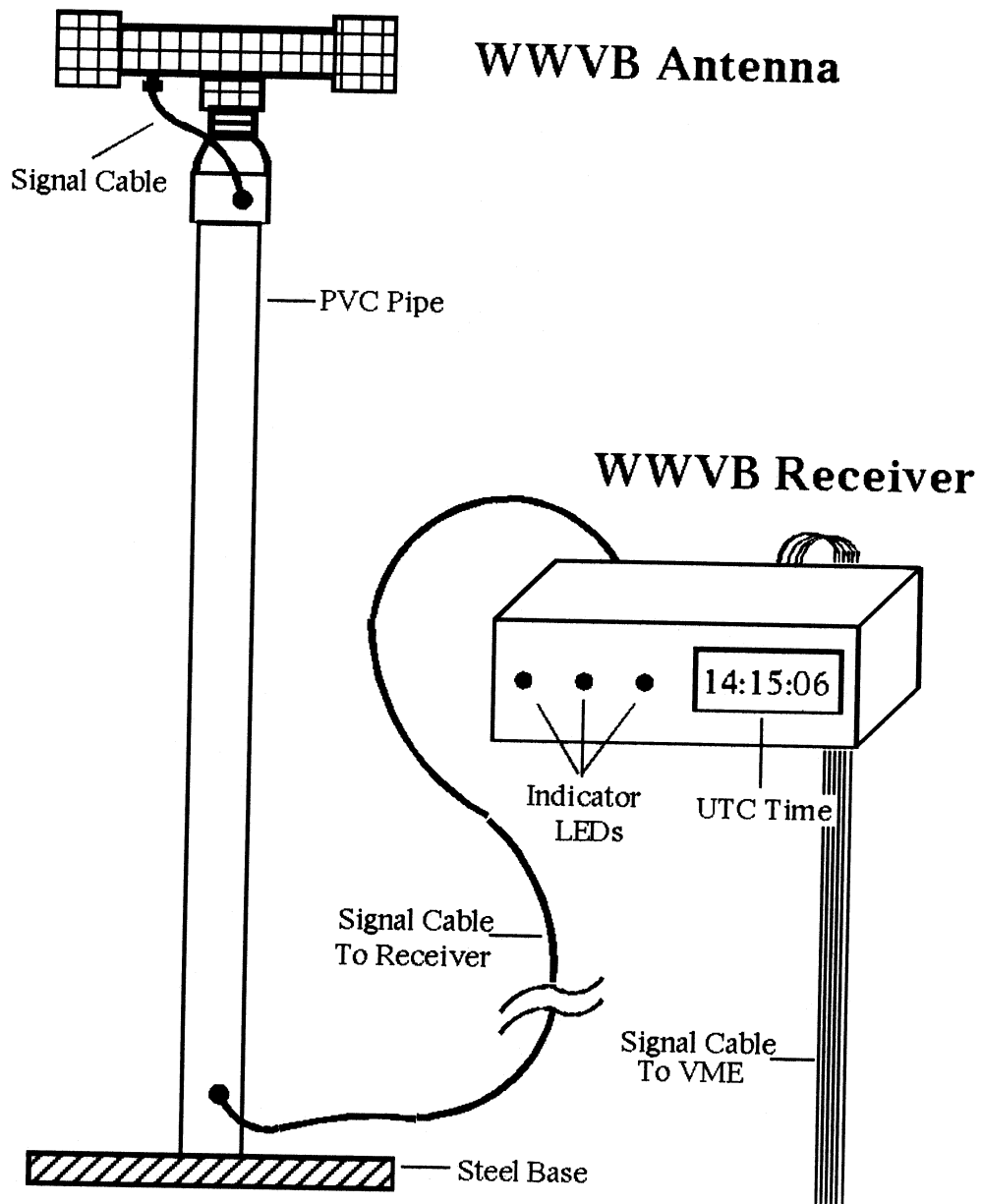
Figure 5.3.1: Antenna for the WWVB synchronized clock.

was obtainable a short distance outside of the building, so the antenna was mounted outside.

The signal cable runs from the antenna to the receiver, which is located near the detector. The front panel of the receiver has indicator LEDs that show the state of the signal. A red "Unlocked" LED lights if the signal is too weak to read, and a green "LOCKED" LED lights if the signal is strong enough to read. Also, a green "SYNCH" LED lights if the signal has been "LOCKED" long enough to synchronize the incoming signal with an internal clock in the receiver. This is provided as a backup so that if the signal is lost for a short period of time, the the clock can still function properly for up to three hours with an uncertainty in the time of ± 100 *msec*. The receiver contains a time zone switch, that allows one to chose the correct time zone, and the front panel of the receiver contains a readout of the local UTC time, as defined in section 3.2.

The receiver is interfaced with the Level-1 electronics with a clock-VME board, which is located with the VME electronics. When the clock-VME board is triggered by a hit, it reads the day of the year, hours, minutes, seconds, time zone, and status data from the receiver. When a hit is read out, this information is sent to the buffer board with the other hit information gathered by the level-1 electronics, where it is stored until it is sent to the level-2 electronics.

Chapter 6
Data Collection and Analysis

Data is collected from the cosmic ray telescope with the help of some computer programs. A level-1 program interfaces the VME electronics with the level-2 electronics, and a program called Taker helps interface the level-2 electronics with the VAX/VMS system that the data is written to. After the data is collected, certain parameters are calibrated, an initial analysis is performed on the data files, and the data files are filtered to obtain a more useful data set. The filtered data is then run through its final analysis, where an attempt to point muon tracks back to Cygnus X-3 is made.

6.1. Data Collection

Run control of the level-1 electronics is provided by an interactive assembler program, by Mike Fortner, called Daq_scint. Daq_scint can be run so that the hits registered by the level-1 and level-1.5 electronics are sent to a computer screen. ADC counts and the position of each track in the three layers of each chamber can be viewed in this mode, along with some simple histograms. These histograms contain the basic digital pad latch and analog (time1, time2, delta time1, delta time2, pad odd A, pad odd B, pad even A, and pad even B) information written for each track. This mode is used mostly for troubleshooting problems on the chambers, since it gives a quick visual display

of where problems are located. Daq_scint can also be run in a mode that writes the hit information (pad latches, analog data, and time stamp), collected in the level 1.0 and level 1.5 electronics, to the level-2 electronics.

The Level 2 and Data Acquisition system writes the event information that passes the level-1 trigger on a MicroVAX computer. When level 1 indicates a good event, digitization occurs and Level 2 is signaled. The supervisor enables the node and initializes the transfer of data. The data is then loaded into the buffer board. The data cable sequencer controls the shipping of data from the buffer to the MicroVAX, and is connected to a multiported memory board in Level 2. The data is available in the Zebra program package, which is a Fortran package for managing data through common blocks with an internal pointer. Though not used in the basement, filter routines written in Fortan can be created, and used offline under VAX/VMS. The data that passes level-2, which is all of the events for our detector, is written to disk in the form of a ZRD file.

When Daq_scint is running in the write to level-2 mode, then an interactive program called Taker can be used to control the level-2 electronics that writes the events to disk. Taker is used to start data runs and provides a running counter of all events written to disk, as well as provides status information on Coordinate, Data Logger, and Daq Filler, which are background processes that help Taker do the complex task of coordinating with the level-2 electronics to write the events to the Vax. Taker also splits data runs up every $\approx 75,000$

events with a limit of nine parts per data run, which can be helpful when one wants to take data for long periods of time.

Lack of disk space is a significant problem with D0muon, which is the VAX/VMS node where the data is collected. There are only $\approx 300,000$ free blocks of space available on the system. Each data file contains $\approx 75,000$ events, which corresponds to an $\approx 140,000$ block file; therefore, there is only room for about two data files on disk. At an average data collection rate of 10Hz, a 75,000 event file can be collected in just over two hours. So in just over four hours of data taking, the entire available disk space on D0muon can be filled. Ideally, one would want to take data continuously 24 hours a day, which would be difficult due to disk space limitations. This problem was solved by Dave Eklund of the University of Arizona. He created a background process that automatically copies the data files to 8mm tape as they are created. After the file is successfully copied to tape, it is deleted from disk, making room for another data file. This background process can be run indefinitely, so that data can be taken continuously for long periods of time. The only limitation in the data taking lies in the program Taker, which only allows nine files per data run, so data runs would have to be restarted every ≈ 18 hours. It takes on the order of 10 minutes to end an old data run and start a new one, so that, ideally, data could be taken in 18 hour segments with ≈ 10 minutes of down time between runs.

6.2. Calibrating and Filtering Data

When the ZRD data files are first collected, they are not ready for their final analysis. First of all, the detector needs to be calibrated to obtain the best possible results. After this an initial analysis of the data needs to be made in order to determine how well the detector and electronics are functioning. Electronic components may need repair, and can be fixed at this point. This whole procedure can be repeated until the detector is functioning satisfactorily. At this point more ZRD data files can be collected. These files are then filtered, so that only events surviving a certain set of cuts are written to DST data files. The data is then ready to analyze with DST programs.

There are calibration constants that must be determined in order for the detector to be used to its fill capabilities. Time, Δtime, t-slope, Δt-slope, pad gain, T_0 constants must all be determined. The first five of these are obtained by taking special kinds of data runs called pedestal and pulser runs. Pedestal runs measure the noise level in each cell of each motherboard. A pedestal is a value above which is considered a hit and below which is considered noise. Pulser runs send controlled pulses separately through the time1, time2, and pad pulser lines on the motherboards. A program called CALIB[42] then processes the information gained in the pedestal and pulser runs and writes the resultant calibration constants to disk. T_0 contants must also be adjusted to account for the variation in internal signal delay in the different motherboards (i.e. varying cable length). This is done by the repetitive use of a program called Tune which uses another program called EXAMINE[43] to adjust the T_o constants until a best

fit value is obtained. A more in-depth treatment of the calibration process can be found in *A Measurement of the Cosmic Ray Muon Charge Ratio Distribution at Sea Level Over the Momentum Range 5-250 GeV/c*, which was written by Richard Mueller.[26]

Examine[43] is used for a preanalysis of the ZRD files. It reconstructs the muon tracks through the detector, and presents this information visually in the form of histograms. The version of Examine used for this preanalysis has histograms of position versus raw hits and position versus track hits for each chamber. These histograms allow the determination of inefficient or noisy cells in the detector. This Examine also contains drift 3-miss and x-offset histograms for each chamber as well as for each motherboard. These histograms are used in the tuning process mentioned above, and give one clues on how well the hits in each column of cells in a chamber agree with the software reconstruction of the track. A file called chamb_eff.out can be created with this Examine and also gives information on how well each chamber is functioning that includes individual chamber efficiencies.

After the calibration and preanalysis procedures are completed, long data runs are taken to create ZRD files. However, the ZRD files are very large and contain a lot of events that are not useful to the analysis, so they must be filtered to obtain smaller more useful files. A program called Filter[44] takes the events one at a time in the each ZRD file, determines if they pass a predetermined set of cuts, and writes the events that pass the cuts to another file, called a

DST file. So Filter is run on a large number of large ZRD files to create a large number of smaller DST files that are used in the next stage of the analysis.

6.3. DST analysis

The Fortran program Dst_kj, written by Ken Johns of the University of Arizona and modified by myself for this thesis, takes the DST files created by filter and analyzes the track information as outlined earlier in Chapters 3 − 4. The program is divided up into small input data files and subroutines that each have a specific function. The most important parts of the program are the primary input data file Inddd, the main program Dst_kj, the phase calculating subroutine phase_comp_new, and the histogram creating subroutine Kj_hists.

6.3.1. Input Data File

Inddd is an input data file that allows certain parameters used in the DST program to be changed. The first parameter is the number of Dst data files that the program will analyze from a list of DST files listed in a data file called files.dat. This allows to quick test the program with a small number of files, or to run the program using all of the available data files by changing one parameter. A set of parameters relate to the source that one wishes to look at. These parameters allow the program to look at different sources (i.e. Cygnus X-3, Hercules X-1, etc.) by changing a small number of parameters, or to look at the same source using different ephemeri. For example, the positional right ascension and declination of the source for both the epochs 1897.5 and 2000 can

be changed. The orbital period, orbital period reference, superorbital period, superorbital reference, pulser period, and pulser period reference can also be changed. There are also adjustable parameters that relate to the shape of the orbit, and a reference to the the time that the object crosses the meridian. There are three detector parameters that set the longitude, latitude, and altitude of the detector, allowing the program to be able to be used with different detectors. There are also a set of cuts, that allows one to narrow the data set. Cuts can be set on the size and shape of the window centered on the source, the region of the detector allowed for hits, and goodness of fit parameters in both the bend and non-bend views. Table 6.3.1 summarizes the values of the parameters used in Inddd for this experiment.

6.3.2. Main Program

Dst_kj is the master program of the DST analysis. It opens the DST files, one at a time, which are listed in a data file called files.dat. For each event, the program first calculates the x, y, and z cosine angles both entering and leaving the detector, a quality of fit parameter for both the non-bend and bend views, an x and z magnet position, and a momentum using a subroutine called Mudsti. These quantities, along with a time stamp and the parameters set in the Inddd data file become the basis for the rest of the program.

The DST program then makes all of the time calculations as outlined in Section 3.2, and the barycycle corrections using the jpl ephemeris as defined

Table 6.3.1: A list of the parameters used looking for muon tracks from Cygnus X-3.

Parameter	Value
Number of Dst Files Analyzed	83
Right Ascension (1987.5)	307.99583°
Declination (1987.5)	40.91500°
Right Ascension (2000)	308.10843°
Declination (2000)	40.95790°
Pulser Period	0.0 *Seconds*
Superoribital Period	34.1 *Days*
Pulser Period Reference	2440949.9013 *Julian Days*
Oribital Period Reference	2440949.9013 *Julian Days*
Superoribital Period Reference	2440949.9013 *Julian Days*
Eccentricity of Orbit	0.00
Detector Longitude	−5.884106 *Hours East*
Detector Latitude	41.837856°
Detector Altitude	200 *Meters*
Type of Window	*Elliptical*
Size of Window	10.0° × 1.0°
Cut On X − Coordinate At Magnet	*None*
Cut On Y − Coordinate At Magnet	*None*
Cut On Bend − View χ^2	*None*
Cut On Non − Bend − View χ^2	4.0
Cubic Fit Data Run	
Orbital Period	0.19968196 ± 0.00000042 *Days*
$\frac{d}{dt}$ (*Orbital Period*)	2.18×10^{-9}
$\frac{d^2}{dt^2}$ (*Orbital Period*)	-4.38×10^{-13} *Days*$^{-1}$
Parabolic Fit Data Run	
Orbital Period	0.19968196 ± 0.00000042 *Days*
$\frac{d}{dt}$ (*Orbital Period*)	0.94×10^{-9}
$\frac{d^2}{dt^2}$ (*Orbital Period*)	0.00 *Days*$^{-1}$

in Section 3.3.4, using the routines Get_time and Baryjpl respectively. At this point the cut on the goodness of fit parameter is made.

The coordinate transformations, as shown in Section 3.1, are made using the calculated times and direction cosines. A subroutine called Get_zenazi calculates the zenith and azimuth angles of the track from the cosine angles. Then a subroutine called Get_radec calculates the right ascension and declination of the track from the zenith and azimuth angles along with the time. A cut on the zenith angle, as set in the Inddd data file, is made at this time. At this point, an initial set of histograms are produced showing the results of these calulations on this uncut DST data.

At this point, windows are opened, as outlined in Section 3.3.1, to search for an excess of events from Cygnus X-3. One window is centered on the position of Cygnus X-3, and 35 background windows are spaced every 10 degrees of right ascension with the same declination. The size of the windows were adjusted in the Inddd data file so that all of the windows touched but did not overlap.

A routine called Radec2zenazi calculates the detector coordinates of the center of each window at the time that each track passes through the detector. The angle between the center of each window and the track, called theta, is calculated using detector coordinates. This angle is weighted differently in the bend and non-bend coordinate due to the difference in detector resolution in these directions. If this angle is less than the cut set in the Inddd data file ($10° \times 1°$ elliptical cut) for any of the 36 windows, then the track information is further processed for whichever window the track happened to fall in. The

phase of each track is then calculated, for its specific window, in a subroutine called Phase_comp_new. The same theta and phase calculations are performed on the data with three stricter cuts for comparison. These three cuts only look at events from the original windows that have a momentum greater than 10 GeV/c, 25 GeV/c, and 100 GeV/c respectively. Another set of histograms are created here to summarize the information for each set of windows.

At this point, a third set of histograms is created that show information on data from the window centered on Cygnus X-3. Also summary information is written to a data file called print_kj.dat. This summary information contains the number of events that fall within each phase interval for each window, as well as their uncertainties. This is done for the standard $10° \times 1°$ elliptical windows, and the three sets of $10° \times 1°$ elliptical windows with the 10 GeV/c, 25 GeV/c, and 100 GeV/c restrictions on momentum. Background estimates for each phase interval are also included.

6.3.3. Phase Calculating Routine

One of the most important subroutines in the DST analysis program is called Phase_comp_new, which calculates the phase of each track that falls into one of the windows. The phase is calculated using Eq. 3.12, and the T_0 correction for the background windows is made using Eq. 3.13. For comparison, the phases were also calculated without the T_0 corrections in a similar subroutine called Phase_comp. The ephemeris values used to calculate the phase, as defined in Table 3.1, were set in the Inddd data file.

6.3.4. Histogram Routine

The subroutine Kj_hists creates all of the histograms using HBOOK4[45], and writes them to a file called Kj_hists.dat. Here they can be viewed on a computer screen or printed on a laser printer with the help of Display5[46], which is an interactive program used to create the histograms from the data files. Three sets of histograms are printed.

The first set of histograms show information on the initial calculations done on the uncut DST data, such as the azimuth, zenith, right ascension, and declination angles. It also contains histograms which show chamber performance information, such as a goodness of fit parameter in both the bend and non-bend view, as well as track positions at the magnet in the x and z directions.

The second set of histograms contains all of the information about the 36 windows that were opened. 10 histograms were created for each of these windows. The first four plots were the phase plots for the standard $10° \times 1°$ elliptical window, and the three $10° \times 1°$ elliptical windows with momentum cuts of 10 GeV/c, 25 GeV/c, and 100 GeV/c. The second four histograms of this group are scatter plots of the right ascension versus declination for each corresponding phase plot. The next four histograms are θ versus phase scatter plots for each of phase histogram, where θ is the angle between the track and the center of one of the windows. The final four histograms in this group are one dimensional θ plots for the above windows.

The second set of histograms also contains phase plots that are the summation of all of the background windows, and a plot comparing how many events fall within each of the 36 windows. These window-to-window variations are also shown with two dimensional scatter plots that show the variations in phase or θ in the 36 opened windows.

A third set of histograms show information similar to the first set of histograms for events that pass all of the cuts and all fall within the $10° \times 1°$ elliptical window centered on Cygnus X-3. One dimensional zenith, azimuth, right ascension, and declination plots are included, as well as a two dimensional scatter plot showing time versus zenith angle folded every 24 hours modulo 1, where the time scale is adjusted so that the time that Cygnus X-3 crosses the meridian is set to 0.5 on the $0.0 - 1.0$ scale.

Chapter 7
Experimental Results

The deterioration of the muon chambers, slow development and updating of the VME electronics, and time constraints based on when the cosmic ray telescope would be disassembled did not allow the collection of the valuable new data set. So instead, I ran my complete analysis on an older set of data collected with the cosmic ray telescope from September 13 to December 12, 1989. I only used data runs that were longer than 2 hours long, since this represents about half of the orbital period of the Cygnus X-3 system, and thus would give a large contribution to the phase histograms. The remaining data set contained 83 files with over 11.3 million events with a live time of $\approx$ 313.5 hours. There were 3,478,283 events that passed the filter, and 8,226 events in a $10° \times 1°$ elliptical window centered on Cygnus X-3. This is a larger data set than collected by experiments claiming to see Cygnus X-3. It is important to note that the data was filtered with the pad fit off. Normally, one would want to filter with the pad fit on, since it greatly increases the resolution in the wire direction. However, a problem was found with the pad fit that was never cured. The cosine squared of the zenith angle is known to be linear. When the files are filtered with the pad fit off this distribution is smooth, but when filtered with the pad fit on the distribution becomes vary ragged. Since this problem was never resolved, the final data set was filtered with the pad fit off.

7.1. Search for a DC excess from Cygnus X-3

In an attempt to look for a DC excess of events coming from the direction of Cygnus X-3, a window centered on Cygnus X-3 and 35 background windows centered on the same declination band spaced every 10° right ascension were used. Four sets of these windows were opened. The first of these used 10° × 1° windows, while the other three sets of windows were the same size with momentum cuts of 10 GeV/c, 25 GeV/c, and 100 GeV/c.

Right ascension versus declination scatter plots were made of the events in all of the windows, which is similar to a plot used in the Fréjus experiment.[23] Figures 7.1.1- 7.1.4 are plots of the windows centered on Cygnus X-3 for the 10° × 1° elliptical window, the window with the 10 GeV/c momentum cut, the window with the 25 GeV/c momentum cut, and the window with the 100 GeV/c momentum cut respectively. They are scatter plots with the right ascention of each track minus 307.9° on the x-axis and declination of each track minus 40.9° on the y axis. This is done so that the position $(0,0)$ on the plots represents the position of Cygnus X-3.

One interesting point about Figures 7.1.1 - 7.1.4 is their shapes. Elliptical cuts were made; however, the scatter plots of the data taken from these cuts are in the shape of an elongated bowtie. These shapes can easily be explained once one realizes that there are two mechanisms at work. One makes the elliptical plot look like a bowtie, while the other compresses the plot along its declination axis to give the plot its elongated shape.

N=8,226
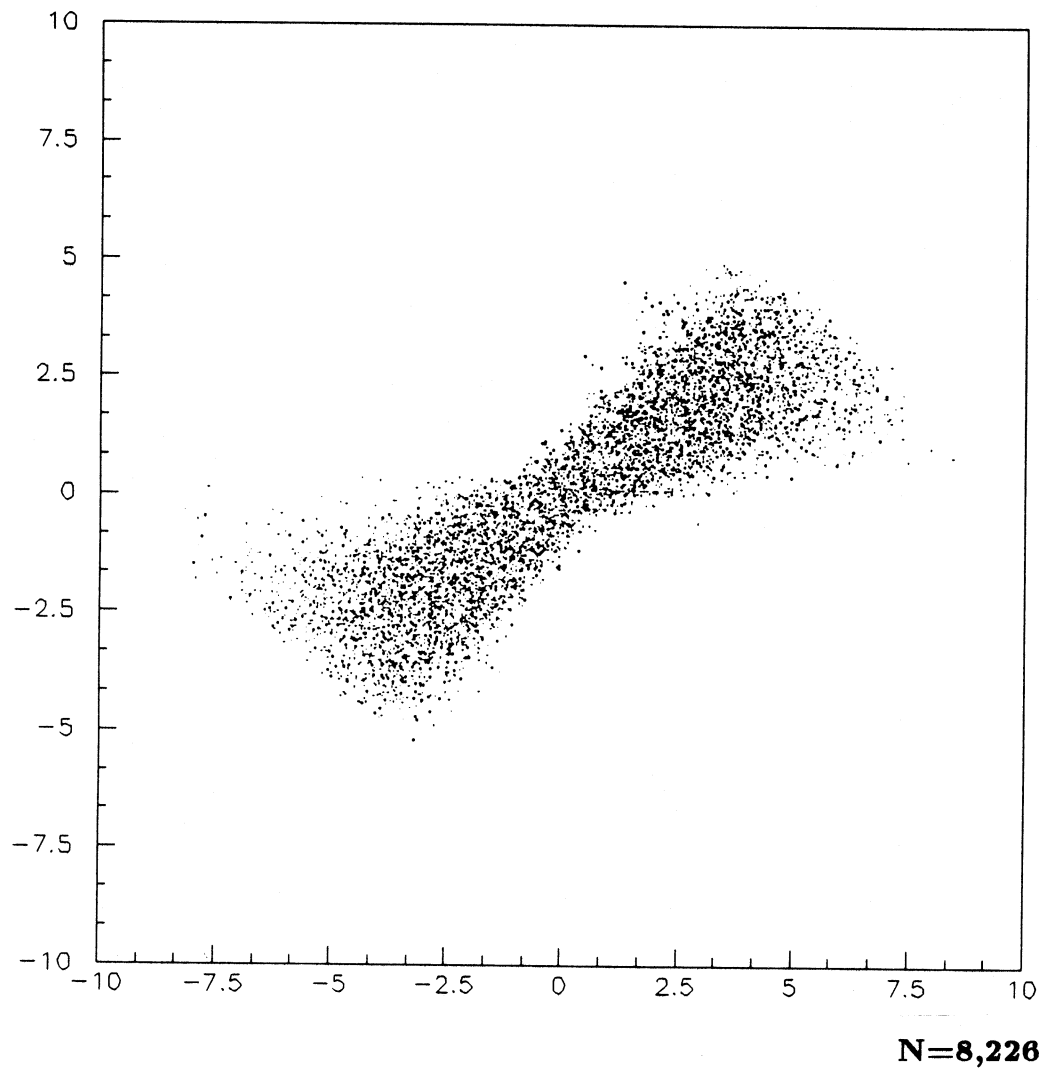
$10° \times 1°$ **window;   Right Ascension vs. Declination**

Figure 7.1.1: A projection of the $10° \times 1°$ elliptical window centered on Cygnus X-3. The x-axis is degrees right ascension from Cygnus X-3, and the y-axis is degrees declination from Cygnus X-3.

N=4,289
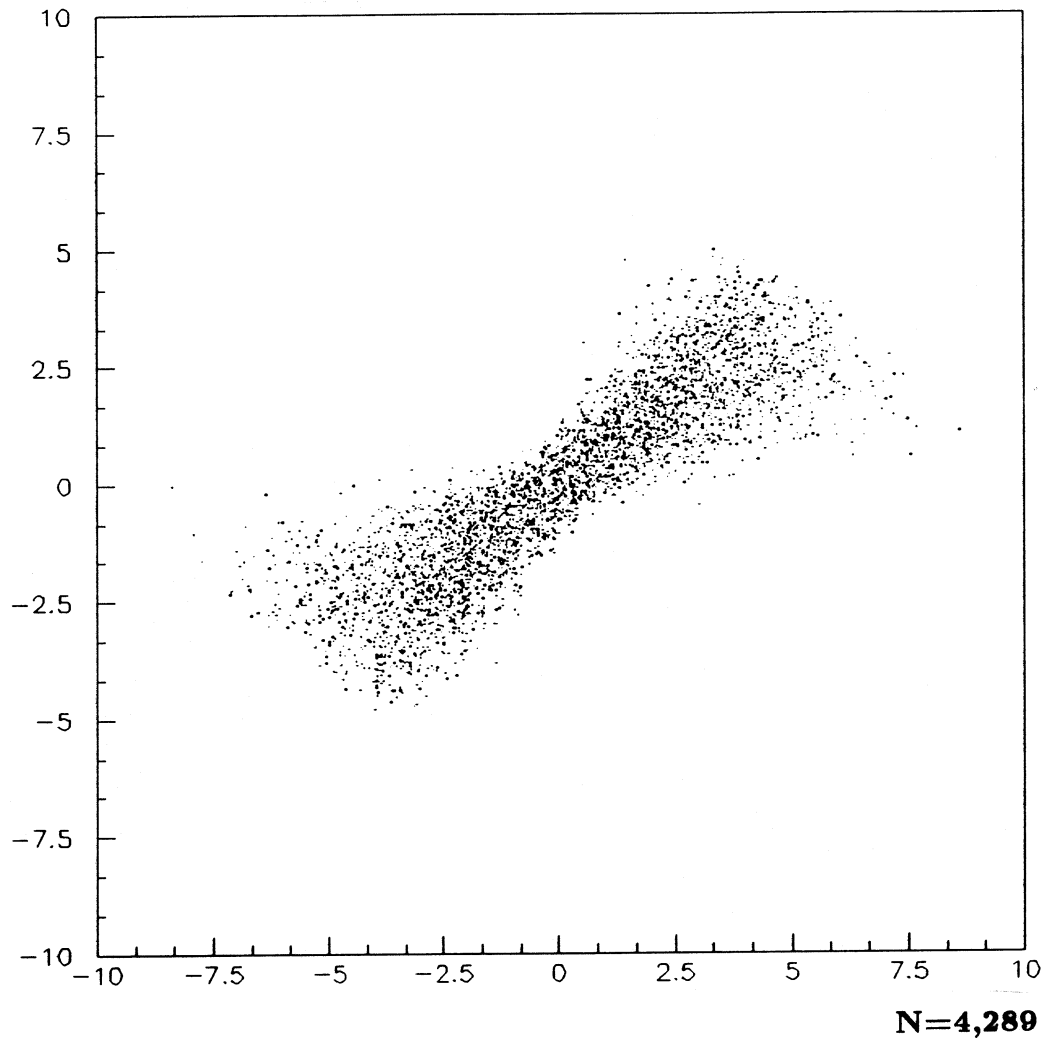
$10° \times 1°$ **window;** $p \geq 10GeV/c$; **Right Ascension vs. Declination**

Figure 7.1.2: A projection of the $10° \times 1°$ elliptical window centered on Cygnus X-3, with a 10 GeV/c restriction on momentum. The x-axis is degrees right ascension from Cygnus X-3, and the y-axis is degrees declination from Cygnus X-3.

$10° \times 1°$ **window**; $p \geq 25 GeV/c$;   **Right Ascension vs. Declination**

N=1,717

Figure 7.1.3: A projection of the $10° \times 1°$ elliptical window centered on Cygnus X-3, with a 25 GeV/c restriction on momentum. The x-axis is degrees right ascension from Cygnus X-3, and the y-axis is degrees declination from Cygnus X-3.

N=452

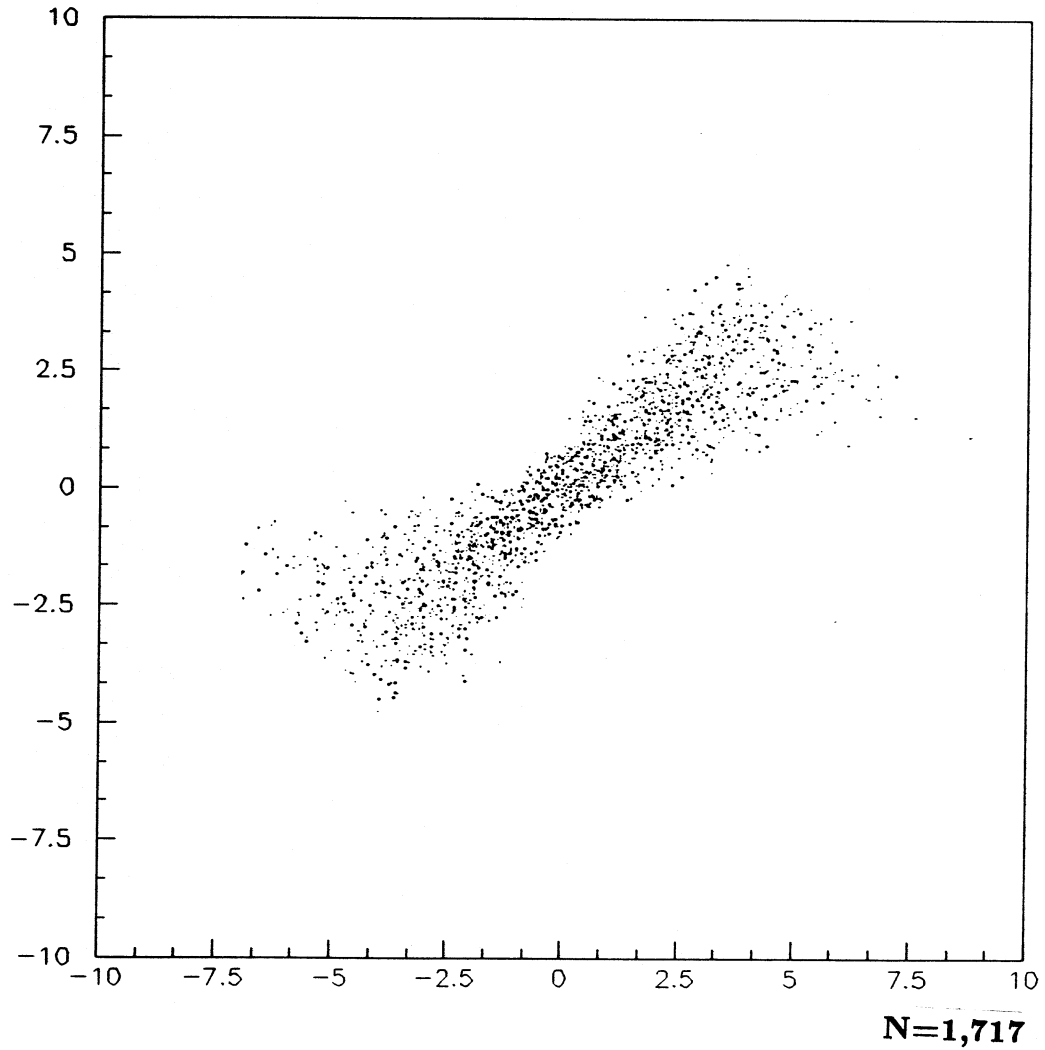10° × 1° **window;** p ≥ 100*GeV/c*; **Right Ascension vs. Declination**

Figure 7.1.4: A projection of the 10° × 1° elliptical window centered on Cygnus X-3, with a 100 *GeV/c* restriction on momentum. The x-axis is degrees right ascension from Cygnus X-3, and the y-axis is degrees declination from Cygnus X-3.

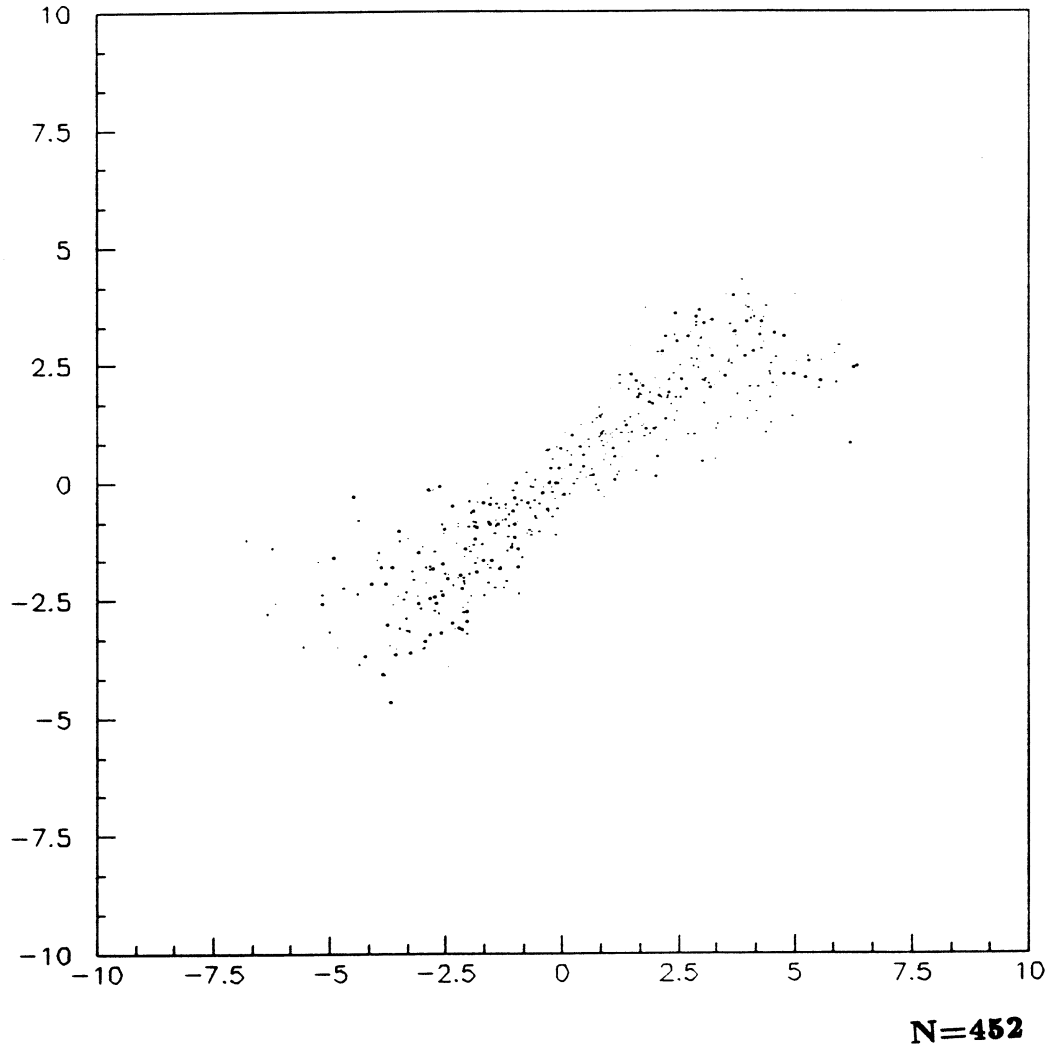The bowtie shape is a result of the fact that the orientation of the right ascension and declination coordinates are not always constant with the orientation of the detector drift and non-drift coordinates that our elliptical cut was made on. The bowtie shape is actually the superposition of many ellipses of slightly different orientations on our right ascension versus declination scatter plots. If the data had been taken from the entire time that Cygnus X-3 was above the horizon, then the overlapping ellipses would have made a complete circle on the scatter plot. This would leave one to believe that we should still get circular plots. However, data from this experiment was not taken at all possible times for Cygnus X-3. In fact, most of the data was taken with Cygnus X-3 in similar orientations in the sky, and thus with similar orientations with respect to the detector coordinates. So for the accumulation of all of the data, one would expect to see the bowtie shape seen in the right ascension versus declination scatter plots.

The second characteristic of the scatter plots is that fact that they appear to be elongated along the right ascension axis, or compressed along the declination axis. This can be explained if we first consider what a window with a circular cut would look like, and if one thinks of this circular window as a telescope field of view. The size of the field of view of our telescope does not change as it is moved around the celestial sphere, but the number of degrees of right ascension that the field of view subtends can change depending on its position on the celestial sphere. The lines of declination run parallel to the celestial equator, while the lines of right ascension run perpendicular to the celestial

equator and intersect at both celestial poles. So the distance between any two lines of declination remains constant (since they will always be parallel), and the distance between any two lines of right ascension are a maximum at the celestial equator and decrease as either pole is approached. A $5°$ circular half cone window will subtend $\approx 10°$ in both right ascension and declination at the celestial equator. When the same window is moved to $+40.9°$, where Cygnus X-3 is located, it will subtend $10°$ in declination and $\approx 15°$ in right ascension. So plotting these windows on a square axis with equal sides makes circular half cone windows look like ovals that are compressed along the declination axis. To verify that this effect occurs, two sets of windows were opened. One set was centered on Cygnus X-3, while the other was centered on the celestial equator. The scatter plots centered on the celestial equator looked circular, while the ones centered on Cygnus X-3 were compressed along the declination axis. If these results are applied to our elliptical cut windows, we would expect to have bowtie shaped windows that are compressed along the declination axis, which is exactly what is seen in Figures 7.1.1 - 7.1.4.

Other experiments had tried using right ascension versus declination scatter plots, with circular windows, to see if there was an obvious signal coming from Cygnus X-3. If there is a measurable signal coming from Cygnus X-3, then one would expect that there be more events bunched toward that center of the distribution. This would be easiest to see for a circular window, and since the distributions have a characteristic bowtie shape, it is hard to tell if there are more events closer to the position of Cygnus X-3. Since the bowtie shape is

the result of overlapping ellipses, one would expect there to be less events on the outside edges than in the central part of the distribution. This is seen in Figures 7.1.1 - 7.1.4 as well as in all of the background distributions. Contour plots were made of source and background windows. There was no noticable difference between the source and background plots, suggesting that there is no significant signal coming from the direction of Cygnus X-3. Larger $20° \times 2°$ elliptical plots as well as $10°$ and $20°$ circular plots were analyzed in a similar manner. These plots also showed no significant signal coming from Cygnus X-3.

Recall that for each window centered on Cygnus X-3 there are 35 other equivalent background windows at the same declination as Cygnus X-3 and spaced every $10°$ right ascension. Therefore, since these windows should not overlap, they can subtend no more than $10°$ in right ascension. It was found by trial and error that the $10° \times 1°$ elliptical windows touch but do not overlap.

Table 7.1.1 summarizes the number of events counted in each window for the standard $10° \times 1°$ elliptical set of windows as well as the three sets of $10° \times 1°$ elliptical windows with momentum cuts of 10 GeV/c, 25 GeV/c, and 100 GeV/c. Similar results are seen for all four cases. There are very few events coming from more than $120°$ right ascension from Cygnus X-3. The number of events greatly increases to a small plateau from about $0°$ *to* $60°$ right ascension from Cygnus X-3. The window centered on Cygnus X-3 ($0°$ window) is not at the center of the gently sloping plateau, but is on one of the edges of the plateau. These distributions can be expected. Most of the data runs were started $2-4$ hours before Cygnus X-3 crossed the meridian. Problems

Table 7.1.1: Comparison of the number of events that fell within each of the 36 windows opened for each set of windows. The first column of data represents the events collected in the standard $10° \times 1°$ elliptical windows, while the three other columns of data represent the events in each window given different momentum cuts.

Window	Number of Events			
	Standard	> 10 GeV/c	> 25 GeV/c	> 100 GeV/c
−170°	0 ± 0.00	0 ± 0.00	0 ± 0.00	0 ± 0.00
−160°	0 ± 0.00	0 ± 0.00	0 ± 0.00	0 ± 0.00
−150°	0 ± 0.00	0 ± 0.00	0 ± 0.00	0 ± 0.00
−140°	0 ± 0.00	0 ± 0.00	0 ± 0.00	0 ± 0.00
−130°	5 ± 2.24	2 ± 1.41	0 ± 0.00	0 ± 0.00
−120°	3 ± 1.73	2 ± 1.41	2 ± 1.41	1 ± 1.00
−110°	24 ± 4.90	18 ± 4.24	8 ± 2.83	3 ± 1.73
−100°	98 ± 9.90	49 ± 7.00	20 ± 4.47	7 ± 2.65
−90°	270 ± 16.43	141 ± 11.87	52 ± 7.21	14 ± 3.74
−80°	588 ± 24.25	323 ± 17.97	124 ± 11.14	34 ± 5.83
−70°	1,196 ± 34.58	640 ± 25.30	249 ± 15.78	61 ± 7.81
−60°	2,245 ± 47.38	1,211 ± 34.80	509 ± 22.56	145 ± 12.04
−50°	3,459 ± 58.81	1,821 ± 42.67	789 ± 28.09	208 ± 14.42
−40°	4,592 ± 67.76	2,486 ± 49.86	982 ± 31.34	241 ± 15.52
−30°	5,969 ± 77.26	3,117 ± 55.83	1,231 ± 35.09	337 ± 18.36
−20°	6,932 ± 83.26	3,632 ± 60.27	1,461 ± 38.22	366 ± 19.13
−10°	7,562 ± 86.96	4,032 ± 63.50	1,636 ± 40.45	399 ± 19.97
0°	8,226 ± 90.69	4,289 ± 65.49	1,717 ± 41.43	452 ± 21.26
10°	8,668 ± 93.10	4,552 ± 67.47	1,861 ± 43.14	457 ± 21.38
20°	8,931 ± 94.50	4,704 ± 68.59	1,843 ± 42.93	444 ± 21.07
30°	8,860 ± 94.13	4,591 ± 67.76	1,825 ± 42.72	466 ± 21.59
40°	9,016 ± 94.95	4,751 ± 68.93	1,876 ± 43.31	455 ± 21.33
50°	8,828 ± 93.96	4,698 ± 68.54	1,871 ± 43.26	439 ± 20.95
60°	8,198 ± 90.54	4,375 ± 66.14	1,754 ± 41.88	425 ± 20.62
70°	7,426 ± 86.17	3,935 ± 62.73	1,535 ± 39.18	366 ± 19.13
80°	6,092 ± 78.05	3,209 ± 56.65	1,261 ± 35.51	291 ± 17.06
90°	4,712 ± 68.64	2,476 ± 49.76	934 ± 30.56	227 ± 15.07
100°	3,204 ± 56.64	1,671 ± 40.88	634 ± 25.18	143 ± 11.96
110°	2,065 ± 45.44	1,052 ± 32.43	357 ± 18.89	88 ± 9.38
120°	1,149 ± 33.90	562 ± 23.71	220 ± 14.83	43 ± 6.56
130°	517 ± 22.74	249 ± 15.78	96 ± 9.80	27 ± 5.20
140°	208 ± 14.42	113 ± 10.63	39 ± 6.24	7 ± 2.65
150°	71 ± 8.43	34 ± 5.83	12 ± 3.46	3 ± 1.73
160°	19 ± 4.36	9 ± 3.00	3 ± 1.73	2 ± 1.41
170°	6 ± 2.45	1 ± 1.00	1 ± 1.00	0 ± 0.00
180°	2 ± 1.41	1 ± 1.00	0 ± 0.00	0 ± 0.00

with the data collection system often ended runs shortly before or after Cygnus X-3 crossed the meridian. The number of muons seen is proportional to the cosine squared of the zenith angle, so 75% of the events seen will come from within 45° of zenith. So it would be expected that many of the events come from a small number of windows with Cygnus X-3 on the tailing edge of the plateau with a smaller number of events on each side of the plateau.

Ideally, data runs in even multiples of the sidereal day are preferred, so that all windows have equal exposure to the detector. This way all of the windows could be used to determine the background rate as outlined in Section 3.3.1. The distribution that we have in Table 7.1.1 is time biased, since all of the windows do not have equal time exposures to the detector. This makes the ideal analysis impossible, and any kind of analysis hard to validate. The only thing that can be done is to try to obtain some useful information out of the data that is on the gently sloping plateau from 0° *to* 60° right ascension from Cygnus X-3. So I will treat the six windows from 10° *to* 60° as the background windows.

For the $10° \times 1°$ half cone windows, the average of the background windows is $8,750.2 \pm 38.2$ events. This is ≈ 524 events greater than the number of events seen in the window centered on Cygnus X-3, well out of the range of the uncertainties. Similar results are seen with the next two sets of windows. The average number of background events for the windows with the 10 *GeV/c* momentum cut is $4,611.8 \pm 27.7$, which is ≈ 322 events more than in the source window. Similarly, the average number of background events for the

windows with the 25 GeV/c momentum cut is $1,838.3 \pm 17.5$, which is ≈ 121 events more than in the source window. The only set of windows that did not show more events from the background windows, was the set of windows with the 100 GeV/c momentum cut. Here there were 447.6 ± 8.6 events in the background window, which were five events fewer than in the source window. This is, however, well within the uncerainties of the source and background windows. The above results show that the time bias mentioned earlier has made it impossible to even use the six windows on the plateau to estimate the background. Therefore, the data set collected in this experiment can not be used to look for a DC excess of events coming from Cygnus X-3. The only way to avoid this time bias is to collect data sets in even multiples of the sidereal day.

7.2. Search for a Periodic Signal from Cygnus X-3

It was shown that the data set used here could not be used to look for a DC excess of events over background coming from Cygnus X-3; however, most experiments that looked for muon tracks coming from Cygnus X-3 did not see a significant DC excess anyway. The strongest evidence cited by some experiments was the correlation of the phase distribution with the 4.8 hour X-ray period. The Soudan-1 and NUSEX experiments saw narrow peaks, no wider than 0.10 *to* 0.15, in the phase distribution in the range 0.65 *to* 0.90, which corresponds to the peak in the x-ray distribution. So even if we can not successfully calculate the background, we should be able to gain some valuable

information by looking at the shape of the phase distribution calculated from our data set. The 1988 van der Klis and Bonnet-Bidaud ephemeris is used to calculate the phase of each track. The cubic fit published in the above article is believed to be the best fit; however, most muon experiments cite the parabolic fit published in 1981 by the same authors since their experiments were performed before the 1988 publication. Therefore, in this experiment, the phase was calculated using both fits for comparison.

Figure 7.2.1 shows the phase plot using both the cubic and parabolic fits for the $10° \times 1°$ elliptical window centered on Cygnus X-3. Figures 7.2.2 - 7.2.4 show the same thing for the windows with the 10 GeV/c, 25 GeV/c, and 100 GeV/c cuts on momentum, respectively.

All four sets of plots in Figures 7.2.1 - 7.2.4 show similar distributions. All of the cubic fit plots have a definite minimum at a phase in the range of $0.4 - 0.50$, and increase on either side of that. The maximum of these plots occurs around $0.9 - 0.95$, and contains about double the number of events than the minimum phase bin. The standard $10° \times 1°$ elliptical window has a minimum of 276 ± 16.6 events at a phase range of $0.50 - 0.55$, and a maximum of 587 ± 24.2 events at a phase range of $0.90 - 0.95$. The window with the 10 GeV/c cut on momentum looks similar, and has a minimum of 162 ± 12.7 events at a phase range of $0.45 - 0.50$, and a maximum of 332 ± 18.2 at a phase range of $0.85 - 0.90$. The window with the 25 GeV/c cut on momentum has a minimum of 51 ± 7.1 events at a phase range of $0.35 - 0.40$, and a maximum of 145 ± 12.0 at a phase range of $0.85 - 0.90$. And the window with the 100 GeV/c cut on momentum has a

N= 8226, H= 2000
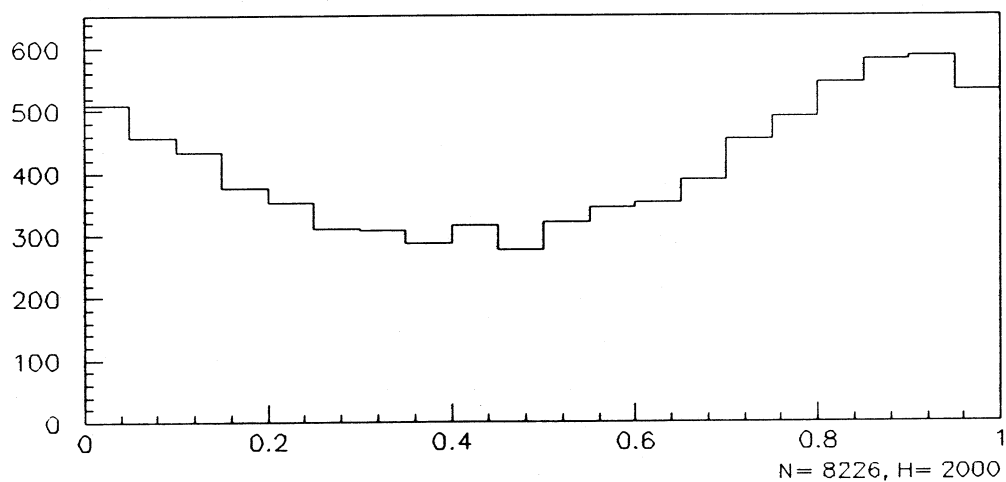
10° × 1° window;   Cubic Fit;   Phase

N= 8226, H= 2000
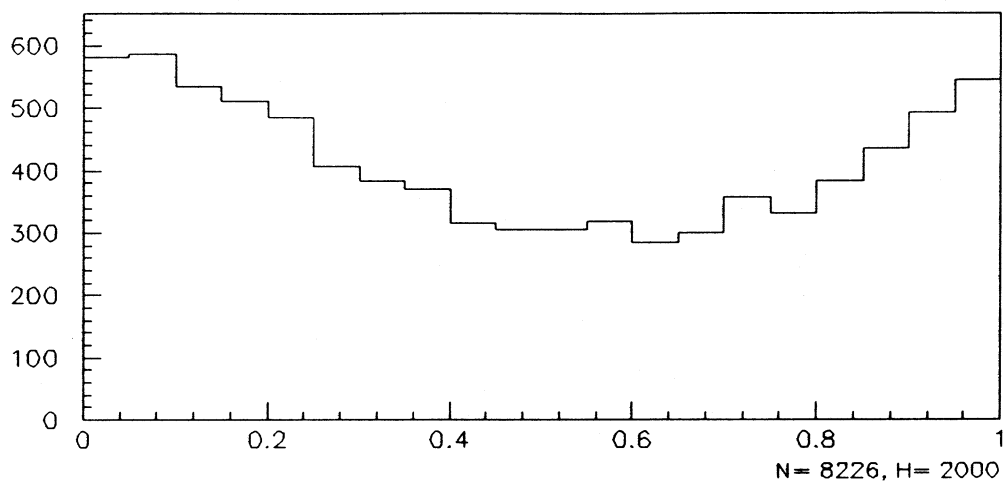
10° × 1° window;   Parabolic Fit;   Phase

Figure 7.2.1: The phase plot for the $10° × 1°$ elliptical window centered on Cygnus X-3 using both the cubic and parabolic fits.
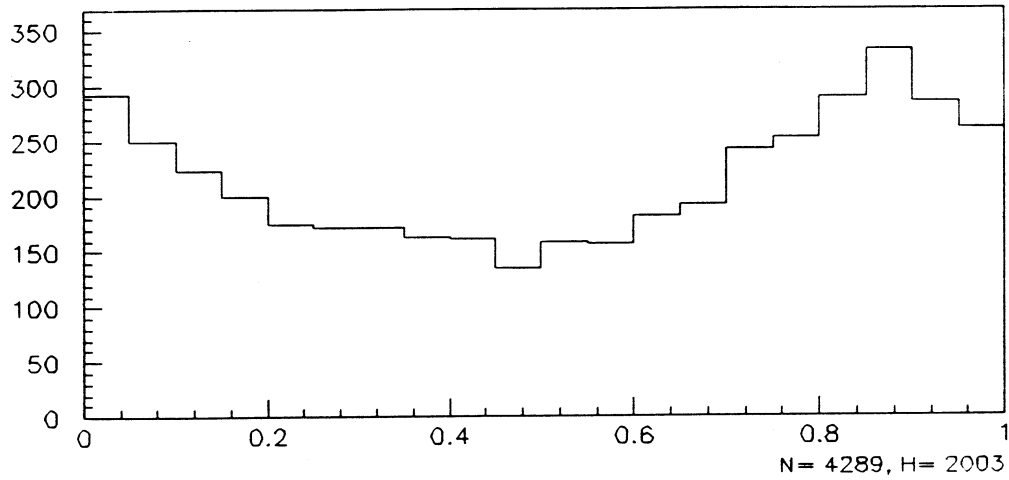
$10° \times 1°$ **window**; $\text{p} \geq 10 GeV/c$; **Cubic Fit**; **Phase**
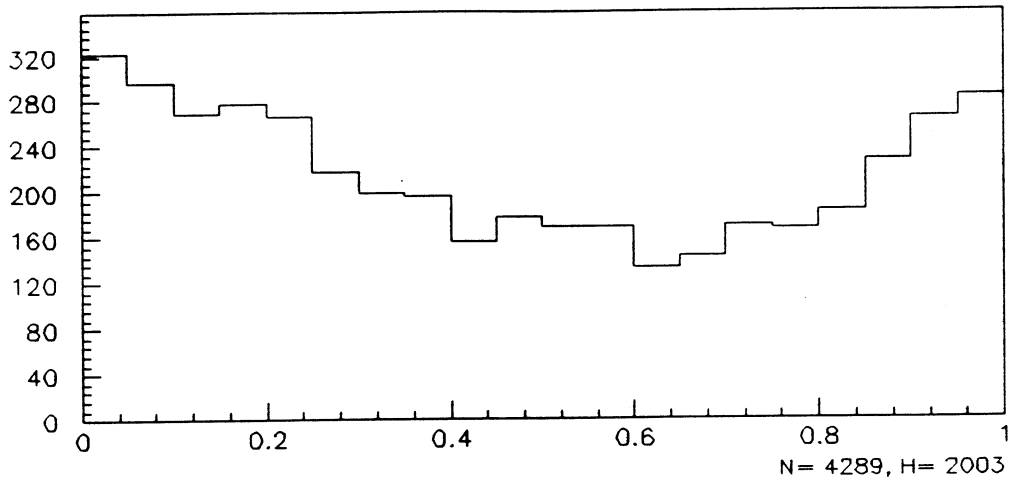
$10° \times 1°$ **window**; $\text{p} \geq 10 GeV/c$; **Parabolic Fit**; **Phase**

Figure 7.2.2: The phase plot for the $10° \times 1°$ elliptical window centered on Cygnus X-3, with a 10 GeV/c cut on momentum, using both the cubic and parabolic fits.
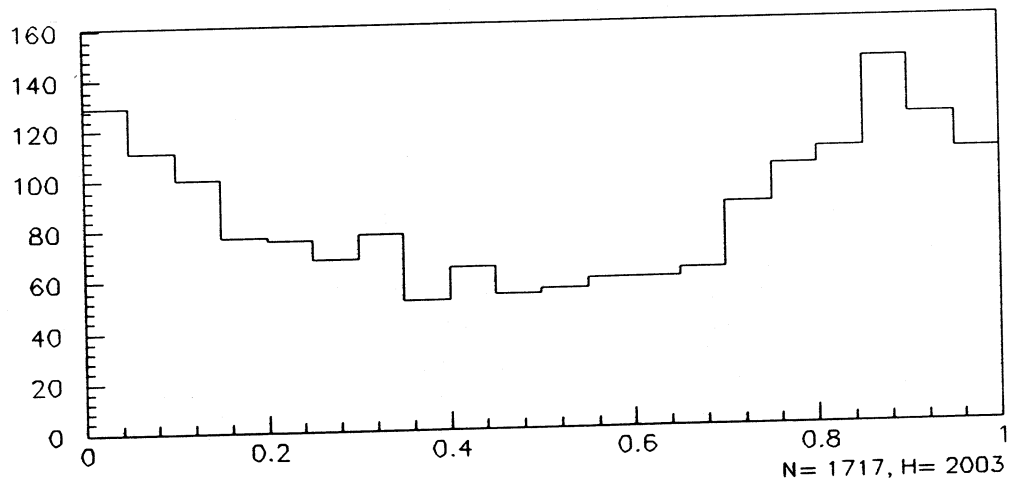
$10° \times 1°$ **window;** $\quad$ **p** $\geq 25 GeV/c;$ $\quad$ **Cubic Fit;** $\quad$ **Phase**
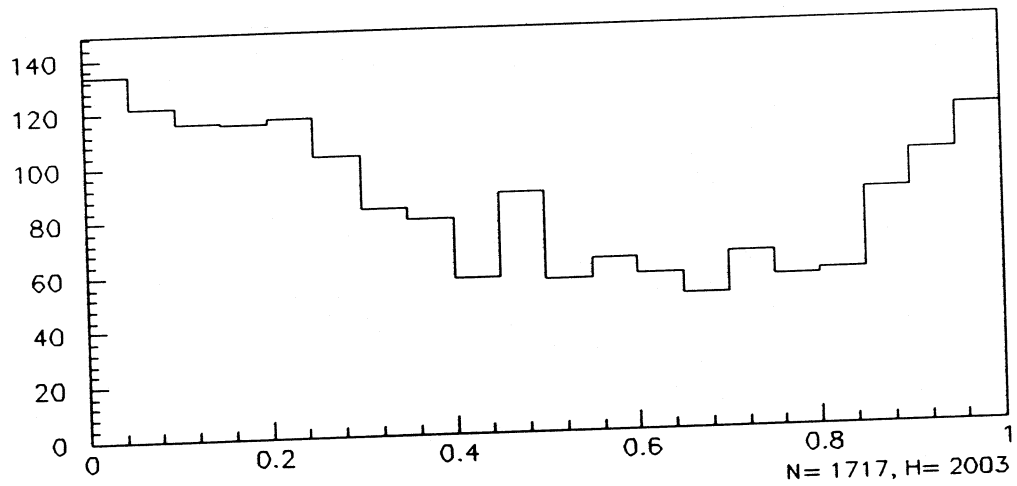
$10° \times 1°$ **window;** $\quad$ **p** $\geq 25 GeV/c;$ $\quad$ **Parabolic Fit;** $\quad$ **Phase**

Figure 7.2.3: The phase plot for the $10° \times 1°$ elliptical window centered on Cygnus X-3, with a 25 GeV/c cut on momentum, using both the cubic and parabolic fits.

N= 452, H= 2004

$10° \times 1°$ **window;** $\mathbf{p} \geq 100GeV/c$; **Cubic Fit;** **Phase**

N= 452, H= 2004
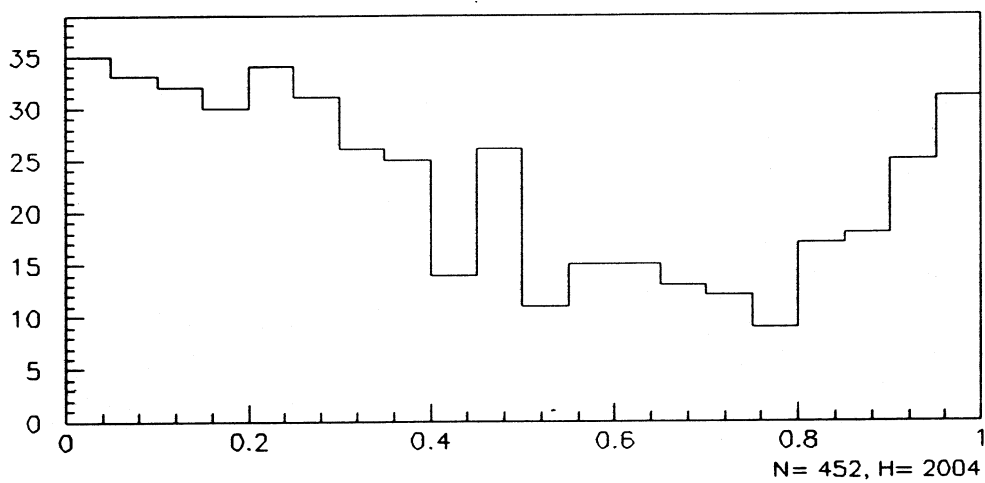
$10° \times 1°$ **window;** $\mathbf{p} \geq 100GeV/c$; **Parabolic Fit;** **Phase**

Figure 7.2.4: The phase plot for the $10° \times 1°$ elliptical window centered on Cygnus X-3, with a 100 GeV/c cut on momentum, using both the cubic and parabolic fits.

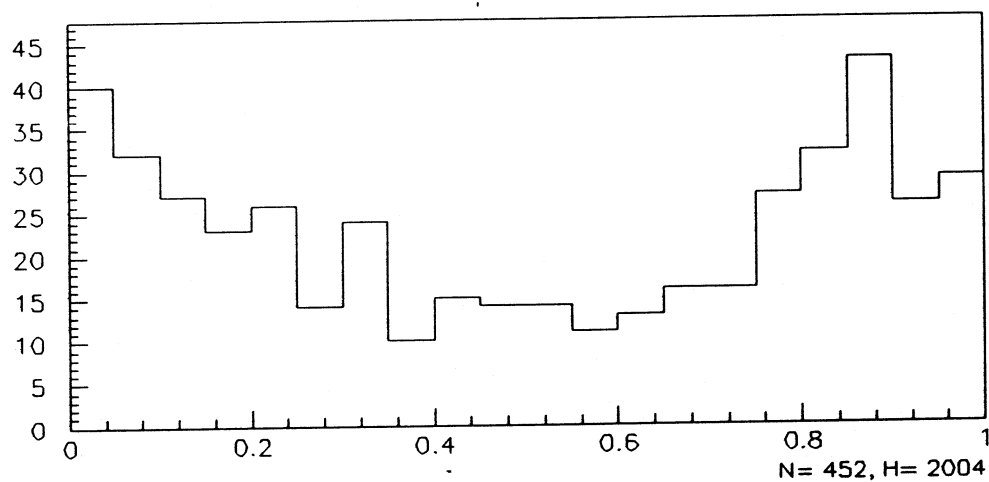minimum of 10 ± 3.16 events at a phase range of $0.35 - 0.40$, and a maximum of 43 ± 6.6 at a phase range of $0.85 - 0.90$. The maximum in this plot seems to be slightly more prominent compared to its neighboring phases than the other two plots, though it is hard to tell due to the broadly sloping shape of the plot.

All four sets of plots in Figures 7.2.1 - 7.2.4 show similar results for the parabolic fit. The shape of the phase distributions are the same as the cubic distributions, only they are shifted about 0.15 or so in phase. All of the parabolic fit histograms show a minimum at around $0.65 - 0.65$ and a maximum around $0.00 - 0.05$. The standard $10° \times 1°$ elliptical window has a minimum of 283 ± 16.8 events at a phase range of $0.60 - 0.65$, and a maximum of 586 ± 24.2 events at a phase range of $0.05 - 0.10$. The window with the 10 GeV/c cut on momentum looks similar, and has a minimum of 133 ± 11.5 events at a phase range of $0.60 - 0.65$, and a maximum of 296 ± 17.2 at a phase range of $0.05 - 0.10$. The window with the 25 GeV/c cut on momentum has a minimum of 49 ± 7.0 events at a phase range of $0.65 - 0.70$, and a maximum of 134 ± 11.6 at a phase range of $0.00 - 0.05$. And the window with the 100 GeV/c cut on momentum has a minimum of 9 ± 3.0 events at a phase range of $0.75 - 0.80$, and a maximum of 35 ± 5.9 at a phase range of $0.00 - 0.05$. The windows with the momentum cuts do not seem to show a more prominent peak, though it is hard to tell due to the broadly sloping shape of the plots.

The offset in the shape between the cubic fit histograms and the parabolic fit histograms can be explained as follows. The period of the Cygnus X-3 system is almost exactly 4.8 hours, but varies slightly with time. The cubic and parabolic

fits show how fast the period changes. This difference is very small. Both fits are referenced to some arbitrary zero time, as explained in Section 3.3.2, that is far enough back in time that no negative times can occur in calculations. So the difference between the zero reference time, and the time at which the data taking occured, is very large so small differences in the rate of change of the period could make a large difference in the phase histograms. On the other hand, the the time over which data was collected was on the order of 3 months, which corresponds to about 480 orbital periods of the Cygnus X-3 system. Since this is a much smaller time frame, the differences between the calculated phases will be much smaller. So we would expect the phase histograms to have similar shapes due to the small data collection time, and have these shapes offset due to the large difference between the reference time and the data collection time.

The cubic fit gives us a maximum in the phase plot of $0.85 - 0.90$, which is in the phase range where we would expect to see a peak; however, the phases vary too much. Other experiments showed the phase histogram looks fairly flat with a narrow peak somewhere in the $0.65 - 0.90$ phase range if there is a measurable muon signal coming from Cygnus X-3,and no peak if there is no signal coming from Cygnus X-3. The data we have collected contains smoothly sloping distributions, with the maximums having over double the number of events as the minimums. This suggests that we may be seeing a second type of time bias in the data. Data runs were started everyday at approximately the same time, and often ended two or three hours later. Coincidentally, the period of the Cygnus X-3 system is on the order of $\frac{1}{5}$ of a day or 4.8 hours. So

each data run was usually not on long enough to capture the entire 4.8 hour cycle, and when the run was started the next day at the same time, it would start in a similar part of the orbital period as it was when it was started the day before. Thus, it is easy to see how certain parts of the phase distribution could accumulate many more events than others in a smoothly sloping manner. The only way to avoid this time bias is to have the data runs in even multiple of 4.8 hours. This would assure each part of the phase distribution had equal exposure to the detector.

One way that this time bias can be verified is by looking at the phase distribution for the background windows, and verify that they look the same. Recall, Eq. 3.13 was used in conjunction with the phase equation (Eq. 3.12) to insure that any zenith angle effects affecting the source region will affect the background regions in the phase, so if this time bias does exist it should also be seen in the background windows. Figures 7.2.5 - 7.2.8 show the phase distributions for the seven $0° - 60°$ right ascension from Cygnus X-3 windows in 3-dimensional surface plots, and correspond to Figures 7.2.1 - 7.2.4 respectively.

Figures 7.2.5 - 7.2.8, though not completely smooth, show that the the time bias is present in all of the background windows, as well as the source window. Though there are some local maximums and minimums in the plots, it is fairly easy to see that the cubic fit plots show a minimum in phase around $0.40 - 0.50$, and a maximum in phase around $0.90 - 0.95$. Likewise the parabolic fit plots show a minimum in phase around $0.45 - 0.65$, and a maximum in phase around $0.00 - 0.05$ (hard to see in the 3-dimensional plot). It also looks like in both the

Figure 7.2.5: A comparison of both the cubic (top) and parabolic (bottom) fit phase distributions from $0° - 60°$ right ascension from Cygnus X-3 for the $10° \times 1°$ elliptical windows.

Events

300

200

60

Right Ascension

0.25   0.5   0.75   1

Phase

$10° \times 1°$ **window;** $p \geq 10 GeV/c$; **Cubic Fit**

Events

300

200

60

Right Ascension

0.25   0.5   0.75   1

Phase

$10° \times 1°$; $p \geq 10 GeV/c$; **Parabolic Fit**

Figure 7.2.6: A comparison of both the cubic (top) and parabolic (bottom) fit phase distributions from $0° - 60°$ right ascension from Cygnus X-3 for the $10° \times 1°$ elliptical windows with a 10 GeV/c restriction on momentum.

10° × 1° **window;** p ≥ 25GeV/c; **Cubic Fit**

10° × 1° **window;** p ≥ 25GeV/c; **Parabolic Fit**

Figure 7.2.7: A comparison of both the cubic (top) and parabolic (bottom) fit phase distributions from 0° − 60° right ascension from Cygnus X-3 for the 10° × 1° elliptical windows with a 25 GeV/c restriction on momentum.

Events

40
30
20
10

60

Right Ascension

0.25   0.5   0.75   1

Phase

$10° \times 1°$ **window;** $\mathbf{p} \geq 100 GeV/c$;   **Cubic Fit**

Events

40
30
20
10

60

Right Ascension

0.25   0.5   0.75   1

Phase

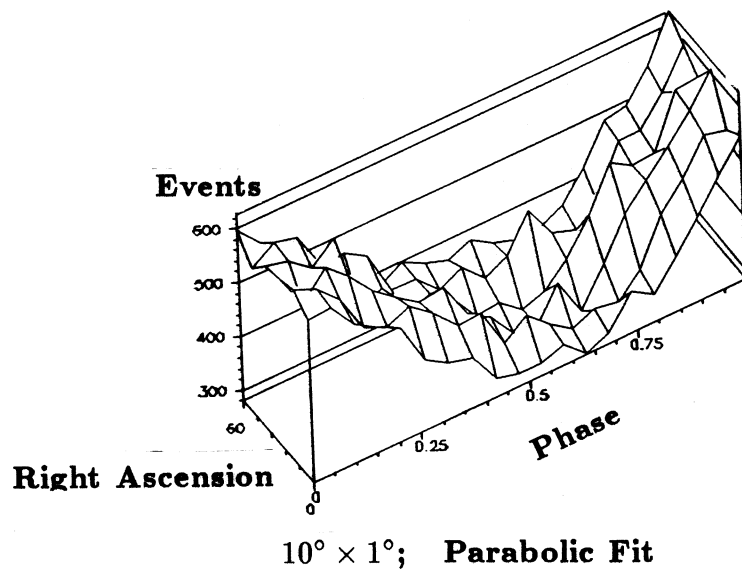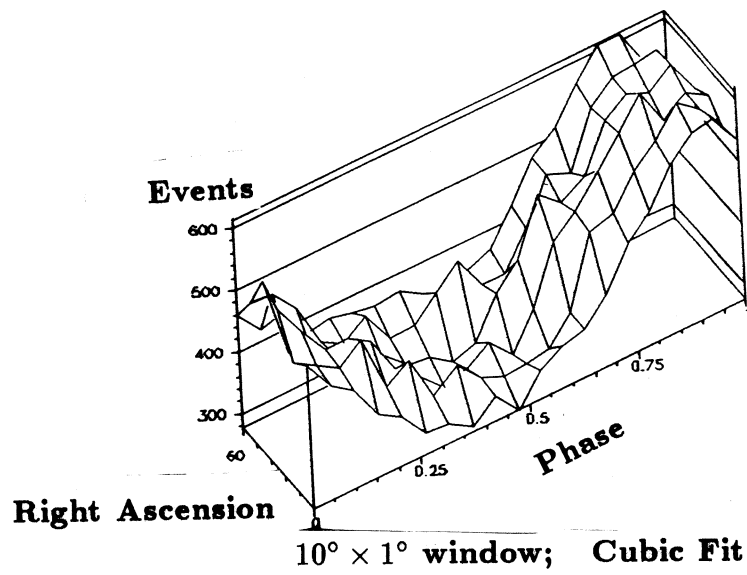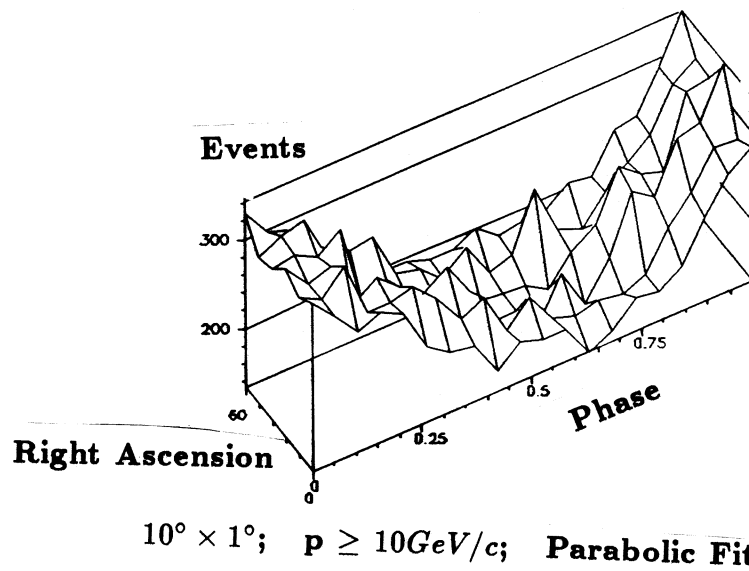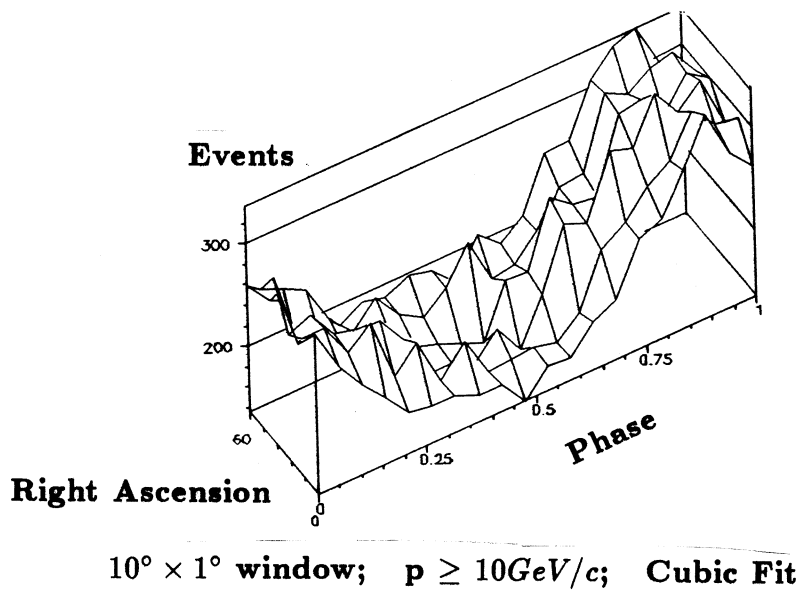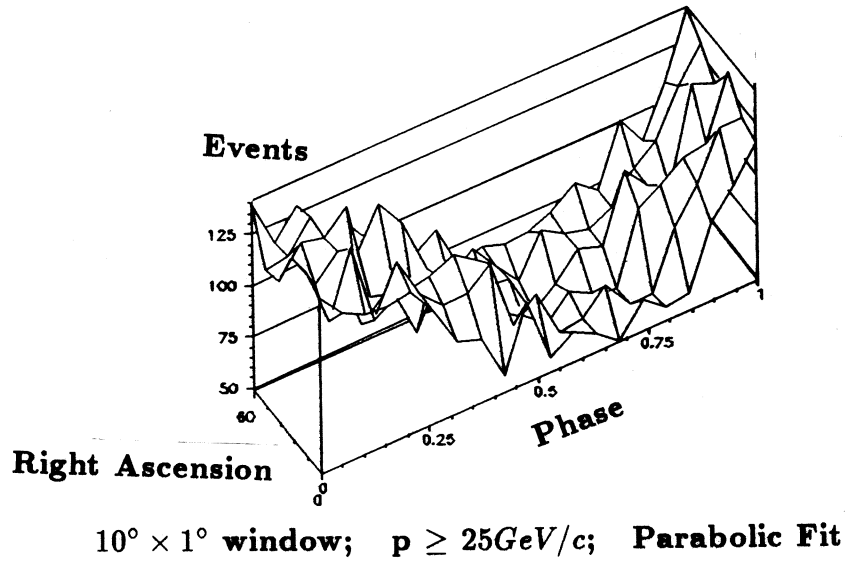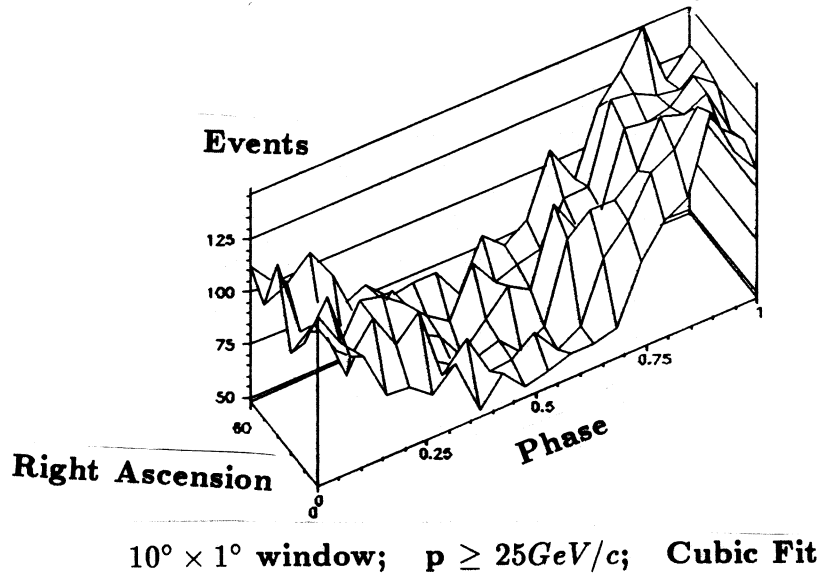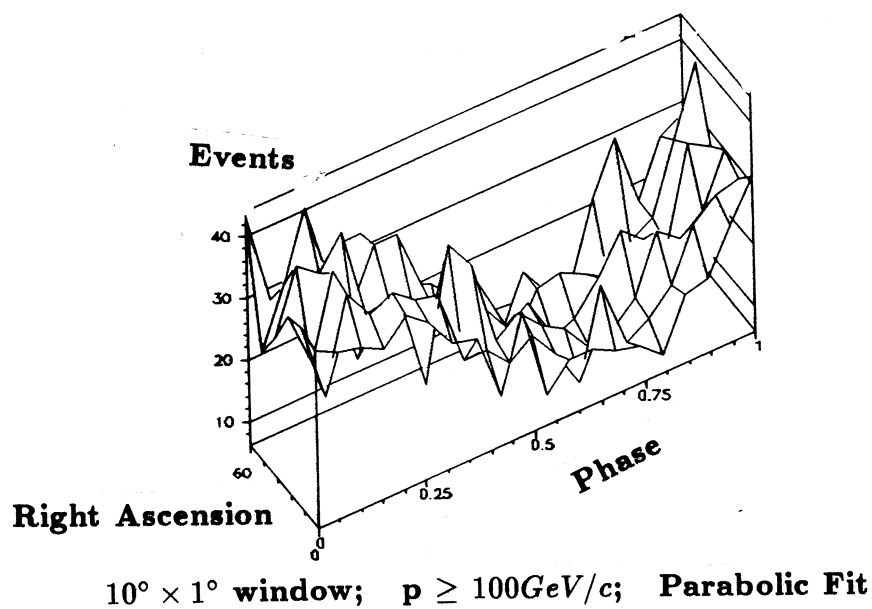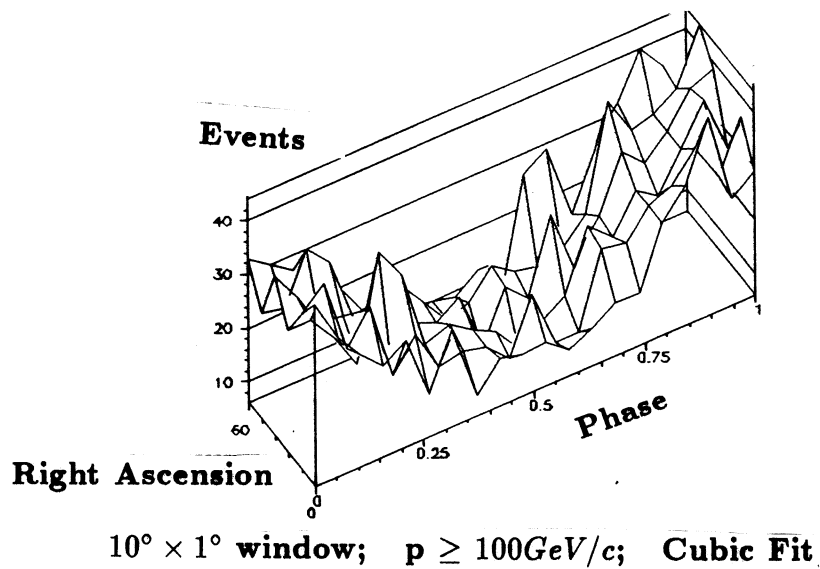$10° \times 1°$ **window;** $\mathbf{p} \geq 100 GeV/c$;   **Parabolic Fit**

Figure 7.2.8: A comparison of both the cubic (top) and parabolic (bottom) fit phase distributions from $0° - 60°$ right ascension from Cygnus X-3 for the $10° \times 1°$ elliptical windows with a 100 GeV/c restriction on momentum.

parabolic and cubic fits that the curvature of the background windows is very similar to the source window in all cases. Similar plots were also made using all 36 windows, using the cubic and parabolic fits, and showed the same phase areas as mentioned above contained the maximums and minimums. This shows without a doubt that the time bias exists in the phase histograms centered on Cygnus X-3, and in all of the background windows as well.

Since there is an obvious time bias in the phase histograms in Figures 7.2.1 - 7.2.4, we can not use the shape of source histograms alone to determine if there is a time modulated signal coming from the direction of Cygnus X-3. To correct for the time bias seen in the phase histograms, the background windows can be used to determine an expected background count in each of the phase intervals. The normal course of action is to add up the total number of events in each of the phase bins for all of the background windows and divide them by the number of background windows to get an expected background count for each phase interval. Then the phase histogram for the source window can be compared to the phase histogram created from the expected background counts. The problem with this method is it assumes equal exposure times for all of the windows. Earlier it was determined that the number of events coming from the window centered on Cygnus X-3 was far less than the average number of events in the background windows. So, if we simply add all of the events in each phase bin for all six background windows and divide them by six, we have more events in almost all of the phase bins for the background window compared to the source window. Weighting the windows by exposure time would be one way

to cure this problem; however, this would be very hard if not impossible to do with our time biased sample.

Another solution to the problem is really only valid if no signal is coming from Cygnus X-3, and that is to weight the background windows based on the number of events in them. For example, the standard $10° \times 1°$ source window has $8,226$ events, compared to $52,501$ events in the six background windows. That is a ratio of 6.38:1 (instead of the ideal 6:1) background events to source events. Similarly, the sets of windows with the 10 GeV/c, 25 GeV/c, and 100 GeV/c momentum cuts have 6.45:1, 6.42:1, and 5.94:1 background events to source events ratios respectively. If there is no signal coming from Cygnus X-3, and the number of events in each phase bin for the sum of all six background windows is divided by 6.38 (for the standard $10° \times 1°$ window), and then the numbers left in each phase bin are subtracted from the phase bins in the source windows, event counts close to zero events should be left in each phase bin. If there is a signal coming from Cygnus X-3 and it contains a narrow peak $0.05 - 0.15$ in phase as seen in other experiments, then the same method of subtracting a weighted background from the source window for each phase interval should eliminate the time bias mentioned earlier and still show the feature of the narrow phase peak. The only difference is that since we are weighting by number of events instead of exposure time, the events in the phase peak will appear to be less significant. This is because any events in the source window actually coming from Cygnus X-3 are included in the count for the source window, lowering the actual background window events to source window events ratio. Thus

the actual background count would be underestimated, and a plot histogram showing the phase bins of the weighted background subtracted from the source window phase bins would have its zero point (the point where the number of source counts equals the number of weighted background counts) raised higher than it would be in the distribution if it was weighted proporly.

Figures 7.2.9 - 7.2.12 show the number of events in each phase bin left from subtracting a weighted background from the source window, and Tables 7.2.1 - 7.2.4 list the numbers left in each phase bin along with their uncertainties and σ values. The time bias has been eliminated from the data, and we have more random looking distributions. All of the cubic plots show an inconsistent broad peak from about $0.85 - 0.15$ in phase, and the parabolic plots show an inconsistent broad peak from about $0.00 - 0.25$ in phase. This broad peak is seen best in the standard elliptical window, and is seen less in the windows with restrictions on momentum. Both of these are about the same width as was seen by the Soudan-1 experiment, only shifted slightly. For the cubic fit, which is considered the better of the two fits, the peak is shifted 0.20 in phase and for the parabolic fit the peak is shifted 0.35 in phase.

For the cubic fit, broad phase peak seems to be most prominent in the standard $10° \times 1°$ window. The σ values in the phase peak are 1.96, 2.52, 1.84, 1.64, 1.40, and 1.35. For the window with a 10 GeV/c cut on momentum the σ values in the peak are 2.68, 0.05, -0.16, 2.51, 1.22, and 0.32. For the window with a 25 GeV/c cut on momentum the σ values are 2.41, 0.55, -0.22, 2.53, 1.14, and 1.51. And for the window
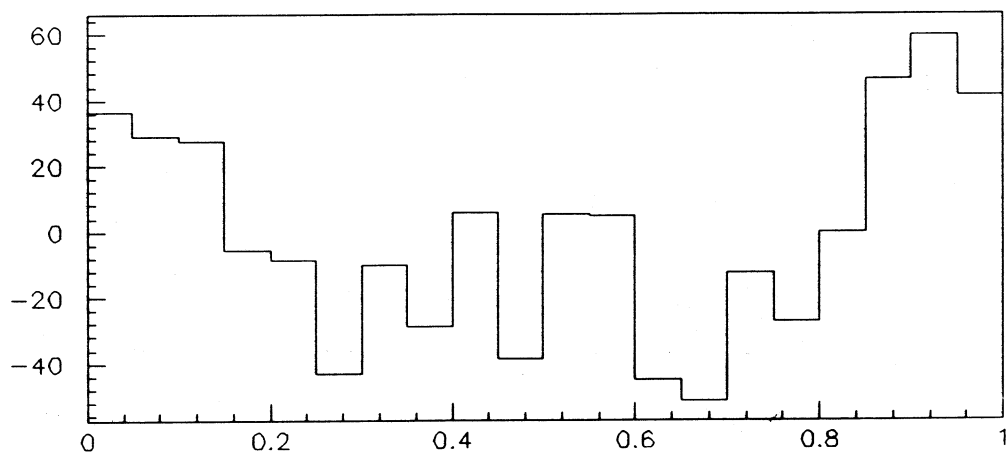
10° × 1° window;   Cubic Fit;   Events - Background
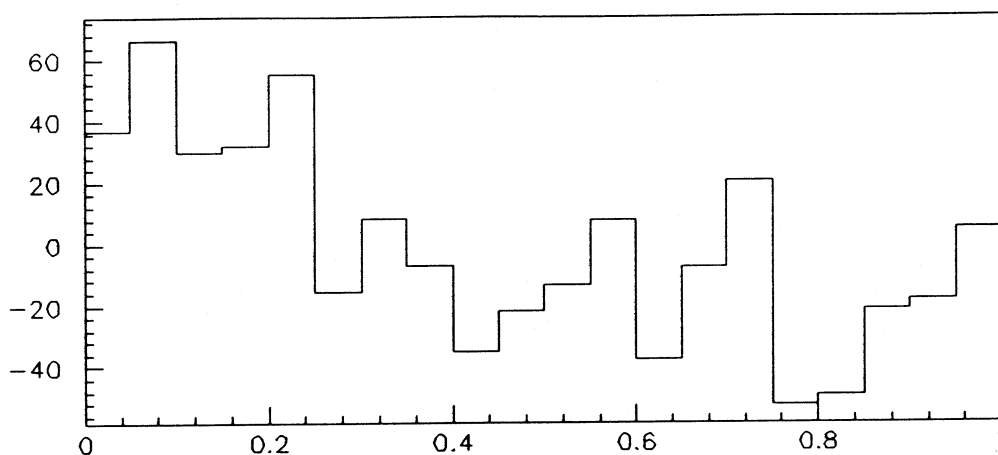
10° × 1°;   Parabolic Fit: Events - Background

Figure 7.2.9: A comparison of both the cubic (top) and parabolic (bottom) fit for the 10° × 1° windows showing the expected background in each phase bin subtracted from the source phase bins in Figure 7.2.1.

Table 7.2.1: A comparison of the phase results for the $10° \times 1°$ elliptical window centered on Cygnus X-3 using both the cubic and parabolic fits.

Phase	Events − Background			
	Cubic Fit	σ	Parabolic Fit	σ
0.00 − 0.05	37.1 ± 31.9	1.64	38.1 ± 34.3	1.57
0.05 − 0.10	29.9 ± 30.2	1.40	67.4 ± 33.9	2.84
0.10 − 0.15	28.1 ± 29.4	1.35	31.1 ± 32.9	1.33
0.15 − 0.20	− 4.9 ± 27.9	−0.24	33.0 ± 32.0	1.46
0.20 − 0.25	− 8.0 ± 27.1	−0.40	55.9 ± 30.8	2.60
0.25 − 0.30	− 42.3 ± 26.1	−2.19	− 14.5 ± 29.3	−0.68
0.30 − 0.35	− 9.4 ± 25.3	−0.51	8.9 ± 27.9	0.45
0.35 − 0.40	− 28.2 ± 24.8	−1.55	− 6.6 ± 27.8	−0.33
0.40 − 0.45	6.3 ± 25.4	0.34	− 33.9 ± 26.1	−1.77
0.45 − 0.50	− 38.0 ± 24.6	−2.09	− 21.1 ± 25.4	−1.14
0.50 − 0.55	6.0 ± 25.6	0.33	− 12.8 ± 25.3	−0.70
0.55 − 0.60	5.3 ± 26.5	0.28	8.6 ± 25.3	0.48
0.60 − 0.65	− 44.3 ± 27.8	−2.16	− 37.0 ± 24.9	−2.01
0.65 − 0.70	− 50.9 ± 29.4	−2.34	− 6.9 ± 24.9	−0.38
0.70 − 0.75	11.8 ± 30.9	−0.52	21.0 ± 26.7	1.11
0.75 − 0.80	− 26.4 ± 32.4	−1.11	− 51.7 ± 27.2	−2.56
0.80 − 0.85	1.0 ± 33.8	0.04	− 48.3 ± 29.0	−2.26
0.85 − 0.90	47.4 ± 34.1	1.96	− 20.2 ± 30.4	−0.92
0.90 − 0.95	60.4 ± 34.0	2.52	− 17.3 ± 32.3	−0.74
0.95 − 1.00	42.3 ± 32.6	1.84	6.1 ± 33.6	0.25

$10° \times 1°$ **window;** $p \geq 10 GeV/c$; **Cubic Fit;** **Events - Background**
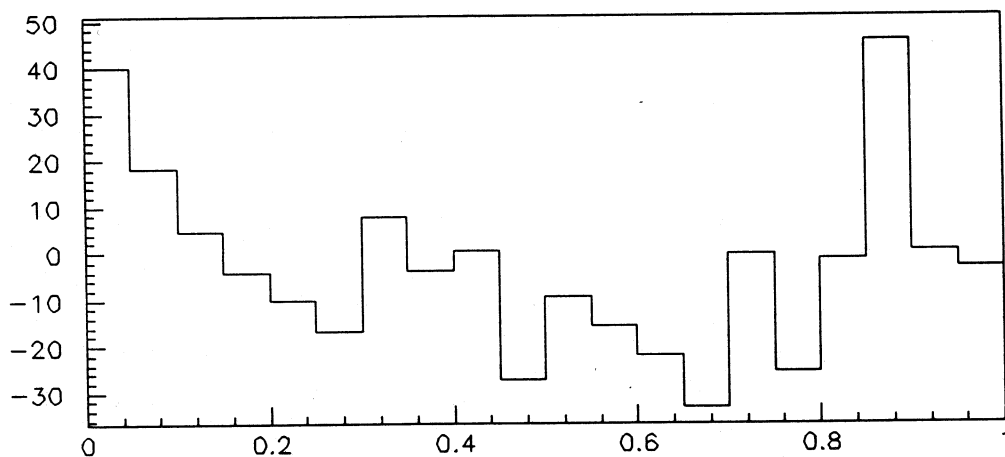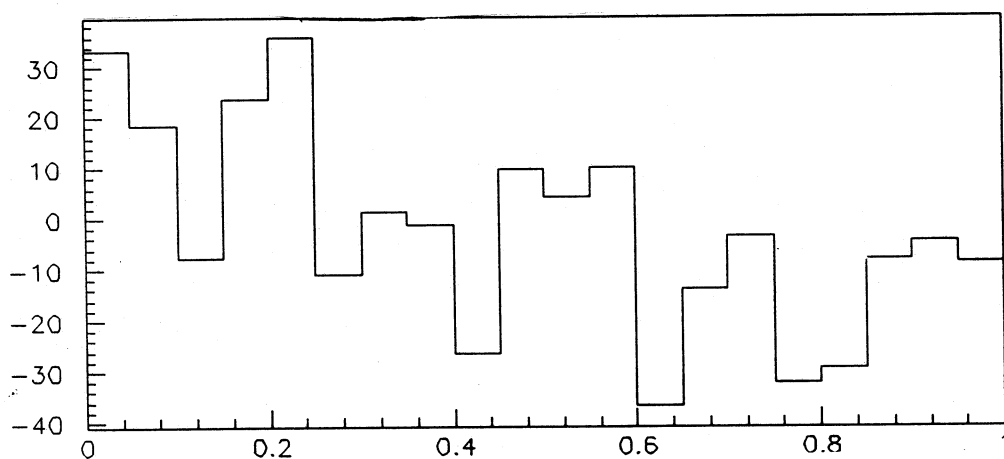

$10° \times 1°$; $p \geq 10 GeV/c$; **Parabolic Fit;** **Events - Background**

Figure 7.2.10: A comparison of both the cubic (top) and parabolic (bottom) fit for the $10° \times 1°$ windows with a 10 GeV/c cut on momentum showing the expected background in each phase bin subtracted from the source phase bins in Figure 7.2.2.

Table 7.2.2: A comparison of the phase results for the $10° \times 1°$ elliptical window with a 10 GeV/c momentum cut centered on Cygnus X-3 using both the cubic and parabolic fits.

	Events − Background			
Phase	Cubic Fit	σ	Parabolic Fit	σ
0.00 − 0.05	40.7 ± 23.5	2.51	33.1 ± 25.0	1.90
0.05 − 0.10	18.9 ± 22.1	1.22	18.5 ± 24.2	1.09
0.10 − 0.15	4.9 ± 21.2	0.32	-7.6 ± 23.6	−0.44
0.15 − 0.20	-3.6 ± 20.2	−0.25	23.7 ± 23.3	1.46
0.20 − 0.25	-9.7 ± 19.1	−0.71	35.8 ± 22.5	2.31
0.25 − 0.30	-16.6 ± 19.1	−1.19	-11.1 ± 21.3	−0.71
0.30 − 0.35	8.0 ± 18.4	0.62	1.3 ± 20.1	0.09
0.35 − 0.40	-3.5 ± 18.2	−0.27	-1.3 ± 20.0	−0.09
0.40 − 0.45	0.7 ± 18.0	0.06	-26.5 ± 18.5	−1.94
0.45 − 0.50	-26.9 ± 17.4	−2.08	9.6 ± 18.7	0.73
0.50 − 0.55	-9.2 ± 18.2	−0.70	4.3 ± 18.4	0.33
0.55 − 0.60	-15.4 ± 18.3	−1.15	10.1 ± 18.2	0.79
0.60 − 0.65	-21.6 ± 19.8	−1.49	-36.7 ± 17.5	−2.78
0.65 − 0.70	-32.7 ± 20.6	−2.14	-13.9 ± 17.5	−1.10
0.70 − 0.75	0.2 ± 22.2	0.01	-3.6 ± 18.7	−0.27
0.75 − 0.80	-25.0 ± 23.4	−1.47	-32.2 ± 19.3	−2.24
0.80 − 0.85	-0.7 ± 24.3	−0.04	-29.3 ± 20.1	−1.97
0.85 − 0.90	46.4 ± 25.1	2.68	-7.9 ± 21.7	−0.50
0.90 − 0.95	0.9 ± 24.1	0.05	-4.5 ± 23.4	−0.27
0.95 − 1.00	-2.6 ± 23.2	−0.16	-8.6 ± 24.3	−0.49
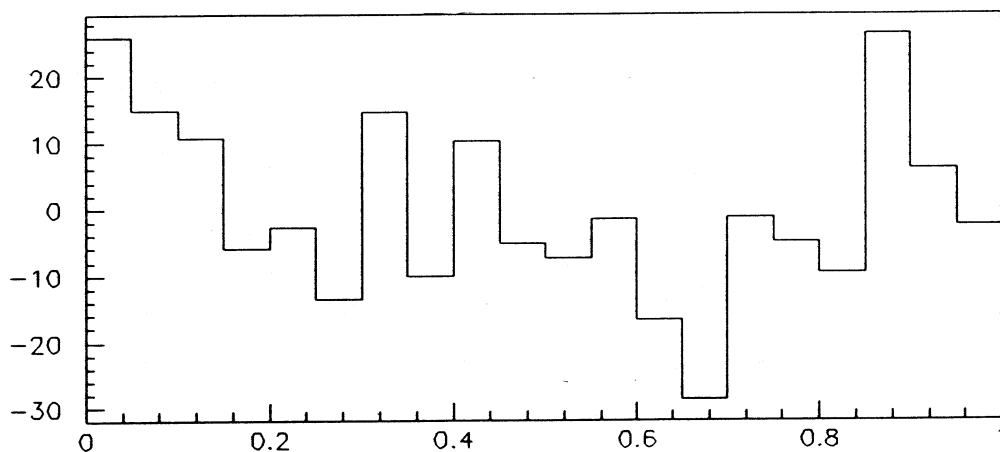
$10° \times 1°$ **window;** $\mathbf{p} \geq 25 GeV/c;$ **Cubic Fit;** **Events - Background**

$10° \times 1°$ **window;** $\mathbf{p} \geq 25 GeV/c;$ **Parabolic Fit;** **Events - Background**

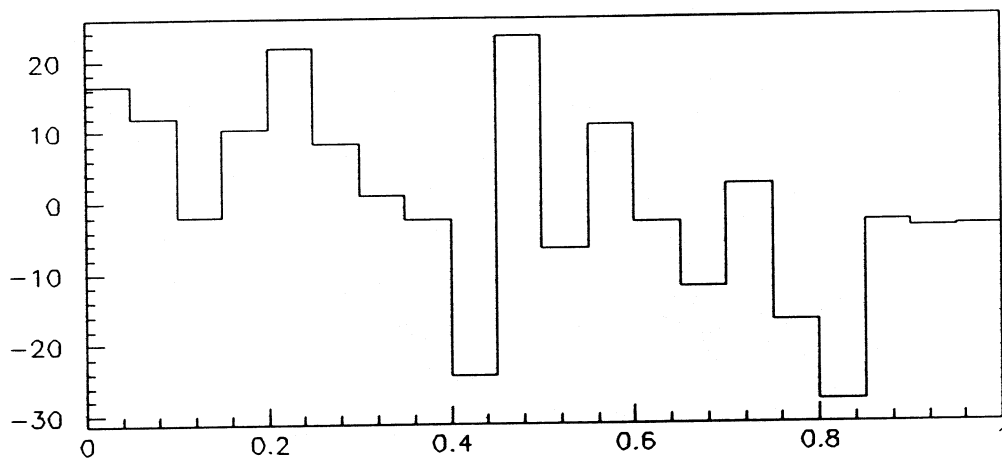**Figure 7.2.11:** A comparison of both the cubic (top) and parabolic (bottom) fit for the $10° \times 1°$ windows with a 25 GeV/c cut on momentum showing the expected background in each phase bin subtracted from the source phase bins in Figure 7.2.3.

Table 7.2.3: A comparison of the phase results for the $10° \times 1°$ elliptical window with the 25 GeV/c cut on momentum centered on Cygnus X-3 using both the cubic and parabolic fits.

Phase	Events − Background			
	Cubic Fit	σ	Parabolic Fit	σ
$0.00 - 0.05$	25.9 ± 15.3	2.53	16.5 ± 15.9	1.13
$0.05 - 0.10$	15.0 ± 14.4	1.51	11.9 ± 15.3	1.13
$0.10 - 0.15$	10.8 ± 13.8	1.14	-2.2 ± 15.4	-0.20
$0.15 - 0.20$	-6.0 ± 12.7	-0.65	10.4 ± 14.9	1.00
$0.20 - 0.25$	-2.6 ± 12.5	-0.29	21.9 ± 14.6	2.23
$0.25 - 0.30$	-13.6 ± 12.3	-1.49	8.2 ± 14.1	0.84
$0.30 - 0.35$	14.8 ± 11.9	1.85	1.0 ± 12.9	0.11
$0.35 - 0.40$	-10.0 ± 10.6	-1.28	-2.6 ± 12.7	-0.28
$0.40 - 0.45$	10.3 ± 10.9	1.40	-24.4 ± 11.8	-2.69
$0.45 - 0.50$	-5.2 ± 10.6	-0.68	23.4 ± 12.4	2.90
$0.50 - 0.55$	-7.4 ± 10.9	-0.93	-6.6 ± 10.9	-0.83
$0.55 - 0.60$	1.47 ± 11.0	-0.18	10.7 ± 10.8	1.47
$0.60 - 0.65$	-16.7 ± 11.6	-1.90	-2.9 ± 10.8	-0.38
$0.65 - 0.70$	-28.6 ± 12.4	-2.98	-12.0 ± 10.5	1.53
$0.70 - 0.75$	-1.2 ± 13.4	-0.13	2.4 ± 11.2	0.30
$0.75 - 0.80$	-4.9 ± 14.6	-0.47	-16.9 ± 11.3	-1.98
$0.80 - 0.85$	-9.5 ± 15.2	-0.86	-28.2 ± 12.0	-3.03
$0.85 - 0.90$	26.5 ± 16.3	2.41	-3.0 ± 13.3	-0.32
$0.90 - 0.95$	6.0 ± 15.5	0.55	-4.0 ± 14.3	-0.39
$0.95 - 1.00$	-2.4 ± 14.8	-0.22	-3.6 ± 15.4	-0.32
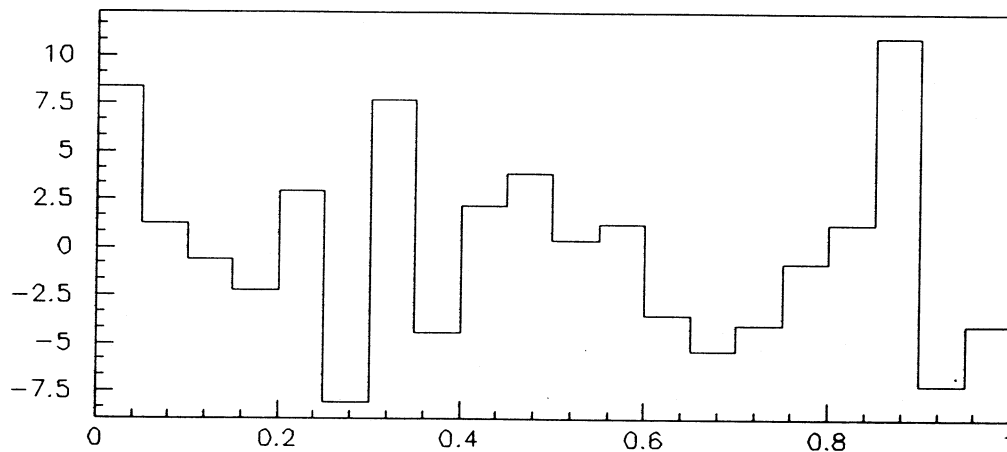
$10° \times 1°$ **window;** $\mathbf{p} \geq 100 GeV/c$; **Cubic Fit;** **Events - Background**

$10° \times 1°$ **window;** $\mathbf{p} \geq 100 GeV/c$; **Parabolic Fit;** **Events - Background**

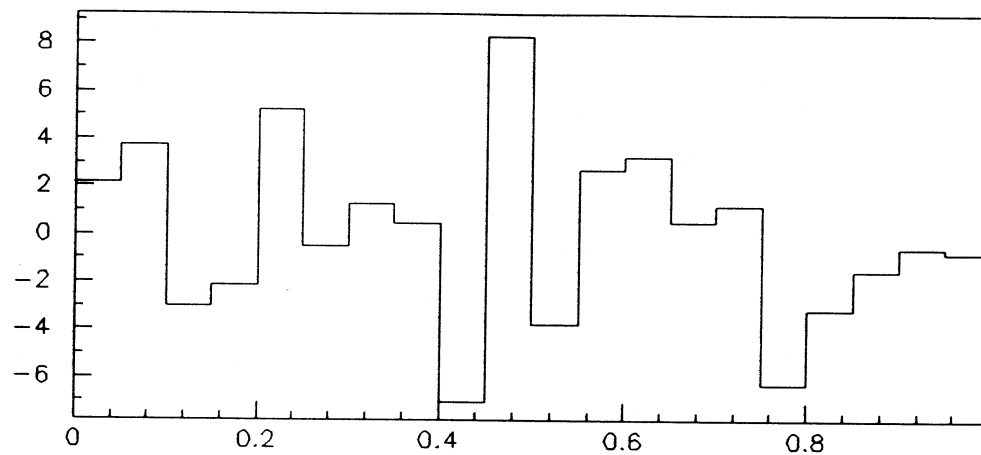**Figure 7.2.12:** A comparison of both the cubic (top) and parabolic (bottom) fit for the $10° \times 1°$ windows with a 100 GeV/c cut on momentum showing the expected background in each phase bin subtracted from the source phase bins in Figure 7.2.4.

Table 7.2.4: A comparison of the phase results for the $10° \times 1°$ elliptical window with the 100 GeV/c cut on momentum centered on Cygnus X-3 using both the cubic and parabolic fits.

Phase	Events — Background			
	Cubic Fit	σ	Parabolic Fit	σ
$0.00 - 0.05$	8.4 ± 8.5	1.48	2.2 ± 8.2	0.68
$0.05 - 0.10$	1.2 ± 7.9	0.21	3.7 ± 7.9	0.68
$0.10 - 0.15$	-0.6 ± 7.4	-0.11	-3.0 ± 8.2	-0.51
$0.15 - 0.20$	-2.2 ± 7.0	-0.45	-2.1 ± 7.9	-0.38
$0.20 - 0.25$	2.9 ± 7.0	0.61	5.2 ± 7.9	0.97
$0.25 - 0.30$	-8.0 ± 6.0	-1.71	-0.5 ± 7.9	-0.08
$0.30 - 0.35$	7.7 ± 6.4	1.89	1.3 ± 7.1	0.25
$0.35 - 0.40$	-4.5 ± 4.9	-1.17	0.4 ± 7.0	0.09
$0.40 - 0.45$	2.2 ± 5.3	0.62	-7.0 ± 5.9	-1.53
$0.45 - 0.50$	3.9 ± 4.9	1.23	8.3 ± 6.6	1.98
$0.50 - 0.55$	0.4 ± 5.3	0.10	-3.8 ± 5.1	-0.99
$0.55 - 0.60$	1.2 ± 4.6	0.40	2.7 ± 5.2	0.77
$0.60 - 0.65$	-3.5 ± 5.4	-0.86	3.2 ± 5.2	0.94
$0.65 - 0.70$	-5.4 ± 6.1	-1.16	0.5 ± 5.0	0.15
$0.70 - 0.75$	-4.0 ± 6.0	-0.90	1.2 ± 4.8	0.37
$0.75 - 0.80$	-0.8 ± 7.4	-0.15	-6.3 ± 4.9	-1.61
$0.80 - 0.85$	1.2 ± 7.9	0.22	-3.2 ± 6.1	-0.71
$0.85 - 0.90$	11.0 ± 8.7	1.95	-1.5 ± 6.1	-0.34
$0.90 - 0.95$	-7.2 ± 7.7	-1.24	-0.6 ± 7.1	-0.11
$0.95 - 1.00$	-4.0 ± 7.9	-0.69	-0.8 ± 7.9	-0.14

with a 100 GeV/c cut on momentum the σ values are 2.41, 0.55, — 0.22, 2.53, 1.14, and 1.51. The parabolic fit shows similar results with the standard $10° \times 1°$ window showing the most prominent broad peak with σ values of 1.57, 2.84, 1.33, 1.46, and 2.60. Likewise the σ values for the broad peak in the window with the 10 GeV/c momentum cut are 1.90, 1.09, −0.44, 1.46, and 2.31; the σ values for the peak in the window with 25 GeV/c momentum cut are 1.50, 1.13, −0.20, 1.00, and 2.23; and the σ values for the broad peak in the window with the 100 GeV/c momentum cut are 0.38, 0.68, −0.51, −0.38, and 0.97. The standard $10° \times 1°$ elliptical window shows the most impressive σ for the parabolic fit windows in the phase range of $0.10 − 0.15$. These peaks look only marginal, but could actually be the result of a time modulated signal from Cygnus X-3.

It is interesting to note that the significance of the broad peaks mentioned above appear to get less significant as the momentum cut is increased. This is just the opposite of what would be expected if there was a signal of high energy parent particles coming from Cygnus X-3. Many of the experiments that looked for a muon signal from Cygnus X-3 were far underground and only the higher energy muons reach their detectors. It is also interesting that in both the cubic and parabolic fits, there seem to be two narrow peaks within the broad peak that seems more prominent than the rest. This occurs at the phase ranges of $0.85 − 0.90$ and $0.0 − 0.05$ for the cubic fit and at the phase ranges of $0.05 − 0.10$ and $0.20 − 0.25$ for the parabolic fit. These peaks also get less significant as the momentum cut is increased, but are always present.

In both the parabolic and cubic fits there appears to be a flat area that looks like it could be the average background rate. This shows up best on the standard $10° \times 1°$ windows. This flat area is from about $0.15 - 0.60$ in phase in the cubic fit histogram and from about $0.25 - 0.75$ in phase in the parabolic fit histogram. This flat region is all slightly below zero as would be expected from earlier arguments if there is a signal coming from Cygnus X-3.

The biggest problem with all of the expected background subtracted histograms is that they all also have a significant dip that is almost as statistically significant as the peak. This valley appears to be narrower than the apparent peak. For the cubic fit, the lowest part of the dip occurs at $0.65 - 0.70$ and has σ values of -2.34, -2.14, -2.98, and -1.16 in the four sets of windows. For the parabolic fit, the lowest part of the dip occurs at the phase interval $0.80 - 0.85$ and has σ values of -2.26, -1.97, -3.03, and -0.71. These valleys could mean two things. First it could mean that all of the time bias was not taken care of in earlier steps. At this point that would make the data set completely useless for the purpose of trying to see a periodic signal coming from Cygnus X-3. The other possibility is that if the peak is a signal from Cygnus X-3, then the actual zero point on the histograms should be moved down and the valleys are then not as statistically significant as they appear. It is interesting to note that the Soudan-1 experiment had a significant dip in their plot (see Fig. 4.1). Their dip occured in the $0.20 - 0.25$ phase range, but this does not correspond to the dip in our plots.

It is also interesting to note that the Soudan-1 data was published for data collected from September 1981 to December 1983, and our data was collected from September 1989 to December 1989. From the time that Soudan-1 published to the time that our data was taken, the Cygnus X-3 system completed 10,950 orbits. Conceivably, the small errors in the orbital calculations could have added up over the six years between the experiments and caused the shift in phase. The cubic fit is considered the better of the two fits, and would thus track the orbital period of Cygnus X-3 better over the span of a large number of years. If our peaks are actually equivalent to the Soudan-1 peaks, then one would expect the parabolic fit to have its data shifted further than the cubic fit data. That is exactly what we see. However, there is no published proof that the cubic or parabolic fit would shift as much as it would have to for our peak to correspond with the one seen by Soudan-1. Preliminary results from Soudan-2, which has taken more recent data, shows no shift in the phase peak in signals from Cygnus X-3. On the other hand, the 1988 van der Klis and Bonet-Bidaud article stated that the parabolic and cubic fits start to diverge around the year 1985.[16]. This would at least verify that there should have been a shift in the phase distributions between the cubic and parabolic fits. Another major problem with our results is that we have used a very shaky, and at points unorthodox, analysis that was necessary due to the two major time biases that existed in the data.

Chapter 8
Conclusions

An attempt to point muon tracks back to Cygnus X-3 was made using the D0muon cosmic ray telescope. A raw data set of 83 PRD files with 11.3 million events were examined, representing 313.5 hours of live time from September 13 to December 13, 1989. The PRD data was filtered with a set of predetermined set of cuts which resulted in a data set of 83 DST files containing a total of 3,478,283 events. Three windows were opened that were centered on Cygnus X-3. A standard $10° \times 1°$ elliptical window centered on Cygnus X-3 contained 8,226 events. Three windows centered on Cygnus X-3 with momentum cuts of 10 GeV/c, 25 GeV/c, and 100 GeV/c were also opened, and contained 4,289, 1,171, and 452 events respectively. For each window centered on Cygnus X-3, there were 35 other windows that were centered on the same declination, and spaced every $10°$ right ascension. These windows were used to determine background rates to attempt to search for a DC excess of events coming from Cygnus X-3. A severe time bias was found in the data, since the data runs were not even multiples of the sidereal day. It was discovered that the six windows from $10° - 60°$ formed the best estimate of the background, since they were closest in the number of events to the window centered on Cygnus X-3. However, the source window still contained far fewer events than the average of these six windows, due to the time bias. This made searching for a DC excess of events from the direction of Cygnus X-3 impossible.

An attempt was made to search for a periodic signal coming from the windows centered on Cygnus X-3. To do this phase histograms were created from Eq. 3.12 for each of the source windows. The phase ranged from 0.00 − 1.00, and was folded to the 4.79 hour Cygnus X-3 orbital period, with a phase of 0.00 being defined as the minimum of the x-ray modulation. The phase was calculated using both the cubic and parabolic fit cited in the 1988 van der Klis and Bonnet-Bidaud ephemeris. This ephemeris was used by all of the experiments trying to point muon tracks back to Cygnus X-3. Soudan-1 and NUSEX saw significant signals in the phase ranges 0.65 − 0.90 and 0.70 − 0.80 respectively. Our phase histograms turned out to contain a second time bias since the data runs were not in even multiples of the 4.79 hour periodicity. After an estimated background for each phase bin was subtracted from each bin in the source window, the remaining phase plot did not show evidence of the 4.79 hour time bias, since the phase of background windows was corrected for any zenith angle effects or right ascension biases with Eq. 3.13 so that all of the windows would place event biases in the same phase band.

The background subtracted phase distributions showed a inconsistent broad peak about 0.25 − 0.30 wide in phase. This is the same width as the peak seen by Soudan-1 in 1983. The peak that Soudan saw was in the phase range 0.65 − 0.90, and the peaks in our plots using the cubic and parabolic fit were in the phase ranges 0.85 − 0.15 and 0.00 − 0.25 respectively. It is questionable whether or not the peaks in our plots are real, or an artifact of our unorthodox analysis made necessary by the time biases present in the data. The peaks

actually became less significant as the momentum cuts become more strict. Even if the peak observed is actually evidence of time modulation, there is still the problem that the peaks do not occur in the same region of phase as the Soudan-1 peak, so the phases would have had to have shifted in the six years between the two experiments. This is possible, but if true the 1988 van der Klis and Bonnet-Bidaud ephemeris would again have to be updated so that the phase distributions would not drift in the period from 1981 − 1990. The parabolic fit is known to have shifted since 1985, which could explain why the peak in our parabolic distribution is shifted, both in respect to the Soudan-1 data and to our cubic fit data. However, there is no evidence that the cubic fit has shifted in that time, which questions the validity of our peak. Also, the fact that we saw two prominent peaks inside of the broad peak for both the cubic and parabolic fit was not observed by any other experiment. As with the braod peak, the narrow peaks became less significant as the momentum cut increased. This observation, along with the fact that these peaks are only of marginal significance anyway, leads one to believe that we are not seeing a time modulated signal in our phase plots.

The solution to the problem of whether there is a signal coming from Cygnus X-3 would be to collect a completely unbiased data sample. This would allow us to see if there are any muon signals coming from Cygnus X-3. If the data is collected in equal multiples of the sidereal day (23.933 hours), the first time bias that we saw would disappear. This would allow us to see if there is a DC excess of events coming from Cygnus X-3. All of the windows studied

would have the same exposure to the detector, so the background calculations outlined in Section 3.3.1 would be completely valid. Also if the data is collected in equal multiples of the Cygnus X-3 orbital period (4.79 hours) then the second time bias would also be eliminated. This would allow us to create phase histograms which are more realistic, and allow us to properly calculate the expected background rate for each phase bin. So a completely unbiased data set would have to be taken in in 114.64 (4.79 × 23.9333) hour or 4 days 18.6 hour chunks. Time in between these runs could be used for taking pedestal and pulser runs and upkeep of the detector. Recall, that Taker's limitations would require that we restart a new data run every 18 hours, with about 10 minutes of downtime between runs. So taking data runs constantly in 114.64 hour segments would mean that we would have to start 7 consecutive runs with Taker, which would result in only 70 minutes in downtime in the entire sample. This $\approx 1\%$ down time would certainly be easier to handle than the severely biased sample that we presently have. At the average $10Hz$ data collection rate, each 114.64 hour segment of data would contain over four million events. So in less than one month, more data could be collected than has ever been looked at.

Unfortunately, the cosmic ray telescope is now disassembled and is thus not available for another data run. However, there may be another answer to helping us determine if there is a muon signal coming from Cygnus X-3. Since the D0muon cosmic ray telescope is so similar to the D0 experiment at Fermilab, it would be useful in the future for the someone to continue where

I am leaving off with this experiment using the D0 detector during one of its cosmic ray commissioning runs. Using the analysis that I have outlined in this experiment and the program that I use to look for the DC excess and phase correlation, and applying these to the D0 detector, could lead to some valuable information. A few weeks of continuous data collection at D0 could accumulate a sample large enough to be useful. That would be a great contribution to both the physics and astrophysics communities, since it would once and for all answer the controversial question of whether a time modulated muon signal can be detected coming from the direction of Cygnus X-3.

References

1. J. M. Bonnet-Bidaud and G. Chardin, Physics Reports (Review section of Physics Letters), "Cygnus X-3, A Critical Review," **170**, 326-404 (1988).

2. W. Thomas Vestrand and David Eichler, Astrophy. J., "On Ultrahigh-Energy Gamma Rays from Cygnus X-3," **261**, 251-258 (1982).

3. Mark Thomson, "Muon Astronomy at Soudan II", Pembroke College, Oxford, 1989 (unpublished).

4. G. Chanmugan and K. Brecher, Nature, "Ultra-high energy γ rays and cosmic rays from accreting degenerate stars," **313**, 767-768 (1985).

5. J. E. Pringle, Nature, "Model for Cygnus X-3," **247**, 21-22 (1974).

6. N. E. White and S. S. Holt, Astrophy. J., "Accretion Disk Coronae," **257**, 318-337 (1982).

7. M. Milgrom and D. Pines, Astrophy. J., "Cygnus X-3: A Cocooned X-Ray Binary Pulsar?" **220**, 272-278 (1978).

8. Demosthenes Kazanas and Donald C. Ellison, Nature, "Origin of Ultra-High-Energy γ-rays From Cygnus X-3 and Related Sources," **319**, 380-382 (1986).

9. Bertram Schwarzschild, Phys. Today, "Are the Ultra-Energetic Cosmic Gammas Really Photons?" **41**, 17-21 (1988).

10. M. L. Marshak, *et al.*, Phys. Rev. Lett., "Evidence for Muon Production by Particles from Cygnus X-3," **54** (19), 2079-2082 (1985).

11. J. Kochocki, , "Astronomy Primer", Tufts International Memo PDK-380, 1988 (unpublished).

12. K. Johns, "A First Look at Astrophysics with D0muon Test," Talk, D0 meeting at Fermi National Accelerator Laboratory, 1989 (unpublished).

13. D. E. Nagle, T. K. Gaisser, and R. J. Protheroe, "Extensive Air Showers Associated with Discrete Astrophysical Sources," Ann. Rev. Nucl. Part. Sci., **38**, 609-657 (1988).

14. Ti-pei Li and Yu-quian Ma, Astrophy. J., "Analysis Methods for Results in Gamma-Ray Astronomy," **272**, 317-324 (1983).

15. M. van der Klis and J. M. Bonnet-Bidaud, Astron. Astrophys., "A Change in the Light Curve Asymmetry and the Ephemeris of Cygnus X-3," **95**, L5-L7 (1981).

16. M. van der Klis and J. M. Bonnet-Bidaud, Astron. Astrophys., "The X-ray Ephemeris of Cygnus X-3," **214**, 203-208 (1989).

17. M. L. Marshak, *et al.*, Phys. Rev. Lett., "Time Distributions for Underground Muons from the Direction of Cygnus X-3," **55** (19), 1965-1968 (1985).

18. M. F. Cawley, *et al.*, Astrophy. J., "Variability In the Light Curve of Very High Energy Gamma Rays From Cygnus X-3," **296**, 185-189 (1985).

19. B. D'Ettorre Piazzoli, "Cygnus X-3 Muon Signal In The NUSEX Experiment," Talk given at the workshop on high-energy to ultra-high-energy behavior of Accreting X-ray sources, Vulcano (Italy), LNF-87/1P, 1986 (unpublished).

20. G. Battistoni, *et al.*, Phys. Lett., "Observation of A Time Modulated Muon Flux In the Direction of Cygnus X-3," **155B** (5,6), 465-467 (1985).

21. R. M. Bionta, *et al.*, Phys. Rev. D, "Underground search for muons correlated with Cygnus X-3," **36** (1), 30-36 (1987).

22. D. J. Cutler and D. E. Groom, "Mayflower Mine Search for Cygnus X-3," in Proceedings of the XXIII International Conference on High Energy Physics, 1986 (Berkeley).

23. Ch. Berger, *et al.*, Phys. Lett. B, "Search For Muons From the Direction of Cygnus X-3," **174** (1), 118-122 (1986).

24. Y. Oyama, *et al.*, Phys. Rev. Lett., "Search for high-Energy Muons from Cygnus X-3," **56** (9), 991-994 (1986).

25. M. Fortner, "A Cosmic Ray Muon Telescope at Fermilab," 1-6, Fermilab, March 9, 1989 (unpublished).

26. R. Mueller, "A Measurement of the Cosmic Ray Muon Charge Ratio Distribution at Sea Level Over the Momentum Range of 5 − 250GeV/c", M. S. Thesis, Northern Illinois University, December 1991 (unpublished).

27. N. Oshima and S. Igarashi, "Response of the D0 Muon Chamber to Changes in Voltage, Incident Angle, Gas Composition, and Gas

Contamination," D0 Note 805, Fermilab, February 24, 1989 (unpublished).

28. C. Brown, *et al.*, Nucl. Instrum. & Methods, "D0 Muon System with Proportional Drift Tube Chambers," **A279**, 331-338 (1989).

29. D. Green, H. Haggerty, S. Hansen, and M. Takasaki, Nucl. Instrum. & Methods, "Accurate 2 Dimensional Drift Tube Readout Using Time Division and Vernier Pads," **A256**, 305-312 (1987).

30. M. Fortner and D. Hedin, "Muon Trigger Update," D0 Note 890, Fermilab, September 15, 1989 (unpublished).

31. B. Drendel, "D0 Muon Chamber Monitor Board Calibration Procedure," D0 Note 974, Fermilab, June 6, 1990 (unpublished).

32. R. I. Morphis, "Motherboard Documentation," D0 Note 983, Fermilab, 1990 (unpublished).

33. M. Fortner, "Level 1 Muon Trigger Logic," D0 Note 816, Fermilab, 1989 (unpublished).

34. L. Scarpelli, "Control Board Testing," D0 Note 979, Fermilab, June 28, 1990 (unpublished).

35. M. Fortner, *et al.*, IEEE Trans. Nucl. Sce. (USA), "The VME-Based D0 Muon Trigger Electronics," **38**, 480-485 (1991).

36. K. Bazizi, "Dzero Muon Electronics - Module Address Card," D0 Note 897, Fermilab, November 6, 1989 (unpublished).

37. T. Sze, "Muon Coarse Centroid Trigger Card Documentation," D0 Note 995, Fermilab, 1990 (unpublished).

38. D. Green, "Muon Trigger Electronics Upgrade," D0 Note 557, Fermilab, May 12, 1987 (unpublished).

39. M. Fortner (private communication).

40. D. Cutts, *et al.*, Computer Physics Communication, "Data Acquisition at D0," **57**, 339-342 (1989).

41. Spectracom Corporation, Model 8170 WWVB Synchronized Clock Owners Manual, April, 1988..

42. D0 Software Group, computer code CALIB (Fermi National Accelerator Laboratory, Batavia, Il., 1990).

43. D0 Software Group, computer code EXAMINE (Fermi National Accelerator Laboratory, Batavia, Il., 1990).

44. D0 Software Group, computer code FILTER (Fermi National Accelerator Laboratory, Batavia, Il., 1990).

45. D0 Software Group, computer code HBOOK4 (Fermi National Accelerator Laboratory, Batavia, Il., 1990).

46. D0 Software Group, computer code DISPLAY5 (Fermi National Accelerator Laboratory, Batavia, Il., 1990).